Titel der Arbeit:

Probing levitated droplets with mass spectrometry

zur Erlangung des akademischen Grades
doctor rerum naturalium
(Dr. rer. nat.)
im Fach Chemie
eingereicht an der
Mathematisch-Naturwissenschaftlichen Fakultät
der Humboldt-Universität zu Berlin

von

Dipl. Chem. Arne Stindt

Präsident der Humboldt-Universität zu Berlin
Prof. Dr. Jan-Hendrik Olbertz

Dekan der Mathematisch-Naturwissenschaftlichen Fakultät
Prof. Dr. Elmar Kulke

Gutachter/innen: 1. Prof. Dr. Ulrich Panne

2. Prof. Dr. Klaus Rademann

Tag der mündlichen Prüfung: 13.04.2016

Abstract

Ultrasonic levitation combines advantages of microfluidics like the required small sample volumes with a wall-less sample handling. While the coupling of analytical methods like optical spectroscopy as well as x-ray scattering are very well elaborated, an established mass spectrometric method to obtain molecular analytical information is still lacking.

The herein presented work describes the fundamental processes for a contactless mass spectrometric analysis of levitated droplets. First, the influences of the specially designed levitator geometry on the levitation capabilities is described. During further experiments, the use of infrared lasers has proven useful as a combined desorption and ionization source for organic molecules from a mixture of water and glycerol as chromophore. Subsequently, sonic-spray ionization was used to gain a deeper understanding of the ionization processes occurring within the spray plume. Mass spectrometric mapping as well as laser-induced fluorescence were performed to investigate the ionization during an aerodynamic breakup of the micro droplets in the spray process.

As a complementary sampling method, the ionization with a low-temperature plasma source is described. First, a time-resolved mass spectrometric investigation of the ionization process is shown. Subsequent to this fundamental study, the application of such a plasma source for the direct analysis of volatile compounds from within the droplets in the surrounding environment without interferences from the droplets bulk phase is described.

Zusammenfassung

Ultraschalllevitation kombiniert die Vorteile von Mikrofluidik, wie beispielsweise die sehr geringe benötigte Probenmenge, mit einer wandlosen Probenhandhabung. Obwohl die Kopplung zwischen levitierten Tröpchen und verschiedenster analytischer Methoden wie optischer Spektroskopie und Röntgenbeugung sehr genau untersucht ist, fehlt es immer noch an einer etablierten Kopplung mit einer massenspektrometrischen Methode für die Analyse auf molekularer Ebene.

Die vorliegende Arbeit beschreibt die Prinzipien, auf denen eine kontaktlose massenspektrometrische Analyse von levitierten flüssigen Proben beruht. Zuerst wurde der neu entworfene akustische Levitator bezüglich des Einflusses seiner Geometrie auf die Levitationseigenschaften experimentell und mittels numerischer Simultationen untersucht. Die anschließend durch geführten Experimente demonstrieren das Potential von Infrarot-Lasern als kombinierte Desorptions- und Ionisationsquelle für organische Substanzen aus einer Mischung aus Wasser und Glycerin als Cromophor. Um einen tieferen Einblick in die hierbei ablaufenden Ionisationsmechanismen zu erhalten, wurde als Modell ein "Sonic-Spray" Konus räumlich per Massenspektrometrie und Laser-induzierter Fluoreszenz untersucht.

Levitator-Geometrie auf die Levitationseigenschaften stimmen sehr gut mit numerischen Simulationen überein. Als komplementäre Ionisationsmethode wurde eine Niedertemperatur-Plasmaquelle eingesetzt. Nach einer zeitaufgelösten Untersuchung der grundlegenden Ionisationsmechanismen wurde diese Quelle für die Untersuchung flüchtiger Spezies aus der levitierten Probe in deren direkten Umgebung ohne störende Interferenzen genutzt.

Contents

Chapter 1

Levitated droplets in analytical chemistry

This chapter provides an overview of the scientific achievements on which the presented work is based.

From biology to geochemistry water plays an important role. It not only covers roughly 70 percent of the earth's surface but also small aerosol water droplets within a size range of $0.1 - 100$ µm form an immense water-air interface in our atmosphere.[1] Both, this boundary layer and the droplets have a drastic influence on earth's climate, which is due to its complexity still poorly understood.[2] The physical properties of those aerosols strongly depend on the highly diverse mixture of various inorganic and organic analytes occurring inside the droplets and on their surfaces.[3] Starting at this macroscopic scale, a further zoom in reveals the importance of water on a microscopic scale. It accounts for two thirds of a human's body mass, representing the pristine environment for biomolecules like proteins. Compared to the airborne aerosols the amount of water in a human cell is even smaller. A standard human cell with a diameter of 20 µm contains of only a few femtoliters of water.

To get a deeper insight into fundamental processes taking place in those small volumes, sophisticated analytical techniques are required. The scientific field handling fluid amounts in the range of nanoliters to attoliters is called microfluidics.[4] One of the most remarkable features of this area is the high scientific diversity ranging from physics over engineering and chemistry towards life sciences and ending in daily life's applications.

Microfluidics

Billions of years before humankind created the sciences of microfluidics nature had already optimized this field. Trees are a very good example of this highly developed and specialized system of small fluid channels with diameters from micrometers to small as a few nanometers.[5] The already mentioned and much newer scientific field of microfluidics can be divided into subfields characterized by

the methods used to handle the liquids. In capillary-based microfluidics the liquids flow through microchannels often incorporated into small chips. The width of these microchannels is usually in the order of tens of micrometers, which promotes unique liquid behaviors like laminar flow.[4] The ambition in those systems is to maintain the sensitivity and high resolution of standard analytical methods and simultaneously miniaturize the used device and therefore the required sample amounts and costs. The now common term *lab-on-a-chip* (LOC) was introduced to describe the efforts to miniaturize a whole laboratory on a small device for chemical[6], biological[7] or medical[8;9] purposes. The development of such devices is motivated by the need for the ability to carry out 'in-field' analyses. Those needs arise from the long time spans and/or the financial efforts involved in a standard analysis in an off-site analytical laboratory. For example it would be possible to perform comprehensive parallel environmental monitoring by installing a dense mesh of small and cheap LOC systems. Furthermore, the application of an on-line control of a patient's response to a medical therapy as a so called point-of-care[10] testing is very promising. LOC systems could also act as portable medical 'labs' for the use in isolated regions[11;12] in developing countries or other places lacking medical care like cargo ships or battlefields.[13] Despite those existing 'killer applications' and other high-throughput applications, the big breakthrough of LOC has not yet occurred. While the miniaturization of the fluid system is well elaborated, the shrinking of the detection systems accompanied by a decrease of costs still remains a challenge.

In addition to the efforts to establish LOC as an on-site device for non-professionals, there is a great interest in exploiting the advantages of microfluidics in traditional sciences. They offer a big potential for parallelization of analytical processes combined with much lower sample consumption, for example in bioassay screen-

ings and other high-throughput applications.[14] Additionally, it is possible to manipulate single particles, cell aggregates or even single cells in LOC devices with optical or acoustical tweezers,[15] which offers deep insights into the behavior of single cells and their diversity.

Regardless of the benefits that microfluidics offer, there are some drawbacks in the use of LOC devices. As already mentioned, the miniaturization of sophisticated detection methods represents a major issue, especially regarding the fact that the design towards small sample amounts claims high demands on the limits of detection for those systems. Another flaw is the chemical incompatibility of the commonly used chip material polydimethylsiloxane[16] with many organic solvents, thus limiting the range of applications to aqueous systems. On the other hand, chemically more inert materials like glass are much more difficult and expensive to process. Also the optical characteristics of the material have to be regarded with respect to optical detection methods. Teflon for example lacks the optical transparency for the used detection methods. Besides those macroscopic disadvantages, some major obstacles can be found on the molecular level. Minimization in volume leads to maximization in surface-to- volume ratio. In other words, the smaller the volume gets, the more likely the chemistry is governed by physical or chemical processes occurring on the surface. Depending on the texture of the microchannel's surface, undesirable molecule interactions can occur. This could result in adhesion of biomolecules on the surfaces and their subsequent removal from further analysis. Another surface-induced side effect is crystal nuclei formation resulting in a bad comparability of those results obtained in LOC analysis and those from standard analytical techniques.

Many of the herein described disadvantages can be circumvented by the use of contactless sample handling methods.[17] Common

contactless methods like magnetic or electrostatic levitation exploit special sample characteristics which are needed to hold the samples in place. Different approaches which are less demanding on the sample conditions are aerodynamic and optical levitation, both of which are not suitable to handle liquids. The most versatile method which avoids all of the disadvantages observed in LOC and which is suitable to handle liquids regardless of their charge and magnetic characteristics is called acoustic levitation.

Acoustic levitation

Throughout the last years, acoustic levitation of droplets, which was once designed for zero gravity experiments, has matured to a versatile technique in analytical chemistry.[18] In reference to the term *lab-on-a-chip* this technique is often called *lab-on-a-drop*.[19] It allows for contactless handling of solutions and thereby prevents analyte-surface interactions. Studies of acoustically levitated samples include X-ray scattering experiments of *e.g.* crystallization processes[20] and protein agglomeration,[21] simultaneous UV/Vis and Raman experiments on nanoparticle formation (see figure 1.1),[22] the interaction of ionic liquids with the atmosphere[23] and kinetics of enzymatic reactions.[24] Successful coupling to mass spectrometry has also been reported.[25] Especially for the coupling with optical methods it is crucial to keep the droplet from moving or deforming during the measurement. This demands for stable ultrasonic traps, *i.e.* traps with a well-defined steep pressure gradient. Despite the parameters of the ultrasonic drivers such as frequency and amplitude, the stability of a trap mostly depends on geometrical parameters used for the transducer and reflector design.

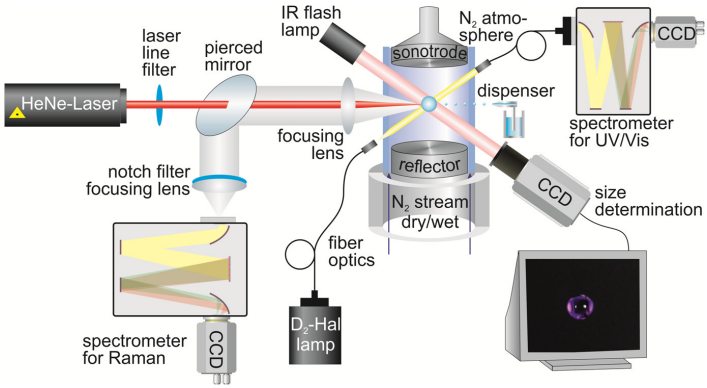

Fig. 1.1: Schematic view of several optical methods coupled parallel to a levitated droplet.[22] It is possible to influence the droplet's environment as well as to add nanodroplets.

In ultrasonic traps, the simplest and most commonly used geometry is the single axis levitator. Here, the transducer and reflector are arranged in a coaxial fashion, sharing the same axis of cylindrical symmetry.[17] The transducer, which often ends in a so-called vibrating plate, moves back and forth towards the reflector in a linear, piston-like motion. At this position the ultrasonic wave is coupled into air and reflected back at the reflector positioned on the opposite side. In the case that the distance between transducer and reflector correspond to a multiple of the ultrasonic wavelength in air a standing wave is formed (fig 1.2). In this wave, an acoustic force which is proportional to the sound pressure compensates gravity and therefore enables levitation. An additional horizontal and also considerably smaller component of this force contributes to stable levitation capabilities in so-called levitation nodes in those pressure maxima along the symmetry axis. In the ideal case, the standing wave has a cylindrical symmetry around its propagation axis (z-axis). While this symmetry gives a good spatial confinement of the levitated object along the z-axis, only a weak confinement in

the xy-plane is provided. The desirable 3D potential well is usually achieved by the above mentioned radiating plate. Excitation in the radial flexural modes within this plate focuses the emitted wave towards the central region of the cavity.[26] This effect is even more pronounced with a curved reflector to refocus the sound wave. In a recent publication, Baer *et al.* could demonstrate the application of such a concave curvature to yield in an even more pronounced pressure well when applied to both, reflector and radiating plate.[27]

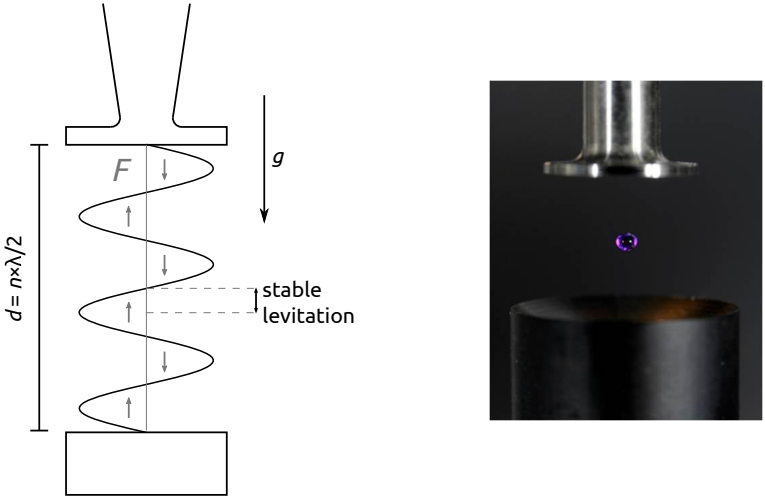

Fig. 1.2: Working principle of an ultrasonic levitator (left). The axial levitation force at a resonance distance which neglects the gravity and the resulting levitation areas are shown. A photo of a droplet containing crystal violet in water trapped in a levitation node (right).

Atmospheric pressure ionization mass spectrometry

In 1912, J.J. Thomson and F.W. Aston performed an experiment where they visualized the deflection of Neon ions in an electrical field[28] and discovered that Neon is composed of the two isotopes ^{20}Ne and ^{22}Ne. This was the first setup in which ions are separated based on their mass-to-charge ratio (m/z) later known as mass spectrometry. In the following one hundred years, this discovery was greatly extended by a lot of groundbreaking and also Nobel Prize rewarded experiments. In principle, every mass spectrometric setup can be divided into three fundamental parts. An ion source is required to form ions out of former neutral molecules or atoms. In contrast to neutral molecules these ions can be manipulated in electric or magnetic fields and therefore be separated based on their m/z ratio in a mass analyzer. In the subsequent last step the ions have to be observed with a detector.

Due to the high demands on collision-free ion flight paths, which can be as long as 17 m,[29] it is essential to provide vacuum conditions in the $\times 10^{-6}$ mbar range. As a result, mass spectrometry from ionization to detection had to be completely performed under those described vacuum conditions for a long time. A big disadvantage of this approach is that the samples have to be transferred into vacuum prior to ionization, which makes a direct access to liquid samples complicated. There were some early notable efforts to perform the ionization step under ambient conditions followed by the transfer of those ions into vacuum in 1966.[30] After all, the progress in turbo molecular pump techniques facilitated broad access to atmospheric pressure ionization mass spectrometry (AP-MS). A wide

field of various ionization techniques evolved with different requirements on sample preparation.

The probably most established technique is called Electro-Spray Ionization (ESI) which was invented by John B. Fenn in 1984, based on the research of Malcom Dole.[31] ESI is likely the AP-MS technique with the highest amount of requirements on the sample preparation and is one of the most important contributions to the evolution of protein characterization to its present state.[32] In ESI, a liquid containing the analyte is nebulized in a taylor cone out of a small capillary with a high voltage applied to the capillary tip.[33] The nebulizing step can be supported by an additional sheath gas. The formed aerosol droplets carry a net charge and are continuously desolvated, which finally leads to the formation of the charged analytes.[34] There are two competitive mechanisms for the transition from a microdroplet to the gas phase. In both mechanisms the localized absolute space charge increases while the droplet desolvates. At some point the charge density becomes to high, which may lead to a so-called coulomb explosion resulting in a completely desolvated molecule[35] or the protonated molecule may diffuse out without a breakup of the droplet.[36] ESI leads to multiply charged ions which results in lower demands on the MS total mass range. However, it suffers from suppression effects which may cause the loss of signals from analytes, depending on their environment and other analytes.[37;38] Two ionization methods which are exclusively suitable for the coupling of liquid chromatography to mass spectrometry are atmospheric pressure chemical ionization (APCI)[39] and atmospheric pressure photoionization (APPI).[40] Both methods require the liquid sample to be vaporized which limits the access to large molecules determined by their thermal stability. APCI utilizes a corona discharge to create protonated water clusters which are able to ionize the analytes in a proton transfer reaction. In

APPI a light source emitting in the vacuum UV region causes a single photon ionization. This method is very selective and generates less background ions.[41]

Sample preparation is not necessary at all with direct desorption/ionization (DDI) methods like direct analysis in real time (DART)[42] dielectric barrier discharges (DBD)[43;44] and flowing-atmospheric afterglow ionization (FAPA).[45] All these methods utilize helium atoms excited in an AC or DC discharge to desorb and ionize samples in a single step. This is either directly caused by Penning ionization or due to a Penning ionization initialized proton transfer reaction. A special position is assigned to matrix-assisted laser desorption ionization (MALDI) initially discovered by Michael Karas and Franz Hillenkamp,[46] which was later transposed to ambient conditions by Laiko *et al.*.[47] In MALDI, the analyte is embedded in an excess of a matrix substance and is then desorped by a ns laser pulse. The matrix is chosen with an absorption maximum that matches the laser wavelength (usually 337 nm or 355 nm). Although both techniques are based on the same sample preparation and experimental methods, the resulting spectra and also the accessibility of analytes differs.[48] It is commonly accepted that those contrasts arise from varying desorption mechanisms under vacuum and atmospheric pressure conditions.[47;49]

While successful coupling of various optical analytical methods to levitated droplets has been reported, only one approach towards a coupling to mass spectrometry has been successfully conducted so far. Herein, corona charging, pulsed high-voltage electrodes, MALDI matrix addition to the droplet and desorption with an UV-laser are combined.[25] In these experiments by Westphall *et al.*, the levitated micro droplets, that already containing formic acid and an UV-chromophore are charged by a corona needle and subsequently exposed to the pulsed output of a nitrogen laser. While the charged

droplet is stabilized by two adjacent ring electrodes, the resulting aerosol plume is directed towards the inlet by a pulsed electric potential applied to two additional electrodes. Despite the pioneering character of this approach, it does not allow any insights into the exact ionization mechanism. Ion formation could result from the reduced pH, the corona charging, the UV-MALDI process, or the applied pulsed electric field. Surprisingly the authors could not observe ion formation when omitting one of the steps, acid addition, corona, UV-laser or pulsed electric field.

Scope of the presented work

While the coupling of optical spectroscopy and x-ray scattering to levitated droplets is very well elaborated, an established mass spectrometric method to obtain molecular analytical information is still lacking. The goal of the here presented work was to advance the research and development towards such a method. In the first step the necessary acoustic levitator was built. The design process and both, a basic characterization of its levitation capabilities and its mechanical durability, are described in CHAPTER 2. A deeper insight into the influence of the levitator geometry on the standing wave will be presented in the second part of CHAPTER 2. The herein obtained results from the sound wave imaging are compared to numerical calculations. The on-line combination of levitated droplets and AP-TOF-MS was investigated utilizing the previously optimized levitator. A laser desorption process allows the transfer of sample from the droplet into the instrument maintaining the advantages of the contactless sample holding technique. The details of the designed setup and the mass spectrometric experiments are described in CHAPTER 3.

A better Understanding of the occurring ion formation process was gained utilizing sonic spray ionization (SSI) as a model for the process of ion formation from neutral droplets. It is shown that the underlying ionization mechanisms in SSI are very similar to those occurring within the droplet desorption process. However, it being a continuous source constitutes a major advantage. Its duty cycle of unity makes it the first choice for deeper investigations. In chapter 4, a novel SSI source is described. This source was characterized by mass spectrometry as well as laser-induced fluorescence (LIF) imaging. A deeper investigation on the spatial differences in the ion formation within the spray plume is presented in the second part of chapter 4.

Whereas the laser desorption yields molecular information of the droplet's bulk phase, complementary information of the droplet's surface and environment was obtained with a dielectric barrier discharge ionization source. The source was first characterized by time-resolved mass spectrometric investigations presented in chapter 5. Later, this source was used to probe the droplets environment which can result in valuable information when investigating chemical reactions with volatile reaction products or to get a better understanding of spray drying processes.

Lastly, in chapter 6 a concluding overview about the overall results is given.

Chapter 2

Design of the ultrasonic levitation device

The design process towards a functioning ultrasonic levitator is described. Furthermore, the correlation between the levitator geometry and the formed the standing wave is analyzed. The resulting sound wave images are compared to numerical calculations.

Ultrasonic levitators

The design of single axis acoustic levitators is typically based on four components: a high frequency power supply, a piezo transducer, a sonotrode (sometimes called horn) and a reflector. An electrical sine function usually in the range of 20 kHz - 60 kHz (with a resulting wavelength range in air of 17 mm - 5.7 mm at 293 K) generated by a power supply is converted into the corresponding mechanical vibration in the piezo transducer. To suppress destructive interferences, the length of the transducer system (*i.e.* the piezo transducer with its metal mounts) has to match the wavelength of the generated vibration. Usually, a system is chosen where the length corresponds to half a wavelength. The vibration created in this way is coupled to a sonotrode. It is worthwhile to choose the same material for the piezo mount and the sonotrode to reach maximum efficiency for the coupling between those parts. The sonotrode serves two purposes: A tapering of the radial cross section increases the amplitude in axial displacement without altering the frequency. Moreover, at the tip of the sonotrode the acoustic wave is coupled into the air and therefore the geometric parameters of this tip clearly have an influence on the wave dispersion characteristics. As for the transducer, its length should also fit a multiple of the speed of sound in the respective medium. At last, a reflector is needed to reflect the ultrasonic wave back and form a standing wave. Again, the geometric parameters and the resulting angle of the back-reflection are crucial for the spatial focusing of the sound wave and therefore for optimal levitation capabilities.

Furthermore, the successful design of ultrasonic traps relies on an accurate and thorough determination of the sound pressure distribution between the transducer and reflector. Different approaches to measure or simulate this pressure pattern have already been ex-

plored. While experimental techniques only allow for critical diagnostics of an existing trap, simulations enable the theoretical optimization of the geometry before the actual trap is constructed. However, simplifications in the underlying models may lead to deviations from these predictions. The ideal approach would therefore be to develop a robust algorithm capable of a fast theoretical prediction of the resulting sound pressure field and a subsequent verification of the accuracy of the prediction by a comparison with experimental data.

Calculations of the sound pressure distribution in acoustic levitators include analytical[50;51] or numerical methods such as the Boundary Element Method[52] and the Finite Element Method.[53] Due to the cylindrical symmetry of most levitators, 2D axisymmetric models are commonly employed, which reduce the computational time considerably compared to 3D models. An interesting approach to calculate the pressure field was proposed by Kozuka and collaborators[54;55] who used the Rayleigh integral with multiply reflected waves between the transducer and the reflector.

In contrast to traditional acoustic levitators which were used to suspend particles in air at a fixed position, new levitation techniques capable of controlling the particle position were proposed recently.[56;57;58;59] These new levitation devices do not have cylindrical symmetry and therefore demand a 3D numerical model to predict the acoustic pressure field. Three-dimensional numerical methods such as the Finite Element Method require long computational times to simulate pressure fields. In order to reduce the computational time, a matrix method based on the Rayleigh integral was proposed[60]. Using this approach, the pressure field of a non-circular levitator can be calculated within a few seconds. This concept is based on the method proposed by Kozuka and collabo-

rators[54;55] as well as the utilization of a monochromatic transfer matrix.[61]

A very simple experimental method for the visualization of the acoustic pressure field is based on concentration of visible matter such as bromine fumes or ice aerosol in the pressure minima.[62] Another very direct approach to measure the levitation potential is directly weighting the compensated gravity on a levitated object with a Cahn balance.[63] These two methods only allow to study the shape of the areas where levitation can occur. A complete image of the sound field can be achieved by optical Schlieren techniques. Unfortunately, the change in the refractive index due to a changed pressure is very subtle[63] and to our knowledge only one successful Schlieren image of an ultrasonic levitator has been published until very recently.[64] Laser interferometry is a novel technique that can also help visualizing the spatial pressure distributions with high speed and resolution and is based on the Schlieren experiments. Two successful approaches have been reported exploiting holographic[65] or Speckle laser interferometry.[58] However, due to the high cost of the instrumentation this technique has so far not been established as a standard tool for the characterization of ultrasonic traps.

A robust and reliable tool to obtain the pressure distribution is to locally measure the acoustic pressure with a small microphone.[63] Lateral scanning of the microphone tip along the meridional plane of the acoustic field allows the recording of a complete two-dimensional map of the sound field.[66] While the scanning makes this procedure time consuming, the method is inexpensive and can be readily automated.

Two modified techniques to obtain sound pressure images will be introduced in this chapter. The experimental technique is a modification of the microphone scanning approach, while the theoretical method is an improved matrix technique. To thoroughly study the

quality of the experimental and theoretical approaches, the results of the individual techniques were compared for four different geometrical designs of ultrasonic traps. These four test sets were generated by the four combinations of two different transducers (with and without radiating plate) and a planar and concave reflector, respectively. This approach not only enables the critical and concise comparison of the proposed methods but also elucidates the effects of the radiating plate and the curvature in the reflector on the sound pressure field.

Designing the parts

For the generation of the high frequency signal, a MWI 400 piezo driver unit modified for a continuous operation mode was connected to an USK 800 Langevine type piezo stack transducer (both MTH Herde, Henstedt Ulzburg, Germany). The generator and transducer were optimized for an output frequency of $f = 40$ kHz. An automated feedback-current-driven tuning in the range of 39 kHz − 41 kHz compensated small deviations in the length of the used sonotrodes and the possible change of speed of sound in the components caused by warming up.

The sonotrode

For the sonotrode design three fundamental parameters have to be considered: the length, the tapering and the form of the tip. The length has to be a multiple of the half wavelength of the sound wave in the used material. The speed of sound c_S with the wavelength λ at a frequency ν is given by

$$c_s = \lambda \nu. \tag{2.1}$$

For solid matters it can also be expressed using material characteristics

$$c_s = \sqrt{\frac{E(1-\mu)}{\rho(1-\mu-2\mu^2)}} \tag{2.2}$$

where E is the elastic modulus of the material, ρ the density and μ the Poisson's ratio. Without considering a transversal propagation inside the material, which is a valid approximation for long rods (length >> diameter), the formula can be simplified to

$$c_s = \frac{E}{\rho}. \tag{2.3}$$

Dural was chosen as material for the sonotrodes, which is a special aluminum alloy (Al95Cu4Mg1) used in the aircraft industry with the characteristics of aluminum but with enhanced durability. With the material constants for the elastic modulus ($E = 73$ GPa) the density ($\rho = 2.77\ \mathrm{g\,cm^{-3}}$) and the Poisson's ratio ($\mu = 0.35$) the resulting speeds of sound are $c_s = 6468$ m/s regarding equation 2.2 and $c_s = 5106$ m/s for the long rod equation 2.3. Considering a frequency of $f = 40$ kHz and the requirement $l = \lambda/2$ the resulting lengths are $l = 80$ mm and $l = 64$ mm, respectively. The sonotrode diameter is determined by the dimensions of the transducer with a diameter of its supporting surface of $d = 17$ mm. The estimated length of the sonotrodes lies in the two digit mm-range and thus lies in between those two assumptions of normal sound propagation and the model for long rods. The most efficient design was evaluated experimentally, observing the deviation from the desired resonance frequency of $f = 40$ kHz. Another important factor for the resulting levitation capabilities is the tapering of the horn along its axis of rotation.[67] This parameter causes an amplification of the axial displacement amplitude conserving the frequency. In figure 2.1 the five usual principal geometries are shown. A simple rod shaped horn without any diminution is shown in figure 2.1 a). This form gives

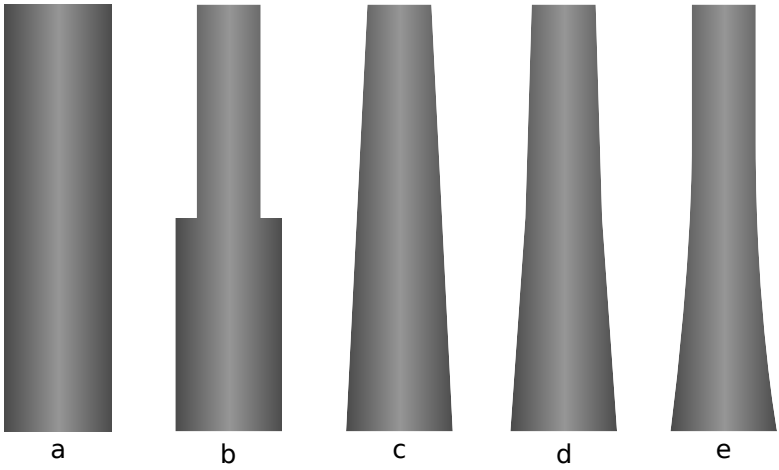

Fig. 2.1: Possible geometries for sonotrodes: a) rod b) stepped c) conical d) double stepped e) exponential.

no amplification but results in the lowest concentration of fluctuating mechanical stress. Also, it's the shape with the lowest demands on the manufacturing process. A simple tapering that is also easy to mill is the 90° step shown in figure 2.1 b). This shape offers a much higher amplification compared to the other four possibilities, but it also shows the highest mechanical stress which could result in material fatigue at the rectangular transition. A conical shape as shown in figure 2.1 c) is a good compromise between the previous two. This design can be elaborated even more resulting in an exponential shape shown in figure 2.1 e). Whereas this is the best solution with an optimal ratio between amplification and stress, it also has the highest requirements on the production process. The exponential tapering can be considered as a superposition of an infinitesimal number of individual steps, hence, a multiply stepped conical design serves as a valid compromise between c) and e).

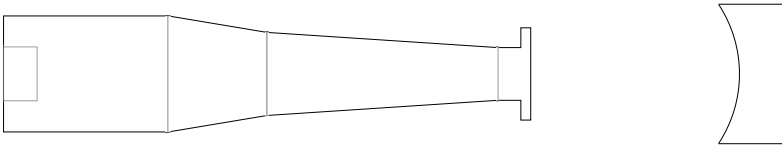

Fig. 2.2: Drawing of the first functional horn and reflector design.

Most sonotrode designs include a so-called radiating-plate at the tips with a diameter usually in the range of the sonotrode before the diminution. However, the effect of this plate on the sound field isn't completely understood and most works only report an improved levitation with such a plate based on empirical findings. For a deeper investigation, prototypes with and without radiating-plates were designed during this work.

The reflector

As known from optical resonators[68], the plane-parallel or Fabry-Pérot geometry is the simplest but not the most performant design for cavities. An improve in geometry is necessary to optimize the resonator's Q-value. Most acoustic levitator designs include a curved reflector whereas this detail is mainly based on assumptions and empirical experiences and not on concrete theoretical models. A first approach to optimize these reflector geometries and therefore the resonators Q-value was made by Xie *et al.*.[69] The optimized parameters are the diameter, the curvature radius as well as the type of the curvature. A spherical reflector is the result of the optimization process whereby the curvature radius and diameter depend on the used frequency and the considered sound pressure node. Based on this work, a reflector for $f = 40$ kHz and $l = 5/2\ \lambda$ with a diameter of $d = 20$ mm and a drilling radius of $r = 17$ mm was designed (figure refc2:horn).

Finite element method

The finite element method (FEM) offers numerical solutions for complex differential equations where no exact analytical solution exists. In order to apply FEM to the design of ultrasonic horns objects have to be transposed into meshes with a finite amount of elements. Computing the transport properties of vibrational propagation, this method offers an opportunity to model mechanical stress occurring in the sonotrode and can therefore be used to improve the practical functionality of this component.[70] For the design of the ultrasonic horns FEM calculations were performed by BAM 5.2. The results show an increased mechanical load at the rectangular transition to the radiating-plate. The sonotrode diameter at the transition to the radiating plate is $d = 8$ mm (figure 2.2) which lies in a critical range close to the calculated fatigue limit of $\sigma \approx 190$ MPa (figure 2.3). This indicates a possible breaking point at this transition which could .

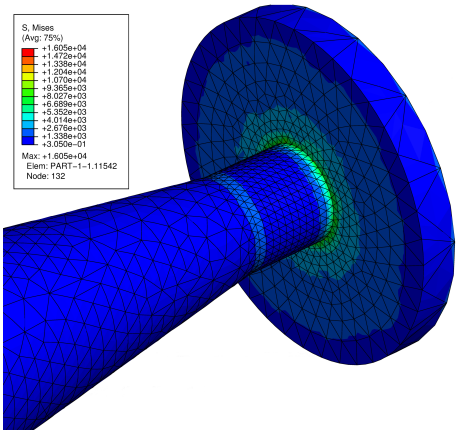

Fig. 2.3: Fatigue stress at the transition to the radiating plate calculated using Abaqus 6.7-1. The triangular mesh was refined at the transition to the radiating plate.

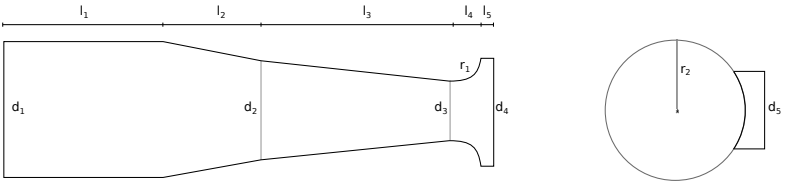

Fig. 2.4: Drawing of the second functional horn and reflector design ($d_1 = 17.6$ mm, $d_2 = 12.7$ mm, $d_3 = 7.8$ mm, $d_4 = 14.0$ mm, $d_5 = 20$ mm, $l_1 = 20.0$ mm, $l_2 = 12.0$ mm, $l_3 = 24.0$ mm, $l_4 = 3.5$ mm, $l_5 = 2.0$ mm, $r_1 = 3.5$ mm, $r_2 = 17$ mm).

Performance and mechanical stability

Two sonotrodes were designed and fabricated by the BAM machine shop regarding the equation for the speed of sound in solids (equation 2.2) and the approximation for long rods (equation 2.3). The sonotrodes were manufactured from Dural with lengths corresponding to half the wavelength of a 40 kHz sound wave in this specific alloy. With the shorter horn it was possible to levitate water droplets up to a volume of $V = 10$ µL ($d = 2.7$ mm) as well as polystyrene ($d = 2$ mm) and stainless steel globules ($d = 2.6$ mm) in the third node at a distance of $d = 5/2\ \lambda \approx 21$ mm. The second (longer) horn triggered the automated shutdown function of the power supply indicating that its resonance frequency is outside the operation range of $39 - 41$ kHz. This behavior demonstrates the long rod approximation as a valid assumption for the design of sonotrodes. As seen in the FEM calculations, there is a maximum in the local occurring mechanical stress load at the rectangular transition to the radiating plate (figure 2.3). After approximately one hour of operation the functional (shorter) horn failed at this transition.

In order to improve this critical region, a new sonotrode was designed. Instead of a rectangular transition a circular one was chosen. The new sonotrode (figure 2.4) was made from titanium

and was manufactured by MTH Herde. The resulting combination of the optimized horn and reflector was capable to levitate water droplets up to a volume of $V = 10$ µL as well as 2 mm polystyrene beads but not the stainless steel globules indicating a dissipation of the directed displacement in the desired direction around the curved transition. However, the new sonotrode offers an improved stability without any aging phenomena after a few hundred hours of operation, thus representing a suitable compromise between performance and endurance.

A major issue is the warming up of the levitation system caused by mechanical load due to the coupling of the individual collective vibrational degrees of freedom. This dissipated vibrational stress leads to an internal heating of the oscillating media. The change in temperature results in different speeds of sounds inside the transducer and horn which affects the automated frequency adjustment. Maintaining a constant frequency is crucial for levitation. Otherwise, the wavelength and therefore the optimal distance between horn and reflector will change and the droplet may become instable. It is extremely challenging to measure the increase in temperature directly due to high voltages at the piezo stack and the 40 kHz vibration at the horn. However, it is easily possible to measure the generators frequency which is directly proportional to the change in temperature. Figure 2.5 shows a plot of the frequency in dependence of the time from the moment the levitator was switched on. These results show the importance of a warm up phase of at least 30 min minimum to obtain stable levitation.

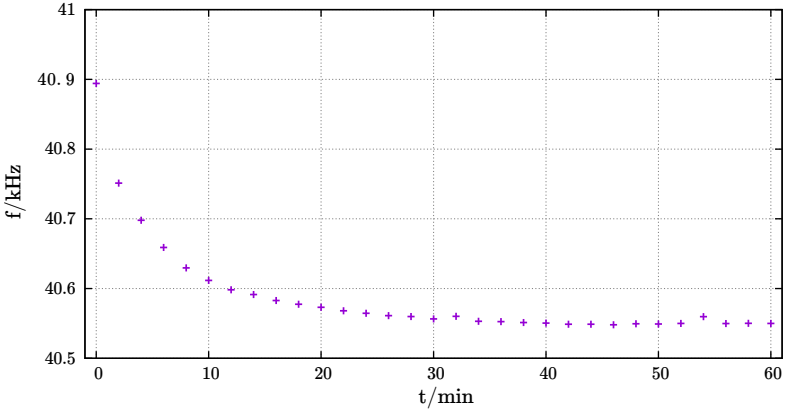

Fig. 2.5: Measured regulated frequency output using the titanium sonotrode for a period of $t = 60$ min and intervals of $\Delta t = 2$ min.

A simple way to characterize the levitation capabilities of this system is the measurement of the sound pressure acting on the reflector using a digital balance. This method directly yields the integrated acoustic radiation force in dependence of the reflector-sonotrode distance.[71] The experiment was performed by attaching a load cell to the rear side of the reflector. The load cell's signal was amplified by an INA125P instrumentation amplifier with precision voltage reference and was read out with an Arduino compatible microprocessor board (Atmega168). The results are presented in figure 2.6 and were compared to calculated levitation nodes following linear acoustics with an operation frequency of $f = 40.667$ kHz assuming a speed of sound of $c_s = 340$ m/s.

There is a significant deviation between the experimentally obtained and the calculated values. An ideal linear behavior would result in equal distances between the sound pressure maxima. Figure 2.6 indicates a deviation from this predicted trend which can be observed in the different spacings between the experimental and theoretically obtained values. In order to exclude possible discrep-

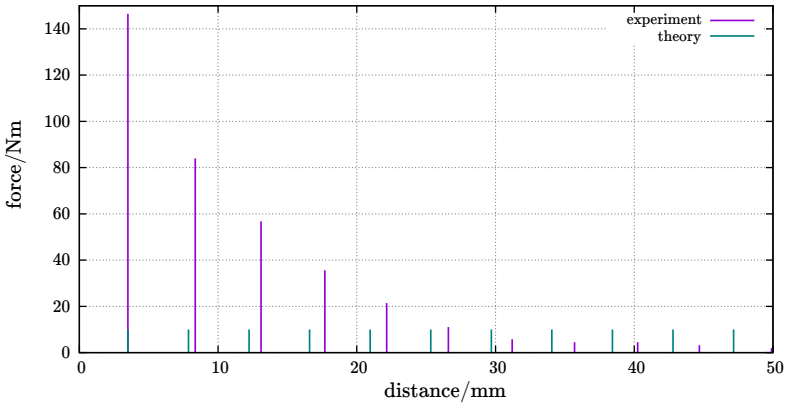

Fig. 2.6: Theoretically calculated and experimentally obtained maximums of the acoustic force. The theoretical values do not include intensity information.

ancies between both data sets that may be caused by factors like a differing speed of sound due to pressure and humidity fluctuations, a closer look at the trends in the experimental data set is necessary. In figure 2.7 the distance between one pressure node and the next larger one reveals a non-consistent behavior. This could be related to an energy transfer from the fundamental frequency to higher harmonics which would result in non-linear effects. Although, it cannot be proven that non-linear effects are causing this phenomenon or if it is simply caused by the interaction of the curved geometry of the reflector with the different shape of the different sound pressure maxima.

Hence, the plane-wave assumption that sound pressure nodes occur at the multiples of the half wavelength in air ($n \times \frac{1}{2}\lambda$) can only be seen as a rule-of-thumb. The real values strongly depend on the geometric parameters of the levitator and on the vibration amplitude and should therefore be obtained experimentally. A second effect that can be seen is the exponential decay of the acoustic force

with increasing node numbers. This shows the increasing influence of loss channels at higher nodes and is related to the Q-value of the resonator. This behavior has already been described for acoustic levitators [17] resulting in a trade-off between levitation potential and free accessibility of the droplet. Especially the first node is geometrically almost impossible to reach with a curved reflector. For a good accessibility at still acceptable steep sound pressure maxima, the third maximum at $l = 5/2\ \lambda$ was used throughout the remainder of this work.

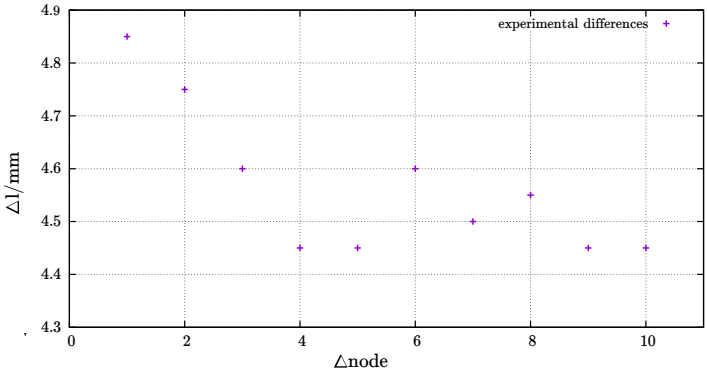

Fig. 2.7: Differences between experimentally obtained acoustic force maxima.

Numerical determination of the acoustic pressure distribution

The complex pressure field in the air region between the transducer and the reflector is calculated by a matrix method [60] based on the Rayleigh integral. According to the Rayleigh integral, the pressure distribution generated by a vibrating surface can be obtained by dividing the surface into infinitesimal area elements followed by the consideration that each infinitesimal element radiates a spherical

wave. The pressure distribution is determined by summing up the contribution of all spherical waves. Numerically, the pressure distribution generated by a transducer can be calculated by dividing the transducer surface into small area cells with dimensions much smaller than the wavelength, as shown in figure 2.8. In this figure, the transducer surface is divided into N cells and the acoustic pressure is determined in a set of points m in space. These points are distributed in a rectangular grid and the total number of points is M. The acoustic pressure p_m in a single point m generated by an ultrasonic transducer vibrating harmonically with complex displacement amplitude ζ is given by

$$p_m = \zeta \frac{\omega \rho c}{\lambda} \sum_{n=1}^{N} \frac{s_n exp(-jkr_{nm})}{r_{nm}}, \tag{2.4}$$

where $k = 2\pi/\lambda$ is the wavenumber, r_{nm} is the distance between the cell n and the observation point m and s_n is the area of the cell n. This pressure p_m given by equation 2.4 resembles only the acoustic pressure emitted by the transducer at a single point m. Equation 2.4 can be rewritten in a matrix form in order to obtain the pressure field in a set of points m that can change from 1 to M:

$$\begin{bmatrix} p_1 \\ p_2 \\ \vdots \\ p_M \end{bmatrix} = \frac{\omega \rho c}{\lambda} \begin{bmatrix} T_{11}^{TM} \\ T_{21}^{TM} \\ \vdots \\ T_{M1}^{TM} \end{bmatrix} \zeta. \tag{2.5}$$

The matrix $\mathbf{T}^{TM}$ of equation 2.5 represents the transfer matrix, where the complex displacement amplitude can be considered as an input and the pressure at a set of points m can be considered as the output. The elements of $\mathbf{T}^{TM}$ are given by:

$$T_{m1}^{TM} = \sum_{n=1}^{N} \frac{s_n exp(-jkr_{nm})}{r_{nm}}. \tag{2.6}$$

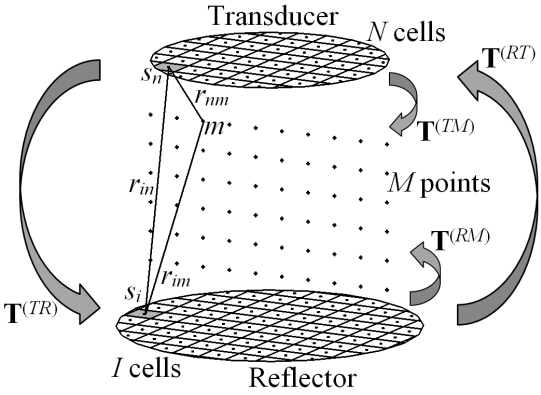

Fig. 2.8: Matrix discretization of the reflector and transducer surfaces and the air gap in between. [72]

Equations 2.4 and 2.5 are used to calculate the pressure generated by the transducer and do not take into account the multiple wave reflections that occur between the transducer and reflector. In order to simulate the wave reflections, it is necessary to add additional reflection terms to equation 2.4. When the wave emitted by the transducer reaches the reflector, it is reflected back and it interferes constructively and destructively with the emitted wave. For the case where the wave is reflected once, the resulting pressure at each point m can be calculated by:

$$\begin{bmatrix} p_1 \\ p_2 \\ \vdots \\ p_M \end{bmatrix} = \left(\frac{\omega\rho c}{\lambda}\right) \begin{bmatrix} T_{11}^{TM} \\ T_{21}^{TM} \\ \vdots \\ T_{M1}^{TM} \end{bmatrix} \zeta + \left(\frac{\omega\rho c}{\lambda}\right) \left(\frac{j}{\lambda}\right) \cdot \begin{bmatrix} T_{11}^{RM} & T_{12}^{RM} & \dots & T_{1I}^{RM} \\ T_{21}^{RM} & T_{22}^{RM} & \dots & T_{2I}^{RM} \\ \vdots & \vdots & \ddots & \vdots \\ T_{M1}^{RM} & T_{M2}^{RM} & \dots & T_{MI}^{RM} \end{bmatrix} \begin{bmatrix} T_{11}^{TR} \\ T_{21}^{TR} \\ \vdots \\ T_{I1}^{TR} \end{bmatrix} \zeta. \tag{2.7}$$

The first term of the right-hand side refers to the wave emitted by the transducer and the second term corresponds to the wave emitted by the transducer and reflected once by the reflector. It is interesting to note that the second term is calculated by the product of two transfer matrices, $\mathbf{T}^{TR}$ and $\mathbf{T}^{RM}$. The transfer matrix $\mathbf{T}^{TR}$ is used to calculate the complex pressure generated by the transducer at a set of points i in the reflector. Knowing the pressure at a set of points i, the pressure at a point m is determined by using the transfer matrix $\mathbf{T}^{RM}$. The elements of matrix $\mathbf{T}^{TR}$ are determined similarly to the elements of $\mathbf{T}^{TM}$:

$$T_{i1}^{TR} = \sum_{n=1}^{N} \frac{s_n}{e} xp \tag{2.8}$$

and the elements of $\mathbf{T}^{RM}$ are given by

$$T_{mi}^{RM} = \frac{s_i exp(-jkr_{im})}{r_{im}}, \tag{2.9}$$

where s_i is the area of the element i at the reflector and r_{im} is the distance between the point m and element i. Equation 2.7 can be rewritten in a compact form:

$$\mathbf{P} = \left(\frac{\omega\rho c}{\lambda}\right) \mathbf{T}^{TM}\zeta + \left(\frac{\omega\rho c}{\lambda}\right) \left(\frac{j}{\lambda}\right) \mathbf{T}^{RM}\mathbf{T}^{TR}\zeta. \tag{2.10}$$

Here, $\mathbf{P} = [p_1, p_2, \ldots, p_m]^T$ is a vector containing the complex pressure at each point m. Equation 2.10 considers only the direct wave emitted by the transducer and the wave that is emitted by the transducer and reflected by the reflector. To simulate an acoustic levitator it is necessary to consider more terms in equation 2.10. The

addition of other reflection terms to the right-hand side of equation 2.10 results in

$$\mathbf{P} = \left(\frac{\omega\rho c}{\lambda}\right)\mathbf{T}^{TM}\zeta + \left(\frac{\omega\rho c}{\lambda}\right)\left(\frac{j}{\lambda}\right)\mathbf{T}^{RM}\mathbf{T}^{TR}\zeta + \left(\frac{\omega\rho c}{\lambda}\right)\left(\frac{j}{\lambda}\right)^2\mathbf{T}^{TM}\mathbf{T}^{RT}\mathbf{T}^{TR}\zeta + \left(\frac{\omega\rho c}{\lambda}\right)\left(\frac{j}{\lambda}\right)^3 \cdot \mathbf{T}^{RM}\mathbf{T}^{TR}\mathbf{T}^{RT}\mathbf{T}^{TR}\zeta + \ldots \tag{2.11}$$

with

$$T_{ni}^{RT} = \frac{s_i exp(-jkr_{in})}{r_{in}}. \tag{2.12}$$

The numerical determination of the sound pressure is illustrated for the case of a single-axis acoustic levitator consisting of a transducer with a flat radiating surface with a diameter of 8.9 mm and a flat reflector with a diameter of 40 mm. The transducer operates at a frequency of 40.99 kHz and the separation distance between the transducer and reflector is 21.4 mm. The acoustic pressure in the air gap between the transducer and reflector was determined in a set of points located in a rectangular grid with a dimension of 40 mm by 20 mm and a discretization of 0.5 mm. The acoustic pressure was determined by using equation 2.11. The first term of the right-hand side of equation 2.11 corresponds to the wave that is emitted by the transducer. This wave is illustrated in figure 2.9(a). The second term of the right-hand side of equation 2.11 corresponds to the wave that is emitted by the transducer and reflected by the reflector. This reflected wave is shown in figure 2.9(b). In figure 2.9(c) the third term of the right-hand side of equation 2.11 is shown, which corresponds to the emitted wave after the 2nd reflection. Figure 2.9(d) presents the superposition of the multiple reflected waves.

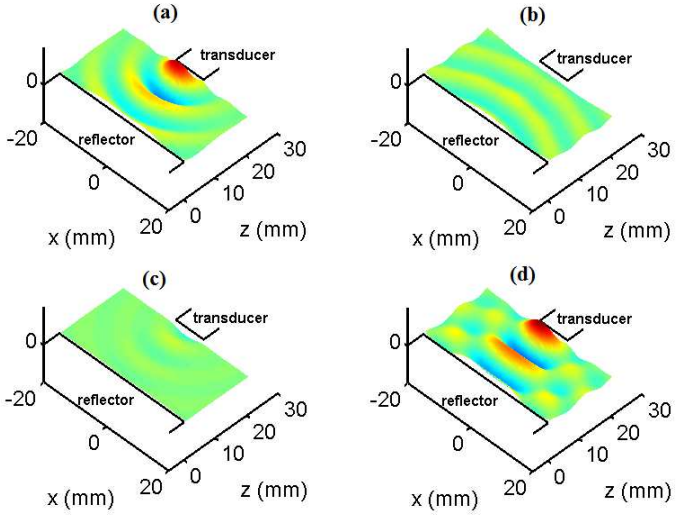

Fig. 2.9: Acoustic pressure in the air gap between the transducer and reflector: (a) Wave emitted by the transducer; (b) Wave after first reflection; (c) Wave after second reflection; (d) Sum of multiply reflected waves ($n = 20$). [72]

According to equation 2.13, the pressure field shown in figure 2.9 is calculated by taking the real part of the complex vector $\mathbf{P}$

$$\begin{aligned} p(t) &= Pcos(\omega t + \theta) = \mathrm{Re}\left\{Pe^{j\theta}e^{j\omega t}\right\} \\ &= \mathrm{Re}\left\{\mathrm{pe}^{\mathrm{j}\omega\mathrm{t}}\right\}. \end{aligned} \tag{2.13}$$

Levitation and sound pressure measurements

The experimental sound pressure measurements were performed using an electret microphone capsule with an outer diameter of 4.5 mm (Conrad Elektronik, Hirschau, Germany). To improve the resolution to a sub-millimeter scale, the capsule was mounted on a blunt syringe needle (900 µm outer diameter, 450 µm inner diameter). The preamplified signal was connected to a lock-in amplifier (SR830,

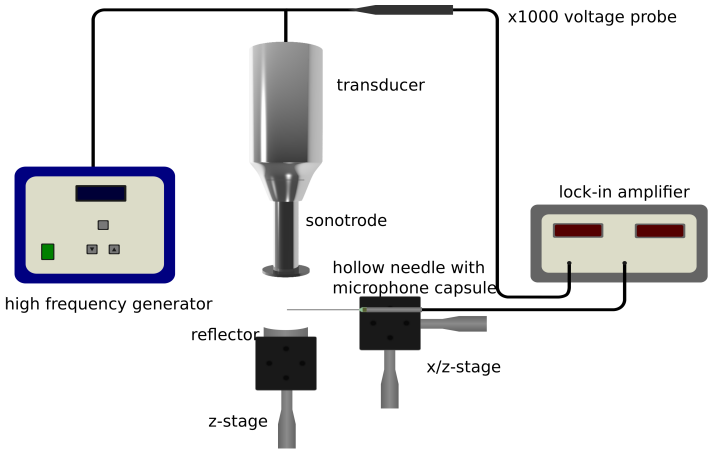

Fig. 2.10: Schematic drawing of the experimental setup used to scan the sound pressure distributions. [72]

SRS, Sunnyvale, CA) modulated by the ultrasonic generator frequency. The amplifier output was recorded using the A/D converter of an oscilloscope (TDS2024B, Tektronix, Beaverton, OR) connected to a PC. Both the x and the y channel were recorded. The 2D scanning process was implemented by using two motorized micrometer stages (Thorlabs, Dachau, Germany) driven by a home written LabVIEW software. The step size was 500 µm in x-axis and 355 µm in z-axis direction. The experimental setup is illustrated in figure 2.10.

Data processing

Assuming that the particles of the medium execute a simple harmonic motion with an angular frequency ω, two parameters are required to represent the acoustic pressure in a given point in space. The acoustic pressure can be represented by the amplitude P and the phase Θ, or alternatively, by a complex number with real and

imaginary parts. In the present work, both numerical and experimental acoustic pressures are represented by complex numbers. Numerically, the complex acoustic pressure is directly obtained by using equation 2.13. Experimentally, the real part of the complex pressure is obtained by readout of the x-channel of the lock-in amplifier (figure 2.11, left) whereas the imaginary part of the acoustic pressure is obtained by recording the signals from the y-channel (figure 2.11, middle). The figures shown in the results section show the modulus of the real and imaginary parts of the experimental data (figure 2.11, right).

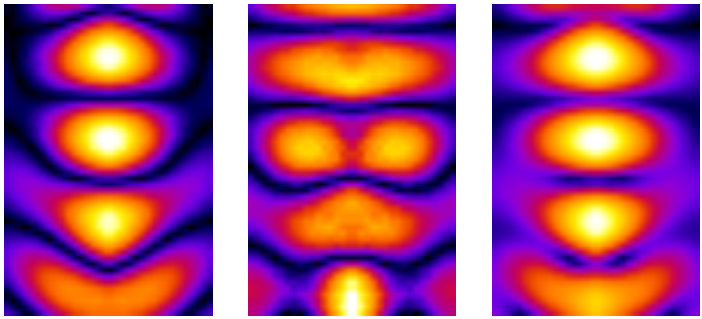

Fig. 2.11: Real part (left) imaginary part (middle) and the resulting modulus (right) of the sound pressure from experimental data for the combination of a radiating plate and a concave reflector. Figures were created using ImageJ with dark colors indicating low and light colors indicating high pressure intensities.[72]

The representation of the acoustic pressure by complex numbers can be used to generate animations with the pressure as a function of time in the air gap between the transducer and reflector. The animations are generated for both numerical and experimental data for each configuration of acoustic levitator. The animation of the

standing wave is generated by creating different frames for each value of t in the equation:

$$p(t) = Re\{p \exp(j\omega t)\} \tag{2.14}$$

where p is the complex pressure amplitude in a given position in space.

Results

The computationally predicted and the experimentally determined sound pressure distributions are shown in figure 2.12. As can be seen, the theoretical and experimental results exhibit a great similarity throughout the entire recorded space. This resemblance applies to all four sonotrode/reflector combinations. Note that the individual results cover different areas within the resonator, since the syringe needle for the acoustic measurements was always positioned not to touch any solid parts. This effect is especially pronounced in the case of the curved reflector since the elevated rim around the milled sphere strongly truncates the gap between the sonotrode and the reflector. Minor changes in the distances between the individual pressure nodes stem from different temperatures and, thus, different speeds of sound throughout the conducted experiments. All images exhibit the same general pattern of alternating high and low pressure regimes along the propagation of the emitted sound (vertical axis in figure 2.12). Albeit, the exact shape of the sound pressure distributions differs strongly for the individual resonator geometries.

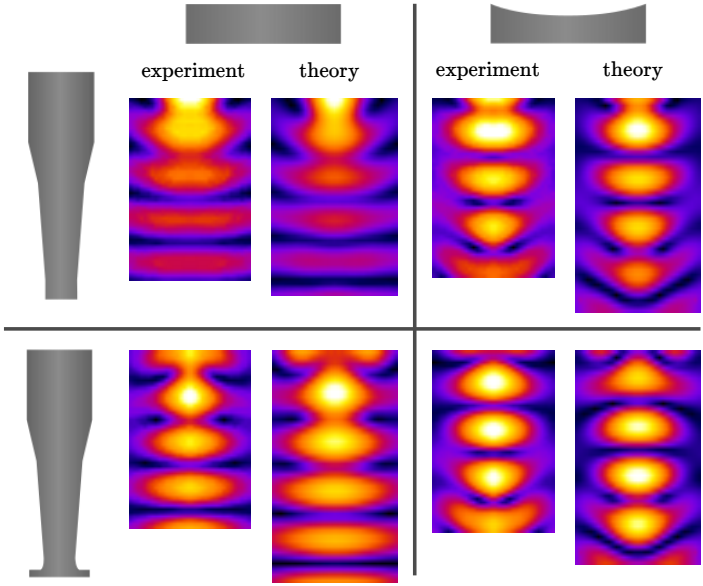

Fig. 2.12: Comparison between experimental and theoretical sound pressure distributions for all four different setups. [72]

This becomes apparent both in the shape of the sound field and in the relative intensity distributions. A direct comparison of the pressure fields on the left and on the right half of the figure (*i.e.* flat or curved reflector) shows distinct differences. On the left, the pressure shows a pronounced global maximum in close proximity of the sonotrode. Especially for the flat reflector, the further the standing wave propagates towards the reflector the weaker the local intensity maxima become. In other words, the emitted part of the sound is stronger than the reflected. This goes along with an axial broadening of the pressure nodes. When reaching the reflector, the wavefront is dissipated over a larger space than the reflector surface, thus not all of the incoming wave can be reflected. Since in levitation experiments the particles are trapped at the axial center of the resonator, this loss of axial confinement is undesirable. As

the right half of the figure shows, a better spatial confinement is achieved with a curved reflector. Comparable to optical resonators, this curvature of the reflecting surface refocuses the backscattered sound wave back towards the axial center of the cavity. This refocusing does not only result in narrower pressure nodes but also in an increase in overall pressure. Axial reconfinement of the curved reflector assures a larger part of the acoustic wave ensemble to be maintained in the levitator while the flat surface projects the acoustic field towards the outer perimeter of the resonator. These waves will eventually leak out of the cavity. For an ideal confinement, the radius of the curvature of the reflector has to be adjusted to the distance between reflector and sonotrode.[52]

A comparison between the sound field distributions obtained with and without a radiating plate attached to the sonotrode (lower and upper row in figure 2.12) shows an additional improvement in the overall sound pressure intensity by introducing a radiating plate. While the shaped reflector mostly affected the shape of the sound field perpendicular to the propagation direction, the plate increases the top down-symmetry of the standing wave due to a more confined emission. The sonotrode without a plate acts merely like an acoustic point source radiating over a large solid angle. This effect occurs when the transducers surface diameter is small compared to the wavelength and the emitted wave has an almost spherical shape. The sound field emitted by the radiating plate, on the other hand, has a bend shape that leads to an axial focusing of the emitted sound. This can clearly be observed in the form of the top sonic mode in the figures. This focusing on both sides of the cavity (by the plate on the emitting side and by the curved surface on the reflecting side) leads to an effective confinement of the standing wave inside the resonator. Hence, most of the emitted sound is trapped inside the cavity leading to a symmetric distribution. The confining

effect of the radiating plate is known to be caused by an excitation of circular overtones in the plate that lead to a displaced radiation source with respect to the radial position on the plate.[26]

In general, the simulation and the experimental approach coincide in confirming the combination of a radiating plate and a curved reflector to yield in the most stable levitation device. Furthermore, the conducted experiments demonstrate the good agreement of prediction and observation. This is a strong evidence that the proposed extended matrix method, albeit being fast, produces reliable results.

The fully functional acoustic levitator with a working frequency around 40 kHz designed for optimal levitation capabilities at 5/2 times the acoustic wavelength in air described in this chapter was used for the further experiments in this work. The next chapter will emphasize on a contactless laser desorption mass spectrometry sampling of levitated droplets.

Chapter 3

CO_2 laser ionization of levitated droplets

In this chapter a setup for the contactless probing of droplets levitated in the previously described ultrasonic trap with a mid-IR laser is presented.

Laser ionization of liquids

In the vast majority of today's mass spectrometric analyses of chemical compounds dissolved in liquids, the ionization and introduction into the mass analyzer is achieved by electrospray ionization (ESI).[31] This technique achieves high ionization yields of singly or multiply charged species. However, some analytes, such as polymers, require ionization techniques that lead to unambiguous charge states to avoid interference. These demands can be met by laser techniques such as matrix-assisted laser desorption ionization (MALDI).[46] Laser ionization of liquids for mass spectrometry has a long history. Early works in this field were hampered by the mismatch of the vapor pressure of liquid samples and the vacuum requirements of mass spectrometric analyzers. The first approach to circumvent this problem used a frit assembly similar to that originally designed for fast atom bombardment ionization.[73]

Based on the introduction of liquid jets in vacuum applications by Faubel and coworkers,[74] the group of Brutschy conducted pioneering laser-induced liquid beam ionization/desorption (LILBID) experiments.[75] Here, the infrared (IR) output of a carbon dioxide (CO_2) laser acted as the excitation source and for an effective coupling the solvent simultaneously functioned as the chromophore. It could be demonstrated that LILBID resulted in very gentle ionization of large biomolecules, but the technical demands on the vacuum system to maintain the necessary low pressure range were very high.

In recent years, the ion transmission efficiency of interfaces between vacuum and atmospheric pressure has improved significantly caused by advances in the vacuum pump technology. This progress inspired an entire new field of atmospheric ionization mass spectrometry[76;47] to develop. Taking up the LILBID experiments, a new set of studies impressively demonstrated the potential of ultra-

violet (UV) and IR laser vaporization/ionization of capillary supported droplets, ballistic microdroplets, and free liquid jets under ambient pressure.[77;78] To ensure an optimal absorption in most IR experiments, tunable optical parametric oscillators (OPO) were used as a light source. Due to the decoupling of the liquid from the vacuum system, the pumping requirements are moderate and a direct access to the intersection area of the laser and the liquid jet facilitates the sample introduction and optimization of geometric parameters.

While the results of UV experiments on liquids nicely resemble the typical features and behavior of MALDI studies on solids, the exact ionization process occurring in IR experiments is still under debate. Among the unanswered questions are the formation of ions despite the insufficient photon energy, the influence of net electronic charge in the droplet, the curvature of the sample surface, and the solvent composition.[77] The major obstacles to a better understanding of the underlying effects are the poor reproducibility of the experiments and the lack of total control of the liquids state variables. This control is best given by the use of static droplets. In liquid jets, the net flow of the liquid is limited by the nozzle diameter. Additionally, an electrostatic charging of the sample inside the pumps, for example in the vicinity of a piezo crystal or within the tubing can hardly be avoided in non-static experiments.

Here, the first IR-MALDI experiments on levitated droplets are described. Throughout these experiments, no charging of the droplet was needed and neither the stabilization of the droplet nor guidance of the formed aerosol droplets required additional external electric fields. Since a CO_2 laser was used for ablation/vaporization, glycerol was added to the solvent which functioned as the chromophore.

Experimental

A schematic view of the experimental setup is depicted in figure 3.1. Briefly, it consists of the acoustical levitation device described in the previous chapter, a laser, and a time-of-flight mass spectrometer (TOF-MS). A droplet consisting of $V = 6$ µL solution was confined in the central pressure minimum of an acoustical standing wave of the homemade acoustic trap and was positioned in front of the inlet capillary of the ambient pressure interface of a quadrupole guided TOF-MS (Tofwerk, Thun, Switzerland).

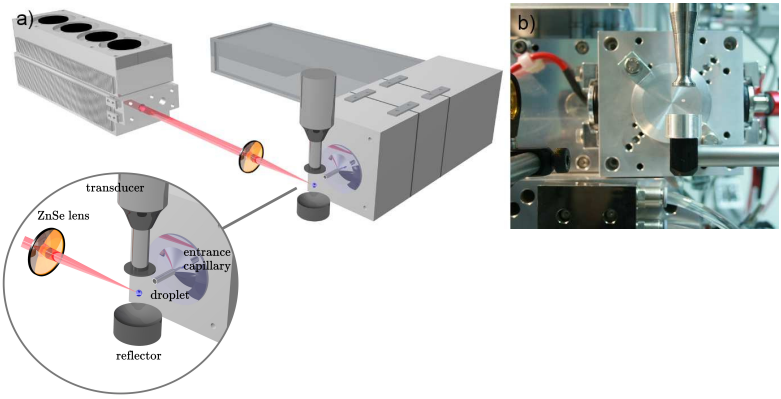

Fig. 3.1: a) Schematic visualization of the experimental setup including CO_2 laser, ZnSe lens, acoustic levitator with droplet and mass spectrometer. b) Photograph of levitated droplet in front of mass spectrometer inlet. The ZnSe lens can be seen on the left edge of the picture, indicating the laser beam path. [79]

The spectrometer briefly consists of four differentially pumped chambers. The first two, at working pressures of 2 mbar and 10^{-3} mbar, respectively, each include a quadrupole ion guide. In the third vacuum stage at 10^{-4} mbar, the ion packet is focused and accelerated into the orthogonal drift tube (10^{-6} mbar). The drift region is arranged in a double-reflectron geometry, in which the ions can

Table 3.1: Used MS parameters.

AP coupling			
Q1 entrance plate	−1 V		
Q1 Rf	5.1 MHz	Q2 Rf	4.6 MHz
Q1 Rf Amp	1 V	Q2 Rf Amp	2 V
Q1 front	1 V	Q2 front	−0.3 V
Q1 back	7 V	Q2 back	−2.7 V
Extraction			
Reference	−28 V	Ion Lens 2	−105 V
Deflector flange	−40 V	Deflector	−41 V
Drift zone			
U+low	37 V	U+high	900 V
U-low	780 V	U-high	60 V
Lens	700 V	Drift	3 kV
Refl. Grid	584.4 V	Refl. backplane	800 V
Hardmirror	0 V	Post Acc.	4.2 kV
MCP	2.4 kV		
Readout			
Mode	positive	Frequency	40 kHz

be tuned to a single-reflectron "V-shape" beam path or a triple-reflectron "W-shape" pattern. In all experiments presented here, the single-reflectron mode was used. For a detailed list of the used MS parameters please see table 3.1.

Liquid sample from the droplet was desorbed by a CO_2 laser ($\lambda =$ 10.6 µm, $P = 20$ W, $d = 1.8$ mm Diamond C55 A, Coherent, Santa Clara, USA), focused by a ZnSe lens (Thorlabs, USA, $f = 100$ mm). For pulsed exposition, the laser was chopped by a self-assembled optomechanical shutter with an opening time of 20 ms/pulse (400 mJ per pulse). All events in the pulsed experiments were synchronized by a delay generator (DG 535, Stanford Research Systems, Stanford, USA). For a visualization of the evaporation process, back illumination shadowgraphy experiments were carried out with a high-speed CCD-camera (Fastec InLine 1000, 1 kHz, San Diego, USA). L-Lysine (purum, crystallized >98 %), tryptophan ethyl ester (>99 %)

and trifluoroacetic acid (ReagentPlus 99 %) were purchased from Sigma-Aldrich, glycerol (anhydrous, BioChemica 99 %) was purchased from AppliChem. All samples were prepared in deionised water with a resistivity of 18.2 MΩ×cm.

Results and discussion

Laser desorption ionization

To visualize the plume formation, a high-speed CCD-camera (1 kHz) was used for synchronized shadowgraphy experiments. Selected snapshots of the obtained temporally resolved spatial distributions of the formed aerosol are depicted in figure 3.2. At the time the liquid droplet is hit by the laser beam (denoted as $t = 0$ ms in the figure), it changes its shape and first vapor formation can be observed opposite to the propagation direction of the laser. During the ≈ 20 ms of exposure, the droplet continues to elongate as it experiences a ballistic repulsion by the ongoing desorption. The aerosol is generated via two individual mechanisms, (a) direct vaporization and (b) ejection of smaller drops on a µm scale that subsequently evaporate. The driving force for this dispersion process can either be thermal energy remaining in the droplets or the strong ultrasonic field in the vicinity of the levitating pressure node. The dispersed particles are only visualized as a nebula, indicating a particle size significantly smaller than the area depicted onto an individual pixel on the CCD chip (5×5 µm). Considering the magnification factor of the used objective 1 pixel corresponds to ≈ 63 µm, *i.e.*, an upper limit of a droplet volume of $V = 0.13$ nL can be assumed in the nebula. Figure 3.2 reveals that the standing wave of the ultrasonic trap spatially confines the aerosol into two regions slightly above and below the original droplet. This spatial concentration is

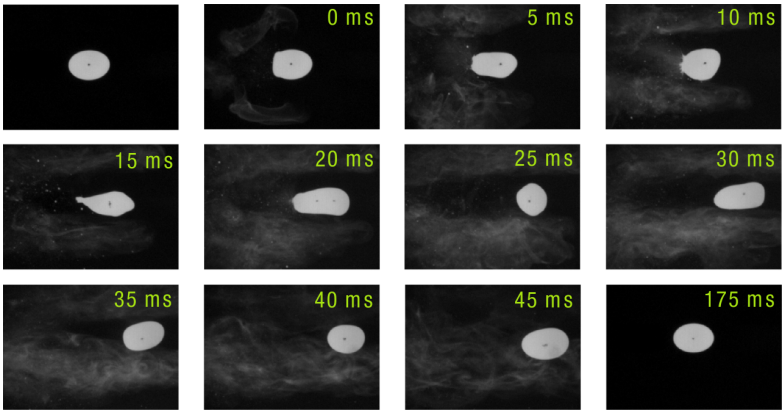

Fig. 3.2: High-speed shadowgraphy of droplet evaporation. 0 ms corresponds to the arrival of the laser beam, laser is coupled in from left to right. Droplet diameter is ≈ 2 mm [79].

believed to promote efficient coupling into the mass spectrometer. After 175 ms, the droplet has returned to the original position within the pressure minimum of the acoustic trap. Note that a shrinking of the original droplet cannot be observed with the resolution of the used camera. Thus, in a single experiment a maximum volume of a spherical shell of 0.5 pixel thickness (*i.e.*, 400 nL) is dispersed as an aerosol. When the laser-driven evaporation was conducted in front of the inlet capillary of the mass spectrometer, the vapor was transferred into the mass analyzer. A typical ion m/z distribution resulting from laser vaporization of a 1:1 glycerol water mixture is depicted in figure 3.3. It exhibits a progression of alkali adducts of n-glycerol clusters up to $n = 6$. The progression has a pronounced peak intensity at $n = 2$, while hardly any signal from the monomer or clusters without alkali metals can be observed. The strongest signal in the low mass range ($m/z \leq 200$) can be attributed to a protonated glycerol/water cluster. Remarkably, no signal out of the predominant CH_3OH or H_2O loss channel of the protonated

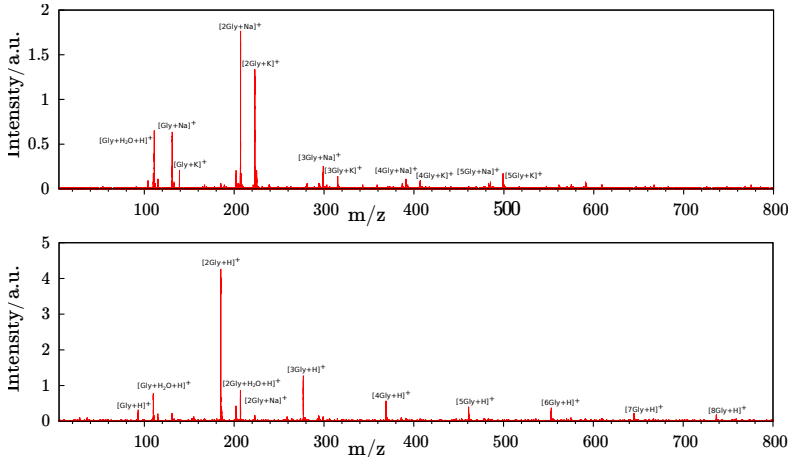

Fig. 3.3: IR-MALDI spectra of levitated glycerol/water (1:1) droplets. *Upper trace*: pure droplet; *lower trace*: 0.5 % TFA in droplet.[79]

glycerol monomer was observed. The addition of trifluoracetic acid (TFA) to the droplet results in an increase of the total ion count (TIC) and a suppression of the alkali ion formation (see figure 3.3). This behavior is typical for MALDI,[80] while in ESI applications, an incorporation of TFA was found to suppress signals.[81] In previous experiments, the main fragmentation pattern of the protonated glycerol dimer resulted in ions with m/z between 167 and 126.[82] However, even though the $[2\text{Glyc} + \text{H}]^+$ signal is the dominating peak in figure 3.3, no such fragments can be observed.

The overall enhancement of the detected ion signal due to TFA addition was quantified by subsequent measurements of the TIC out of 6 individual droplets containing different amounts of the acid. The results are shown in figure 3.4. The increasing acidity of the solvent leads to a steep rise centered around ≈ 1.75 % of TFA. At higher concentrations, a saturation with a total increase factor of ≈ 60 with respect to the non-acidified solvent occurs. This observed increase of ion yield can be understood by the increasing number

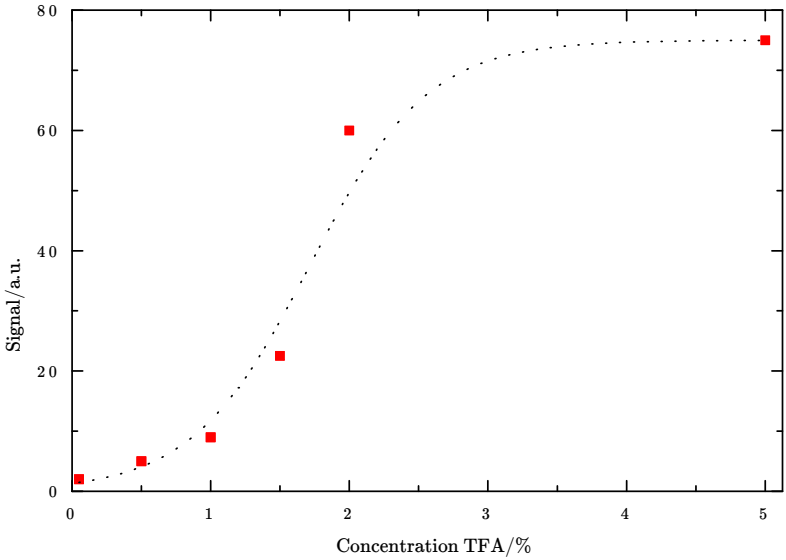

Fig. 3.4: Dependence of trifluoroacetic acid concentration on ion yield. The dashed line is merely a guide for the eye. [79]

of preformed ions in solution. In a subsequent experiment, lysine was added as a typical analyte to a droplet without TFA. As can be seen from figure 3.5, the obtained IR-MALDI spectra strongly resemble the results from the analyte free experiments, but three additional ion peaks are observed. The ion signal at the lower m/z of 147 can be assigned to the protonated analyte, while the peaks at $m/z = 239$ and 331 arise from clustering of lysine to a protonated glycerol monomer or dimer, respectively. Again, the addition of TFA to the droplet leads to a visible suppression of the alkali adducts. In the lower trace of figure 3.5, the spectrum of 10 mmol/L lysine solved in a 1:1 glycerol water droplet with TFA is shown. In contrast to figure 3.3 no signal enhancement can be observed. To understand this, note that even though in figure 3.4 a maximum increase of the ion count was observed for $\approx 3\,\%$ of TFA addition,

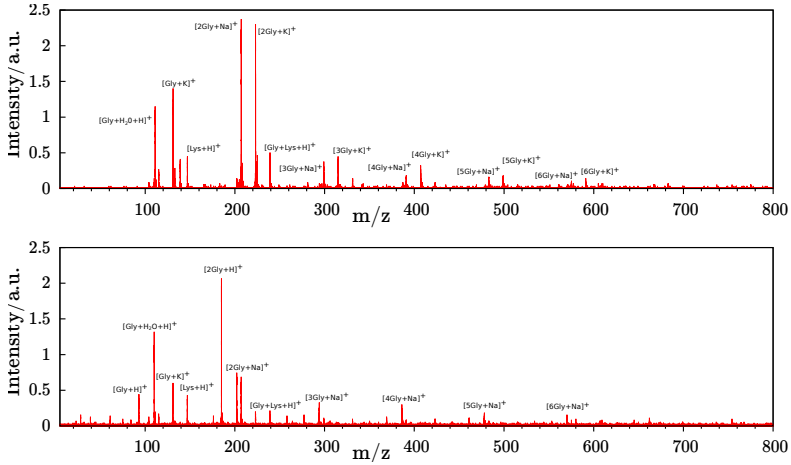

Fig. 3.5: IR-MALDI spectra of levitated glycerol/water (1:1) droplets wit 10 mmol/L lysine. *Upper trace*: pure droplet; *lower trace*: 10 mmol/L TFA in droplet. [79]

in this experiment the main focus was not the total ion count but a lysine spectrum without interference. Therefore, only an equimolar amount of 10 mmol/L of TFA was added. In both spectra, it can be observed that while the glycerol dimer has the strongest ion signal contribution, the lysine is preferentially detected as a monomer or clustered with only one glycerol. As can be seen from a direct comparison, the addition of TFA mainly changes the shape and intensity distributions of the glycerol containing ions, while the lysine containing signal mostly remains unaffected. Even though this behavior can be rationalized through the vast excess of glycerol, the larger proton affinity of lysine compared to glycerol should lead to a higher sensitivity of lysine signal to the pH of the solvent.

The new approach of IR-MALDI on contactlessly confined liquid matrices introduced here can contribute to gain insight into the complex processes involved in MALDI ionization.[83] A major advantage of liquid matrices is that no crystallization step is needed

in the development of newly improved MALDI matrices. While most chemical properties such as the proton affinity and spectral absorption maxima can readily be predicted prior to synthesis of a new matrix material, the crystallization process is highly unpredictable.[84]

Another difference is the energy introduced into the system in the desorption step. While in typical MALDI experiments UV lasers are utilized that are absorbed by electronic transitions in the matrices, the excitation with a far IR laser only leads to a vibrational excitation. Thus, excited-state proton transfer reactions[85] or unintentional multiphoton ionization can be excluded as a possible ionization channel. Furthermore, the viscosity and the high thermal conductivity of the droplets leads to an effective redistribution of the induced fragment recoil, thus resulting in low relative initial velocities and minimized thermal degradation of the analyte ions.

The ionization of the droplets, however, still remains unclear as it involves several individual steps: In the first step, the droplet evaporation can lead to a charge separation of preformed ions that are stable until detection in the mass spectrometer, *i.e.*, so called lucky survivor ions.[86] The separated charges would subsequently be localized on individual micro droplets that are repelled from the original droplet. Further evaporation of solvent leads to a coulomb explosion comparable to ESI. Subsequently, individual desolvated molecules can undergo collision-induced gas phase protonation. Due to the observations upon TFA addition and since no multiple charges could be observed, ESI-like mechanisms appear less likely and are postulated to play a minor role here. The other ionization pathways are both typical for UV-MALDI and cannot be distinguished between in this study. In a recent publication, Karas and coworker used selectively deuterated matrices to give compelling evidence for the coexistence of both, the lucky survivor model and the gas phase

protonation mechanisms as competitive pathways for the ionization in MALDI.[86]

Even though no quantitative statement on the involved ionization mechanism can be made here, some general estimations are possible: Despite the high viscosity of the glycerol matrix and the relatively fast ion formation in the present experiments, the protonation mechanism is clearly thermodynamically governed. This is obvious because the ionization probabilities strongly correlate with the proton affinities of the neutrals of PA_{wat} = 691 kJ mol^{-1}; PA_{glyc} = 87 kJ mol^{-1} and PA_{lys} = 996 kJ mol^{-1}.[87] While in the original droplet the chemicals were abundant at molar ratios of H_2O/glycerol/lysine $\approx 28:7:0.01$, water could only be detected in a cluster with glycerol whereas a strong lysine ion signal could be observed.

Postionization

To improve the analytical versatility and the limit of detection of laser desorption ionization two different postionization sources were designed and built. Due to the utilization of an additional postionization source the laser desorption process is merely required to transport sample from the droplet into the MS. This vapor is then subsequently ionized in an additional stage mounted between the ionization region and the entrance to the MS. Each postionization source was embedded into a Teflon block with a 300 µm capillary inlet for the vapor. Each block ended into a cylindrical reaction chamber with a length of 10.5 mm and a diameter of 9.5 mm. For the APCI a stainless steel spike was used as the high voltage electrode with an applied voltage of 2.5 kV and the entrance plate to the subsequent stage as the ground electrode. The spike was positioned with an angle of 45 ° to the ground electrode with a distance

of 3 mm. For the APPI experiments the spike was replaced with a VUV lamp (Hamamatsu L10706, $P = 6$ W, Japan) with a spectral distribution ranging from 115 nm to 400 nm which is capable to induce single photon ionization (figure 3.6).

The APCI spectrum of lysine shows a significantly different ion pattern along with a much higher intensity (figure 3.7). The main signals in this spectrum arise from glycerol as well as glycerol water adducts. The protonated lysine signal is low compared to the matrix molecules which dominate the spectrum. Comparing its intensity to the laser desorption/ionization (LDI) spectrum in figure 3.5, however, reveals an increase in intensity by the roughly 10^4 to 10^5. The variation in appearance of the signals can be explained with the different ion formation process. While in the LDI process the ion formation seems to be a statistical process influenced by the bulk phase parameters as well as the dynamics of the evaporation process, APCI is a gas phase ionization. Protonated water molecules and water clusters collide with the analyte molecules which can lead to a proton transfer reaction. The so formed protonated analyte ions can be detected in the following step. This gas phase protonation also explains the absence of alkali adducts. It would be possible to further simplify the matrix spectrum by heating up the inlet which would break up the clusters.

The APPI spectrum of the aromatic amino acid ester shown in figure 3.7 demonstrates one of the most significant advantages of this technique. The main features in the spectrum are the signals of the protonated molecule, as well as its dimer and its trimer, but neither water nor glycerol species can be observed. The reason for this behavior lies within the ionization energies (IE) for the different molecules. While the IE for water and glycerol are higher then the maximum photon energy emitted by the VUV lamp of 10.8 eV this

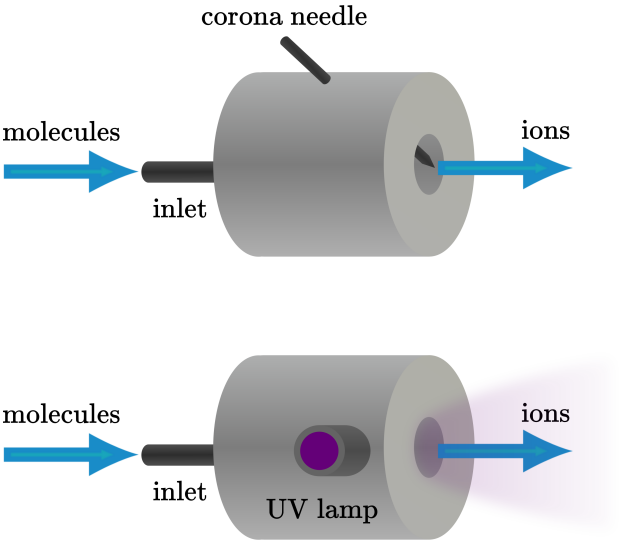

Fig. 3.6: Postionization setups utilizing a corona discharge (top) or a VUV lamp (bottom).

energy is sufficient to ionize a huge variety of organic molecules like aromatic metabolites, steroids and flavonoids.[41]

The newly developed coupling of acoustically levitated droplets with atmospheric IR-MALDI TOF-MS has proven to be a promising candidate for MS interrogation of microfluidic systems. Based on its simplicity, the approach is a capable tool to evaluate the influence of, *e.g.*, additional charge or acidity in the vaporized liquid on the ion yield to further elucidate ionization mechanisms and develop new ionization schemes. In an analytical context, the contactless confinement is an ideal environment for online pre-concentration in liquid samples prior to the probe step. Also the described laser desorption technique offers a versatile sampling with an affiliated post ionization. However, an additional heated transfer capillary would be needed to decluster the spectra and to promote a stable ion formation process. However, heating up the capillary to commonly

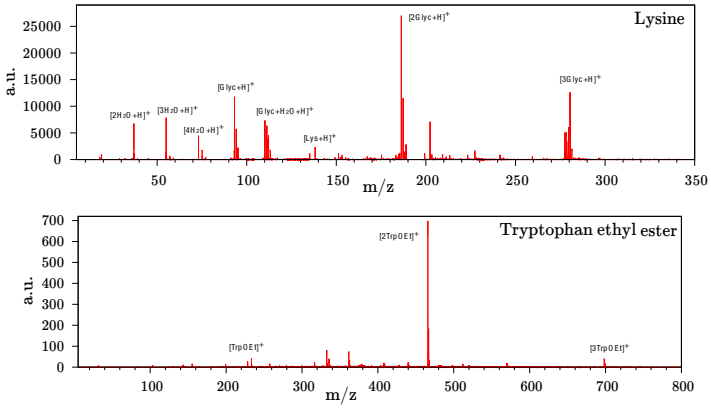

Fig. 3.7: Spectrum of lysine generated by APCI postionization (top) and tryptophane ethyl ester generated by APPI (bottom).

used temperatures around 300 °C would prohibit the use of standard vacuum seals and Teflon components and therefore requires a completely new ion source housing.

More importantly, the initial step of the desorption process requires a deeper investigation since the absence of strong electrical fields as well as the laser photon energy of $E = 0.12$ eV cannot explain the ion formation. It must therefore be assumed that the original formation of charged particles arises from the ejection of sprayed material itself. Therefore sonic spray ionization (SSI), also known to produce ions without any applied electrical fields (or lasers), was used as a model to understand the fundamental mechanisms of the ionization process in a spray in the next chapter.

Chapter 4

Characterization of sonic spray ionization sources using laser-induced fluorescence imaging and mass spectrometry

Sonic spray ionization can function as an advantageous model system for the simulation of the droplet plume generated by the laser pulse. Thus, enabling the elucidation of the ionization processes taking place during laser desorption

Development of sonic spray ionization

In the previous chapter, ionization of analytes by a mere charge separation *via* nebulization was observed. The nebulized solvent was not carrying a net charge (this has been verified by exposing the droplet to a strong DC field), thus a charge separation had to occur during the breakup of the droplet. To obtain a deeper insight in the occurring ionization mechanisms, sonic spray ionization was chosen as an advantageous model to simulate the spray plume generated by the laser pulse.

Spray ionization in the absence of high voltage potentials, heating and lasers is an especially mild form of ionization. It was discovered somewhat accidentally in 1994 by Hirabayashi *et al.*[88] The authors observed the most effective ionization at a gas evaporation speed of 1 Mach (which equals the speed of sound) and consequently named the technique sonic spray ionization (SSI). In contrast to electrospray ionization (ESI),[89] even extremely weakly bound complexes can be ionized intactly, the addition of redox buffers is not needed[90] and pure water can be used as solvent.[91] However, SSI lived in the shadow of its popular "sibling" ESI for many years until the Cooks group rediscovered it 10 years after its introduction for the ionization of intact non-covalently bound species.[92;93] In the following years, the group of Eberlin further improved the instrumental aspects of the technique. They successfully employed it as a desorption/ionization method[94] and further simplified it by utilizing the Venturi forces of the sheath gas flow instead of additionally pumping the solvent.[95] Owing to this progress, the name Venturi easy ambient sonic-spray ionization (V-EASI) was suggested. However, since the main experimental approach and the underlying ionization processes are the same, throughout this thesis the original nomenclature of SSI will be used. Despite its impressive progress,

SSI is still far from being established an analytical standard tool. In a recent publication by Antonakis *et al.* this was attributed to the fact that no sonic spray ion source was commercially available.[90] Thus, all experiments have to be conducted with self-designed and self-constructed spray sources. This hampers a direct comparison of results recorded in different laboratories. Therefore, an ion source based on a commercially available nebulizer for inductively coupled plasma applications was employed.[90]

The similarity in spectra obtained by SSI and ESI suggests that similar ionization mechanisms are involved.[96] The ionization process in ESI has been the subject of many experimental and theoretical studies.[97;98] In 2004, the droplet size/charge distribution in the ESI plume was determined by combined Doppler phase interferometry and ion mobility methods.[98] Other experiments exploited the solvatochromism of rhodamine 6G for recording spectrally filtered laser-induced fluorescence (LIF) images of the ESI plume.[99] Since the attachment of polar solvents, such as water, shifts the energetic positions of the electronically excited and ground states in the dye differently, this technique allows to measure the spatial distribution of naked and solvated molecules in the ESI plume, respectively.[99]

Consistent interpretation of theoretically and experimentally obtained results led to the conclusion that the formation of desolvated ions out of charged droplets can occur along two main pathways. In both cases each droplet shrinks by evaporation of uncharged solvent under maintenance of its original net charge until a critical charge density is reached. At this coulomb limit, the charge cannot be stabilized by distribution along the volume of the droplet and electrostatic repulsion induces a droplet rupture into at least two smaller droplets. These daughter droplets, however shrink at an even higher rate since their surface to volume ratio increases.

According to the so called charge residue model (CRM)[35] this concentration of charge carriers by evaporation, droplet rupture and subsequent ongoing shrinking is repeated until every daughter droplet merely carries a single charge. After evaporation of the remaining solvent, this charge cannot be distributed over several sub droplets and a single charge remains. If the final droplet also carries an analyte molecule, this is where the charge is localized and the desolvated charged analyte ion or charged cluster is formed by the residual charge after distribution.

In contrast, the ion evaporation model (IEM) claims that at a certain size of the droplets, stabilization of the charge will be energetically favored due to the evaporation of a charged molecule out of the droplet assisted by the increase in the field strength at the droplets surface.[36;100]

Several results can be found throughout the literature that strongly suggest the coexistence for both mechanisms.[101] The extent to which either of the individual pathways is followed depends on the charge density (both positive and negative) within the droplet and the polarity of the solvent/analyte. Since the droplets are in a thermodynamic equilibrium, eventually the turn towards either path will be balanced by Gibbs energy minimization ($\Delta G = \Delta H - T\,\Delta S$). Because the entropy change is equal for all processes leading to the formation of an ion from a droplet, the ultimate driving force is the ratio of the ions enthalpy of solvation $H_{sol}(A^+)$ and the free energy of the liquid to gas phase change of the solvent $H_{vap.}(Sol.)$. Since especially at high analyte concentrations (as observed at the end of several subsequent evaporation/rupture cycles) these values are typically not accessible, determination of the corresponding mechanism solely relies on empirical data. Even though sonic spray ionization has long been known to be a powerful analytical tool for weakly bound complexes, no work has been conducted so far to determine

the coexistence of the same pathways described above for ESI to be valid for SSI, also.

As opposed to ESI, a high voltage potential is not present in SSI. This arises the question of the source of the initial formation of charged droplets. To better understand the mechanism of SSI, a series of experiments combining macro photography and mass spectrometry have been conducted.[102] The results nicely resemble the droplet-size distribution obtained by ion mobility studies.[103] The aerodynamic breakup of charged microdroplets is a well studied phenomenon, since it occurs in everyday life processes like water flowing from a faucet, waterfalls, and especially clouds and forming thunderstorms.[104;105;106]. A generally accepted model of this breakup has been proposed by Zilch *et al.*.[102] According to this model, the aerodynamic forces acting onto a charged droplet with a surface determined by an electric bilayer form a liquid balloon consisting of a ring shaped annulus and a thin skinned bag. The Debye-Hückel charge distribution leads to an enrichment of positive charge within the thicker annulus while the remaining negative excess remains in the bag. Upon aerodynamic droplet rupture, this leads to large positive droplets and a fine aerosol carrying the negative counter ions. In addition to the explanation of charge separation during droplet rupture, this model explains the different behavior of positively and negatively charged species in spray ion formation.

This chapter will describe the setup and characterization of two individual sonic spray ion sources based on commercially available nebulizers. For a first evaluation of the spray formation based on LIF experiments, an airbrush vaporizer was employed. Throughout the remainder of this chapter, this ion source will be referred to as SSI source 1 or airbrush. For a more detailed study on the spatial distribution of ionization efficiency, a slightly more sophisticated setup consisting of a spray nebulizer designed for inductively

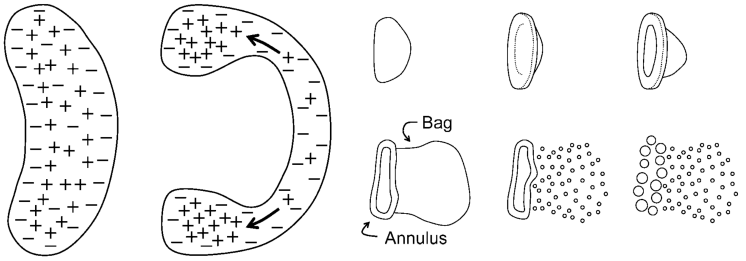

Fig. 4.1: Schematic visualization of the bag-mechanism for the charge separation during droplet breakup. Figure taken from Zilch *et al.*.[102]

coupled plasma (ICP) MS was applied. The latter was found to have a lower overall throughput of analyte solution making it more appropriate for elaborate, time consuming studies. In addition, the formed droplets were found to be smaller. This goes along with an evaporation closer to the spray nozzle and thus allows the direct mapping of the individual ion formation. This is necessary for an assignment of the contributing ion formation pathways. In consistence with the above mentioned, the obtained ion source will be referred to as SSI source 2 or nebulizer. The chapter will consecutively introduce the individual experimental designs followed by the obtained results.

Setup I

SSI setup I

A photograph and a scheme of the used spray source are depicted in figure 4.2 (a) and (b), respectively. A Sogolee HP-200 airbrush gun (Airbrushes Equipments Co., Republic of China) with an adjustable sample flow rate set to 10 $\mu L\,s^{-1}$ was used. A mixture of methanol (> 99.9 % pure, AppliChem, Germany) and water

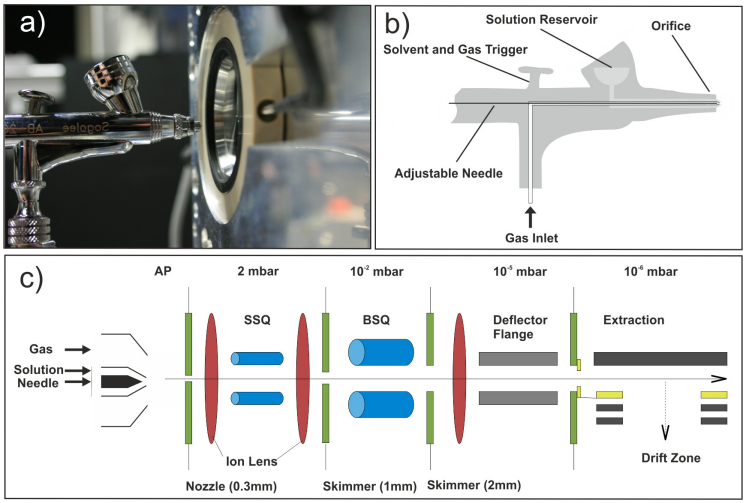

Fig. 4.2: Experimental setup: (a) photograph of the airbrush gun in front of the mass spectrometer inlet; (b) scheme of the used airbrush gun; (c) scheme of the atmospheric pressure coupling in the used mass spectrometer. [107]

($s < 2\ \mu\mathrm{Scm}^{-1}$, Carl Roth, Germany) (v:v 1:1) was used as solvent. To investigate the ion pattern of amino acids and peptides of different sizes, four different analyte solutions containing a concentration of 0.1 mmol L^{-1} L-lysine (> 98.0 %, Sigma-Aldrich, Germany), reserpine (98.0 %, Acros Organic, Belgium) and vancomycin hydrochloride (> 93.0 %, AppliChem, Germany) were vaporized. For lysozyme (LYZ) (molecular biology grade, AppliChem, Germany) a 1 mmol L^{-1} solution in neat water was used. Nitrogen (99.99 %, Air liquide, Germany) served as carrier gas at a typical stagnation pressure of 2 bar. The airbrush gun was mounted on an xy-stage for easy geometrical alignment and positioned collinear or parallel to the inlet of the mass spectrometer (API HTOF-MS, Tofwerk, Switzerland) with the same parameters as described in chapter 3. The distance between the spray nozzle and the inlet orifice was set

to 10 mm. The potential of the inlet nozzle was set to 20 V while the airgun was held at ground. Best results were achieved using an axial displacement of 3 mm between the cylindrical symmetry axis of the valve and the inlet, respectively. After passing the vacuum inlet (0.3 mm diameter), the ions pass three subsequent differential pumping stages before entering the orthogonal time-of-flight drift zone, see figure 4.2 (c). Mass spectra were accumulated over 3 s (60 s for lysozyme). At the given flow rate this corresponds to a sample consumption of 30 µL analyte solution or 3 nmol of analyte.

LIF experiments

For the LIF experiments, a solution of 220 $\mathrm{mg\,L^{-1}}$ rhodamine B (Lambdachrome, Lambda Physik, Germany) in a 1:1 methanol water mixture was nebulized with the airbrush gun. All experimental parameters were kept as in the MS experiments. The entrance plate was replaced by a plane ground electrode (15 mm distance to nozzle) to resemble the aerodynamic and electrical conditions present in front of the mass spectrometer (assuming that the spray flow is much higher than the vacuum pull). The fluorescence was excited using a frequency-doubled Nd:VYO_4 diode-pumped solid-state laser (532 nm, 500 µJ per pulse, 25 ns full-width half-maximum pulse width, BLADE IR 25, Compact Laser Solutions, Germany) expanded to a spot size of 20 mm using a Keplerian telescope. Depending on the experiment, the repetition rate was set to 1 kHz or 20 kHz. Fluorescence maps were acquired using an EOS 550D camera with an EF-S 18-55 mm IS II objective (both Canon, Japan) mounted in a retro position at right angles to the propagation direction of the laser beam, see figure 4.3. The shutter of the camera and the trigger of the laser were synchronized by a delay generator (DG 535, SRS, USA). Detection of the incident laser light was avoided

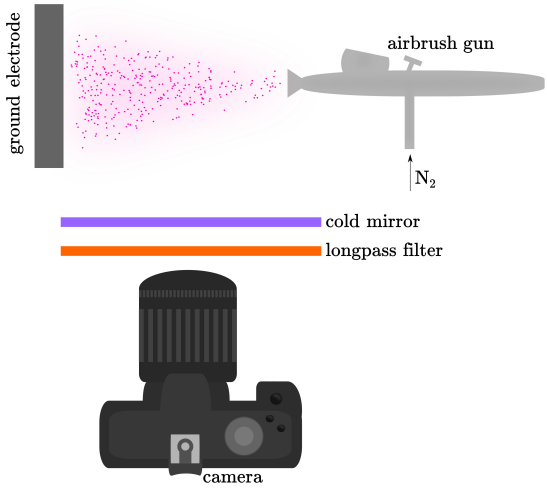

Fig. 4.3: Scheme of the used LIF setup. Please note that the direction of the laser propagation is orthogonal to the visual plane.

by the use of a 2" longpass filter (OG 515, Schott, Germany). For the analysis of the desolvation process, a 2" ultraviolet (UV) cold mirror (FM204, Thorlabs, Dachau, Germany) with a half-maximum spectral cut-off that was previously experimentally determined to be $\lambda = 556$ nm, was introduced between the spray cone and the camera.

Characterization of setup I

SSI-MS

The recorded spectra of lysine, reserpine, vancomycin and lysozyme are depicted in figure 4.4. The individual analytes that cover a wide range of molecular masses can readily be detected. In the case of lysine, with a molecular weight of 146 Da, see figure 4.4 (a), the predominant feature in the upper mass range of the recorded spectrum

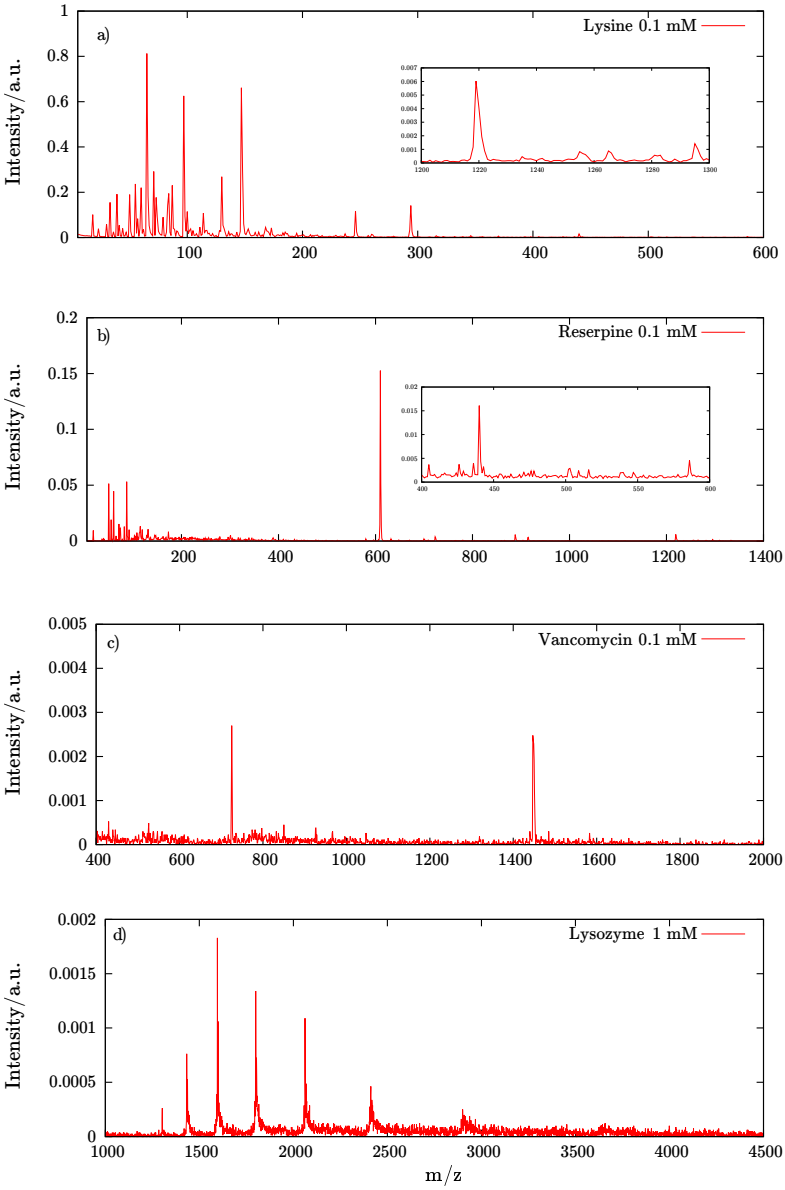

Fig. 4.4: Recorded SSI mass spectra for solutions of (a) lysine (146 Da), (b) reserpine (609 Da), (c) vancomycin (1450 Da) in a 1:1 MeOH/H_2O mixture and (d) lysozyme (14.3 kDa) in neat H_2O only. [107]

is the protonated cluster progression $[Lys_n+H]^+$. These clusters of up to four lysine molecules can be detected with a good signal-to-noise ratio [$S/N = 806, 444, 70$ and 17 for monomer, dimer, trimer and tetramer, respectively; see figure 4.4 (a) inset]. The ions detected in the low mass range can be attributed to protonated solvent clusters such as $[(H_2O)_nH]^+$, $[(MeOH)_nH]^+$, $[(MeOH)_n\times(H_2O)_mH]^+$ and their respective alkali adducts.

The main feature in the reserpine spectrum, see figure 4.4 (b), is the protonated monomer. The ion signal of the dimer can also be observed, albeit with a two orders of magnitude lower intensity. Compared to the lysine spectrum, the ion signals in the low mass range are much less pronounced which is caused by the analytes different pK_a values.

In the spectrum of vancomycin solution the doubly protonated analyte yields the strongest ion signal, see figure 4.4 (c). The singly charged monomer has a slightly lower intensity and is the second most pronounced feature. In contrast to the lighter lysine and reserpine, no cluster formation could be found. This result nicely coincides with typical ESI experiments for which the usual threshold for doubly charged ion formation of $m = 1$ kDa has been established.[108] This "one charge per kilodalton" rule of thumb derives from the high proton affinity of terminal nitrogen and nitrogen in the side chains of the amino acids lysine, arginine, proline and histidine. With the even heavier polypeptide lysozyme, the whole spectrum is governed by a series of multiply charged monomers, see figure 4.4 (d), comparable to ESI experiments. It is known that in ESI an especially broad charge state distribution can be observed from denatured peptides.[34] The observed charge state distribution is asymmetrically centered around the $[LYZ + 9H]^{9+}$, with the lowest observable charge being $[LYZ + 5H]^{5+}$ and the highest being $[LYZ + 11H]^{11+}$. The observed ion patterns can be briefly

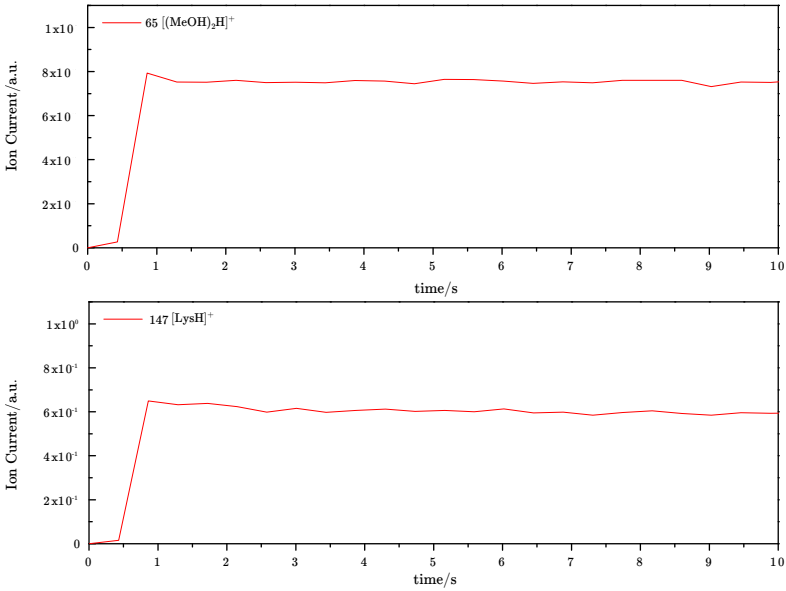

Fig. 4.5: Temporal trace of the $[Lys+H]^+$ and $[(MeOH)_2H]^+$ ion signals of a 0.1 mmolL^{-1} L-lysine solution.[107]

summarized as follows: Small molecules tend to form ion clusters while larger molecules preferentially form multiply protonated ions. This resembles previous findings for both SSI and ESI.[34;109] To demonstrate the stability, a temporal trace of the $[Lys + H]^+$ and $[(MeOH) + 2H]^+$ ion signals out of lysine solution is depicted in figure 4.5. For a visualization of the reproducibility, figure 4.6 shows two individual lysine spectra recorded with an interval of two weeks and a deviation from the mean value of 11 %

LIF

The observed SSI-MS spectra strongly resemble ESI-MS spectra, as outlined before. This is somewhat counterintuitive since the ion formation models for ESI[110] rely on charge separation by the applied

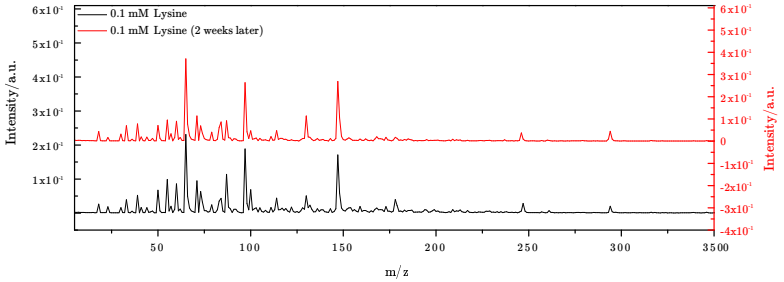

Fig. 4.6: Two individual SSI spectra of 0.1 mmolL^{-1} L-lysine solution recorded in a time interval of two weeks. The red spectrum has been biased for visualization. [107]

electric field. A similar ionization mechanism in the absence of high voltage can result from statistically charged microdroplets. Another plausible explanation is the so-called "bag mechanism" which postulates that a charge separation occurs during the aerodynamic breakdown of the microdroplets. [102] To gain a better understanding of the underlying processes in the SSI-MS experiments, accompanying pulsed LIF studies were conducted. Figure 4.7 (a) depicts an image of the fluorescence of the rhodamine B solution expanded under identical conditions as in the SSI-MS experiments. During the camera exposure time of 2 s the solvent solution was illuminated by the laser with a repetition rate of 1 kHz. The expanding jet has a conical shape with an opening angle of $2 \times 15°$. Perpendicular to the propagation direction of the jet, the plume exhibits a Gaussian shape that broadens while moving away from the orifice. Comparable plume shapes have been found for ESI experiments. [99] For further analysis, the red channel of the RGB image was converted into a grayscale image, representing the spectrally integrated fluorescence. The result is shown as an overall fluorescence map in a false color representation in figure 4.7(b). The expanding cone is of cylindrical symmetry along the expansion direction because

of the cylindrical shape of the orifice. The fluorescence intensity detected on the camera chip is thus a projection of a cylindrical object. If the detector is aligned parallel to the axis of symmetry, this projection can be expressed as the Abel Transform of the original three-dimensional (3D) distribution (for example, see Renth and Riedel):[111]

$$F(y) = 2\int_{y}^{\infty} \frac{f(r)rdr}{\sqrt{x^2 - y2}} \tag{4.1}$$

A numeric inversion of the Abel Transform was undertaken using a MATLAB code. Since the inverse Abel Transform has been the subject of many scientific publications (see Hansen and Law[112] and references therein), the mathematical details are not given here. Briefly, the inversion was computed following a Fourier-Hankel cycle.[113] The result is the original 3D distribution of the spray cone. This distribution is shown in figure 4.7(c) as a meridional slice. Owing to the cylindrical symmetry, this slice contains all the information of the original 3D distribution. It is clear from figure 4.7(c) that the spray has the form of a filled cone with its highest fluorescence intensity in the center. The mere 2D projection could have stemmed from a hollow distribution. This, however, does not coincide with the fact that the highest ion yields were observed when the central part of the expansion was aligned 3 mm off the axis of the orifice of the mass spectrometer.

Rhodamine B exhibits a pronounced solvatochromism.[114] Upon solvation, the energetic position of the S_0 ground state and the S_1 excited state shift with respect to each other and the band in the fluorescence spectrum experiences a redshift. The wavelength of maximum fluorescence of solvated rhodamine was found to be $\lambda = 577$ nm (MeOH)[115] and $\lambda = 580$ nm (H_2O),[114] while the excited molecules without a solvent cage emit light with a maximum of $\lambda = 542$ nm.[116] The optimal excitation wavelength also shifts

accordingly, from $\lambda = 531$ nm to $\lambda = 557$ nm in the presence of water.[116] Both transitions can thus be pumped by the frequency-doubled Nd:YVO_4 laser at $\lambda = 532$ nm. A subsequent spectrally resolved observation of the fluorescence distribution will allow identification of the solvation state of the molecules. For this purpose, a UV cold mirror with a half maximum cut-off wavelength of $\lambda = 556$ nm (transmission at $\lambda > 556$ nm, reflection at $\lambda < 556$ nm) was introduced into the beam path of the collected light. Therefore, the collected fluorescence signal in the presence of the mirror mainly represents the light emitted from solvated molecules. The result is depicted in figure 4.7(d). A direct comparison with figure 4.7(b) clearly shows that most of the rhodamine B molecules in the spray cone are solvated. To visualize the subtle effect of desolvated molecules on the overall fluorescence signal, the difference between figure 4.7(b) and figure 4.7(d) *i.e.* the difference between all molecules and solvated molecules is shown in figure 4.7(e). This LIF map primarily shows the fluorescence below $\lambda = 556$ nm, that is light emitted by desolved molecules. The difference is 14 % for integrated intensities and around 50 % for the region with the highest intensity values. It can be seen that desolvation of the molecules happens preferentially in the outer region of the expansion zone. This could be explained by the fact that the acceleration of the liquid droplets occurs *via* Venturi forces that act on the outer region of the liquid column in the nozzle. This could lead to a stronger acceleration of the droplets in the outer region of the orifice. Another way to interpret the preferred desolvation in the perimeter of the cone is the fact that closer towards the center, a sonic expansion forms zones of silence. Within these volumes no or only little collisions with ambient gas molecules like atmospheric N_2 occur. Thus, the observed anisotropy of the solvation state could indicate that the stripping of the solvent molecules happens primarily by inelastic

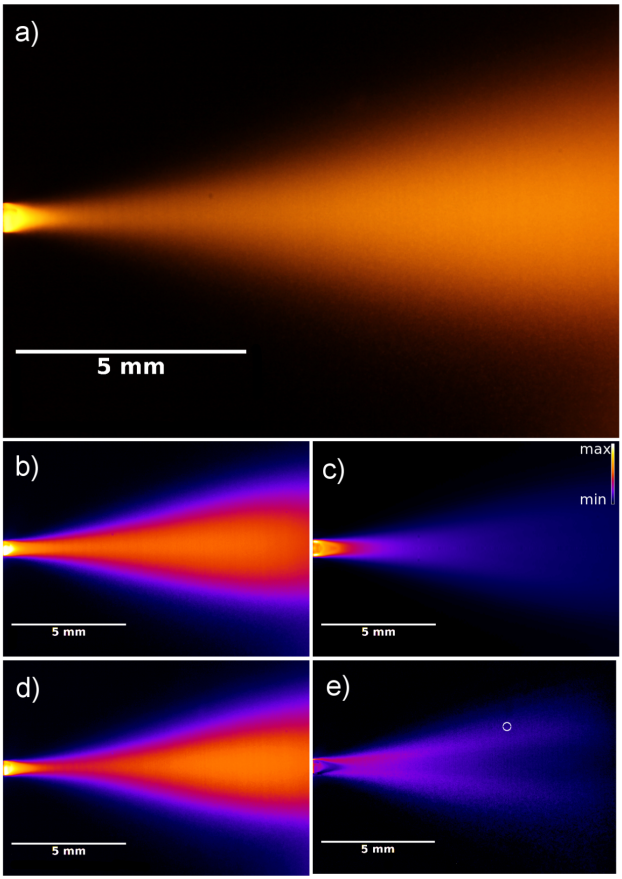

Fig. 4.7: **LIF images of the SSI cone: (a) fluorescence signal of rhodamine B in 1:1 MeOH/H_2O accumulated over 2000 excitation laser pulses; (b) overall fluorescence intensity map in false color representation (see inset); (c) meridional slice through the reconstructed 3D distribution of (b); (d) overall fluorescence intensity through the UV cold mirror - only fluorescence above 556 nm (mainly solvated rhodamine B) is detected; (e) difference image between (b) and (d) - only fluorescence below 556 nm (mainly desolvated rhodamine B) is observed. The circle represents the inlet position in the MS experiments.** [107]

scattering processes with surrounding slow gas molecules. However, a detailed explanation needs further investigations. A comparison between figure 4.7(d) and figure 4.7(e) reveals that throughout the entire expansion cone most of the molecules stay solvated. Yet, no analyte solvent clusters were visible in the MS spectra. This gives strong evidence for a subsequent desolvation throughout the ion path in the mass spectrometer. It can be assumed that heating of the carrier gas stream would result in a more effective desolvation of the ions: However, in the experiments conducted so far no additional heating was applied. The exact formation of the detected desolved ions is unclear. Most plausible is a solvent vaporization in the intermediate pressure region, caused by the increased relative vapor pressure of the solvent, or the interface between atmospheric pressure (AP) and the acceleration towards the high vacuum inside the MS. Since the solvation state of the formed ions strongly impacts the detected ion pattern,[101;117] comparable LIF studies in the individual stages along the differential pumping of the AP interface towards the mass analyzer could be conducted. Another approach towards the desolvation/ionization process is the mesoscopic study of individual microdroplets. In order to obtain information about the droplet-size distribution and the droplet velocities, another set of experiments was conducted using the same setup as for the mere visualization of the spray cone. For spatially resolved identification of single droplets, the repetition rate of the excitation laser was increased to 20 kHz while the exposure time of the camera was set to 1/ 1024 s. A corresponding image can be seen in figure 4.8(a). The image contains several microdroplets that were illuminated multiple times. After assignment of various imaged particles to the same droplet, the particle velocities can be calculated by connecting imaged particles to subsequent visualizations of the same droplet while traveling on its characteristic trajectory. For all observed droplets

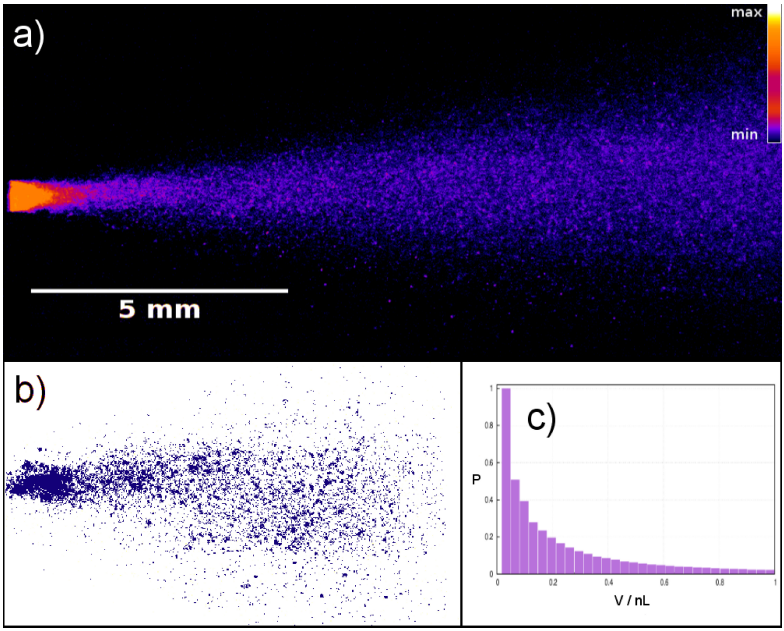

Fig. 4.8: Single microdroplet studies: (a) multiple illuminations of expansion cone in a false color representation; (b) single illumination of the expansion cone as binary map; (c) histogram of the droplet-volume distribution. [107]

the obtained velocities were in the range of $20 - 40$ ms^{-1}. These results are in almost perfect agreement with earlier work that presented values between 15 m s^{-1} and 55 m s^{-1}.[102] The velocity of the expanding gas can be estimated using gas dynamics following the formula for an adiabatic expansion against atmospheric pressure:[88;118]

$$P = [1 + 0.5(\gamma - 1)Ma^2)]^{\gamma(\gamma-1)} \tag{4.2}$$

in which P is the stagnation pressure, Ma represents the Mach number and γ denotes the heat capacity ratio of nitrogen. The used stagnation pressure of 2 bar leads to a gas velocity of $\sim$ 1 Mach.

This means that the expanding gas has sonic speed, whereas the solvent droplets that are accelerated by the expanding gas *via* Venturi forces have a lower final velocity by a factor of $25 - 50$. To understand the vaporization process, it is also important to determine the microdroplet size. Thus, single exposure images were recorded. This was achieved by decreasing the repetition rate of the laser to 1 kHz, which roughly coincides with the exposure time of $1/1024$ s of the camera. The retrieved images were background subtracted and transformed into binary data sets by a thresholding algorithm (ImageJ, National Institutes of Health, USA). An example is shown in figure 4.8(b). Subsequently, ImageJ was used to run an automatic particle size analysis. After converting the images to binary data sets by defining an intensity threshold value for the differentiation between droplets and the background, the algorithm calculates the volume of each single droplet under the assumption of almost spherical particles. To obtain sufficient statistics, this experiment was repeated until 350,000 individual microdroplets had been evaluated. The resulting droplet size distribution is shown in figure 4.8(c). The conversion from the measured area in the images to the volume given in figure 4.8(c) was made under the assumption of spherical droplets. The droplet size distribution follows an exponential decay with a maximum at a volume of 30 pL. This corresponds to a droplet diameter of approximately 40 µm. This coincides with the spatial resolution of the used camera setup. Hence, it is possible that even smaller droplets are formed than this instrumental resolution limit. The results lie between the size determined by the stroboscopic photography experiments of Zilch *et al.*[102] (10 µm) and the results obtained by an aerodynamic particle size study (0.8 µm).[103] The latter aerodynamic study resulted in a bimodal particle-size distribution with maxima at diameters of 0.7 µm and 0.9 µm. Since this is below our spatial resolution, no direct comparison can be

done. Zilch found a monoexponential distribution with a maximum at a droplet size of 10 µm in diameter,[102] but the maximum resolution of the used camera is not stated in the publication so it is unclear whether the deviation is caused by experimental limitations or stems from different expansion conditions. Moreover, no further conclusion of the effects of CRM and IEM in the SSI process can be drawn. Thus, a slight adjustment of the used setup is required to expand the investigation of the underlying ionization processes into a second spatial dimension. Since the results obtained from setup I clearly indicate an incomplete desolvation throughout the entire expansion cone, for a closer study of the exact desolvation mechanism it is crucial to move the desolvation closer to the expansion orifice. This can most directly be achieved by a sonic spray setup that yields in a finer spray, *i.e.* smaller initial droplets that evaporate faster.

Spatially resolved mass spectral investigation of charge state distribution in a sonic spray cone

Both, the experimentally observed anisotropic desolvation behavior as well as the theoretically predicted ion formation by Zilch *et al.*[102] should result in a strong dependence of the observed ion yields on the exact spatial position within the spray cone. This anisotropy of ionization efficiency should be reflected in the geometry of the positioning of the sonic spray source relative to the low pressure inlet of the mass spectrometer. The obtained position dependence in ion yield has a direct effect on the performance of any analytical study using a spray ion source, since typically experiments are conducted at a fixed geometry. Thus, by iteratively changing the relative position of the used nebulizer with respect to the inlet, the intake volume was mapped for a spatially resolved interrogation of the ion formation probability at different points in the spray cone. This experiment will be described in more detail on the following pages.

As a first analyte, myoglobin (from horse heart, $> 90\,\%$, Sigma Aldrich) was used. This choice was based on several considerations: Myoglobin is a molecule of real analytical interest and typically serves as a well understood test candidate for ionization process studies (*e.g.* Iavarone *et al.*[119]). Myoglobin can be detected in positive and negative ion mode. Both, the positive and negative spectra of Myoglobin are known to include heme and two broadly distributed series of charge states, attributed to holo-myoglobin (intact protein) and apo-myoglobin (myoglobin lacking the heme unit). The exact maxima of the charge state distributions correlate to the folding of the molecule which is affected by the solution conditions

and the desolvation process or the spray source. The described properties result in rich mass spectra, *i.e.* each individual mass spectrum contains a plethora of information. This is greatly beneficial since all the information, *i.e.* the relative intensities of individual charge states are included in each single spectrum and do not have to be accumulated by adding up information of subsequently recorded spectra. This makes a direct comparison much more robust towards long term fluctuations. Since in mapping experiments a positive and a negative spectrum have to be recorded for each pixel, one universal acquisition of a sum of features instead of the sum of acquisitions with single features also drastically shortens the amount of time needed for a thorough study.

Conducting the experiments, a maximum of ion sensitivity combined with a minimum on sample throughput had to be realized. Therefore, instead of the previously used TOF instruments, a linear quadrupole ion trap mass spectrometer (LCQ-Advantage, Thermo-Finnigan) was used while a modified ICP nebulizer with minimized sample consumption served as the SSI source. This combination has been reported previously by Antonakis *et al.* to be a powerful tool for the detection of weakly bound complexes and sensitive biomolecules.[90] Thus, the experiments were conducted within the scope of a collaboration in Spiros Pergantis' laboratories in Crete.

Results from setup II

All experiments were performed using a Thermo-Finnigan LCQ-Advantage ion trap mass spectrometer. The ion trap's calibration was verified every day using STFA as described in Antonakis *et al.*.[90] The mass spectrometer was operated with a capillary temperature of 300°C, a temperature that had already been found to provide maximum sensitivity for protein analysis. All spectra 20 scans

(3 microscans/ 400 ms each) from $m/z = 150$ t $m/z = 2000$ were accumulated with a capillary voltage of 90 V in positive mode, −100 V in negative mode and a tube lens offset of 80 V in positive mode and −105 V in negative mode.

Based on previous experiments, a nitrogen driven ICP nebulizer (Meinhard SB-50-A1) was used as the SSI source.[90] To further reduce the flow rate of the sample jet, a fused silica capillary with an outer diameter of 200 µm and an inner diameter of 100 µm (Polymicro Technologies, #1058150021) was inserted into the nebulizers front exit channel. With a nitrogen stagnation pressure of 4.8 bar the resulting analyte flow rate was measured to be 6.5 µL/min for the same solvent conditions as in the further experiments. To conduct reproducible mapping experiments, the nebulizer was mounted on a 2D micrometer stage (Thorlabs). A high-resolution macro image (magnification = 1) of the relative positions of the nebulizer tip and the MS inlet was taken before each measurement in order to correct for minor day to day deviations of the nebulizers start position caused by the translation stage leeway. To ensure a complete unfolding of the protein, it was dissolved in a solution of water/methanol (80/20) containing 0.1 % acetic acid. The used chemicals were Myoglobin (from horse heart min. 90 %), L-Glutathione (>97 %, Fluka BioChemika), Methanol (for HPLC - Gold - ultragradient, Carlo Erba Reagents). To record the ion sensitivity maps the nebulizer was moved a total of 15 steps from its start position with a step size of 100 µm and 7 steps with a width of 250 µm along the x-axis (orthogonal to the inlet) and y-axis (perpendicular to the inlet), respectively. The resulting 112 RAW files were then batch processed to obtain the m/z intensity maps for individual ions, each complete map representing an area of 1.5 mm × 1.6 mm. To improve the visual comprehensibility and to destretch the images, the data sets were mirrored and the pixel widths along the x- and y-axis were ad-

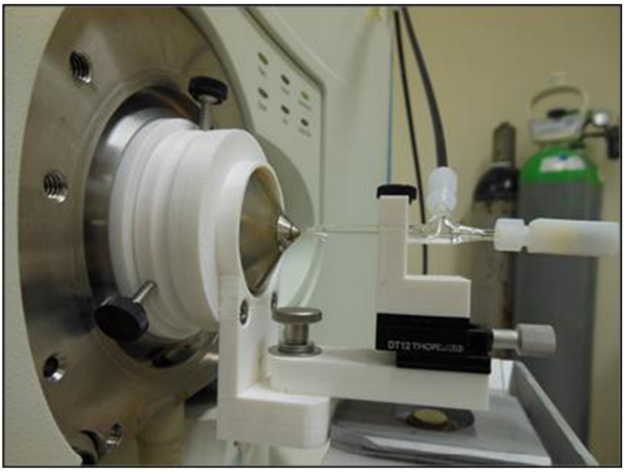

Fig. 4.9: Photographic visualization of the used setup. The x-y translation stage for the controlled displacement of the nebulizer with respect to the MS inlet is not shown. Picture taken from Kanaki *et al.*.[90]

justed to a uniform value of 50 µm using the bicubic interpolation algorithm from ImageJ.[120]

Results

Typical positive and negative mass spectra of myoglobin are depicted in figure 4.11. As can be seen in the mass spectrum of myoglobin, not only the multiply charged proteins but also the detached heme unit could be detected. As stated above, this allows for the recording of ion intensities of different charge states as well as relative ion intensities of different molecules within single measurements.

The intensity maps for the negative as well as positive ions are shown in figure 4.12. These were produced simultaneously using the SSI process and acquired "pseudo" simultaneously by switching the polarity of the ion optics and the ion trap mass analyzer. The

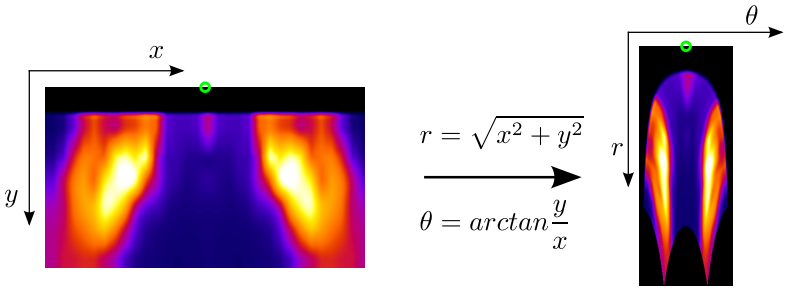

Fig. 4.10: Raw data of the [myoglobin]$^{+14}$ map (left) and the respective mirrored and interpolated result on the right. The gray colors were converted into a lookup table for a better optical perception. Dark colors indicate low values whereas bright colors indicate high values.

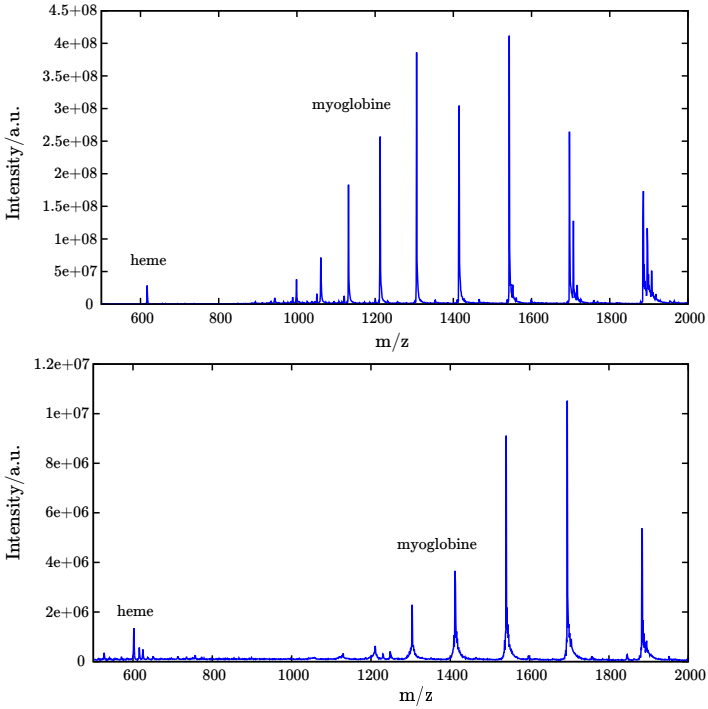

Fig. 4.11: The spatially integrated myoglobin mass spectra in the positive (top) and negative mode (bottom).

images represent the spatial ion intensities in such a way that the tip of the heated ion transfer capillary is always located in the top center position of each image. The black areas in the top of the images represent the space directly in front of the MS inlet. Experiments could only be conducted starting from a necessary minimum distance between the nebulizer and the MS. This results in black areas to which no relative ion intensities could be attributed. Those areas are still represented in the intensity maps to allow for an absolute comparison of the distances between the SSI nozzle and the inlet tip.

A first look at the produced ion acceptance maps reveals strong differences between the spatial distributions of formation likelihood of positive and negative ions. Especially the positive and negative protein ions show a strong dissimilarity in the ion patterns. These differences are the least pronounced for the heme unit, but become more obvious for the low charge state proteins and grow stronger towards increasing charge states.

At a first glance these patterns are somewhat non-intuitive to read but contain all the information of the ion formation/transfer probabilities in the recorded plane. Because of the axial symmetry of the nebulizer plume along the propagation direction of the expanding gas (the center line in the maps in figure 4.12), even the entire 3D information is incorporated in these ion acceptance maps. A closer inspection of an individual ion map reveals this content. As a first example the ion acceptance distribution of the $z = \pm 14$ ion will be discussed. The intensity in the top row represents the ion formation and transfer probability when the SSI is closest to the inlet nozzle. A horizontal view along this x-axial position reveals two individual features with maximal intensity. Please note that the coordinate nomenclature corresponds to the geometry in the laboratory frame as discussed in the experimental section, *i.e.* not the

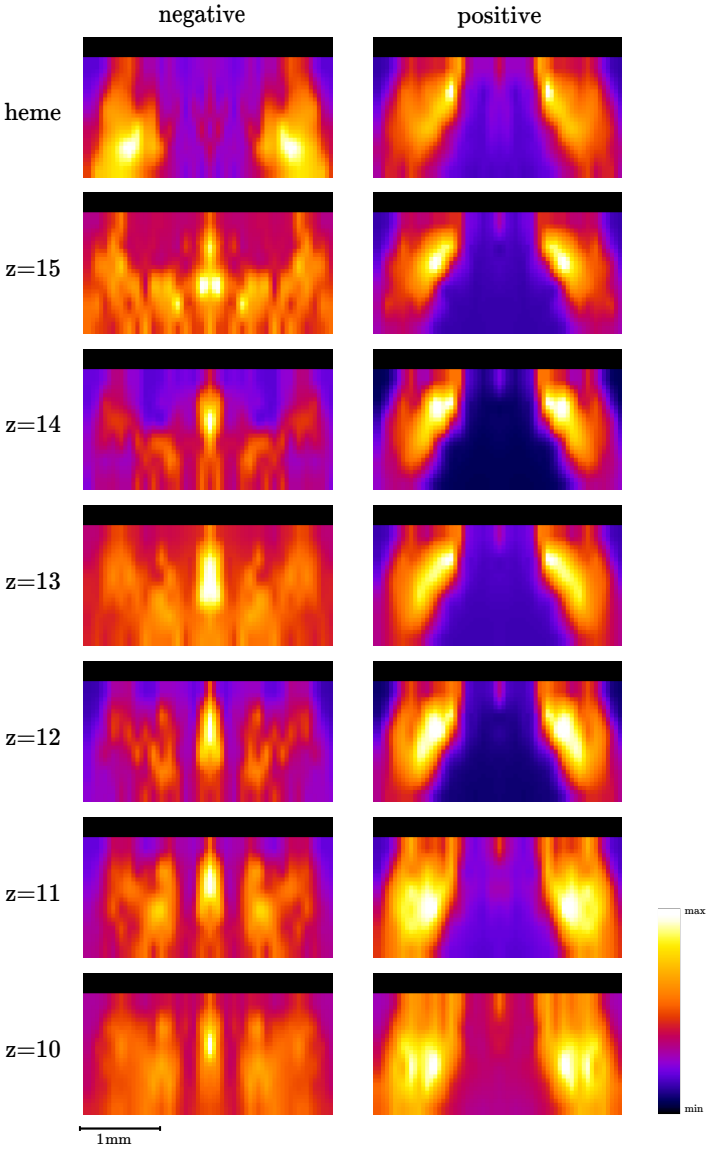

Fig. 4.12: Visualization of the spatial ion acceptance for myoglobin in positive and negative mode. The tip of the transfer capillary is located at the center top of each image. For a better perception all maps are normalized. For relative intensities please refer to figure 4.11.

actual x- and y-axes of the image but vice versa. The local maximum in the center of the image corresponds to the case when the SSI is coaxial to the inlet. The more pronounced outer maxima correspond to geometries, in which the SSI is offset by roughly 0.5 mm in either direction. When increasing the coaxial distance between the SSI source and the orifice (a walk towards the bottom rows in the image), the central maximum decreases in intensity, while the outer maxima increase *via* a global maximum in intensity to decrease again towards even larger distances. During this increase in distance, the perpendicular position of the outer maxima can also be observed to linearly shift towards larger offsets. This linear shift of off-axis displacement from the center towards a larger distance between the nebulizer and the inlet represents a fixed opening angle of the expanding plume. Therefore, the positive ion formation/desolvation is most effective at a certain angle, which correlates qualitatively with the opening angle of the spray cone. A second formation channel can be observed coaxially, which plays only a minor role in this positive ion formation. While all the positive ions show a similar spatial distribution as the discussed case and are mainly formed in the outer perimeter of the spray cone with only a small maximum in the center, the negative ion formation can be seen to exhibit a more complex behavior. They feature a coaxial maximum as well, which is much more pronounced than for positive ion formation. Additionally, local maxima with a distinctive orthogonal offset can be observed. The outer ionization paths towards larger opening angles of the spray, however, show a large anisotropy and seem to be composed of more than one straightforward ion formation channel. The diffuse character of this outer feature hampers a direct visual identification of significant trends in the change of the ion path morphology.

The heme unit shows a different behavior caused by its different molecular properties. The negative ions again appear in the outer regions of the cone similar to the positively charged peptides. In contrast, the negative heme ions also appear in the outer regions but with a larger offset as well as preferentially at a larger distance from the inlet. Besides those described differences between positive and negative ions, there are also trends observable in individual ion yield distributions within the series of multiply charged ions. In positive mode for instance, the maximum of ion occurrence shifts towards larger distances with decreasing charge. This trend goes along with an overall broadening of the angular distribution as well as a shift towards smaller angles. In negative mode, the trend regarding the distance to the inlet is reversed but also less pronounced. The maxima appear to get closer to the inlet with decreasing charge. Also the relative intensities of the outer maxima increase and shift to wider angles.

An exact quantitative analysis of the shown ion formation probability distributions is complicated because of the way in which the maps are presented. The presented dimensions are merely the Cartesian coordinates of the laboratory frame in which the translation stages were aligned while the experiments were conducted and do not correspond to physically meaningful dimensions in the charged particles coordinate system. Physically, the distance from the inlet (*i.e.* the absolute value of the radius centering at the inlet position) and the relative angular fraction of the solid opening angle of the spray cone (*i.e.* the angle between the line spun between the point of interest and the inlet and the axial line in the center of each image) are the two dimensions in which more or less favored ion trajectories should be observed. The radius corresponds to the real distance the formed ions travel in order to reach the inlet, the angle affects the expansion conditions and the density of the surrounding ambient

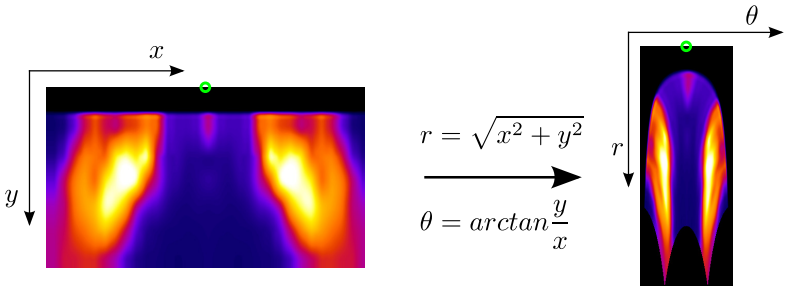

Fig. 4.13: Example polar transform process. The green circle represents the position and diameter of the transfer capillary.

gas (amount of collisions on the way to the inlet). To get a more systematic view of those trends regarding these two dimensions of interest, the ion maps were polar transformed (figure 4.13). From the resulting maps the radial as well as the angular distribution of the ion occurrence can be directly obtained by the line integrals. The results are shown in figure 4.13 for the progression of the $z = \pm 14$ myoglobin ions. In polar coordinates, the two earlier discussed ion formations and transfer channels occur at different angles and can thus still be separated into two distinct regions of interest (ROI) in the following analysis. In case of the positively charged ion formation, these ROIs are defined to be 0-24°for the inner channel (in the remainder of this chapter referred to as channel I) and 24-60°for the outer channel (channel II in this chapter's nomenclature). It is also obvious that both channels have a pronounced anisotropic radial distribution. The summation of the individual ROIs was performed along the line integrals of the coordinate of interest (radius or polar angle, respectively) to achieve quantitative angular and radial distributions. The exact workflow is schematically depicted in figure 4.14.

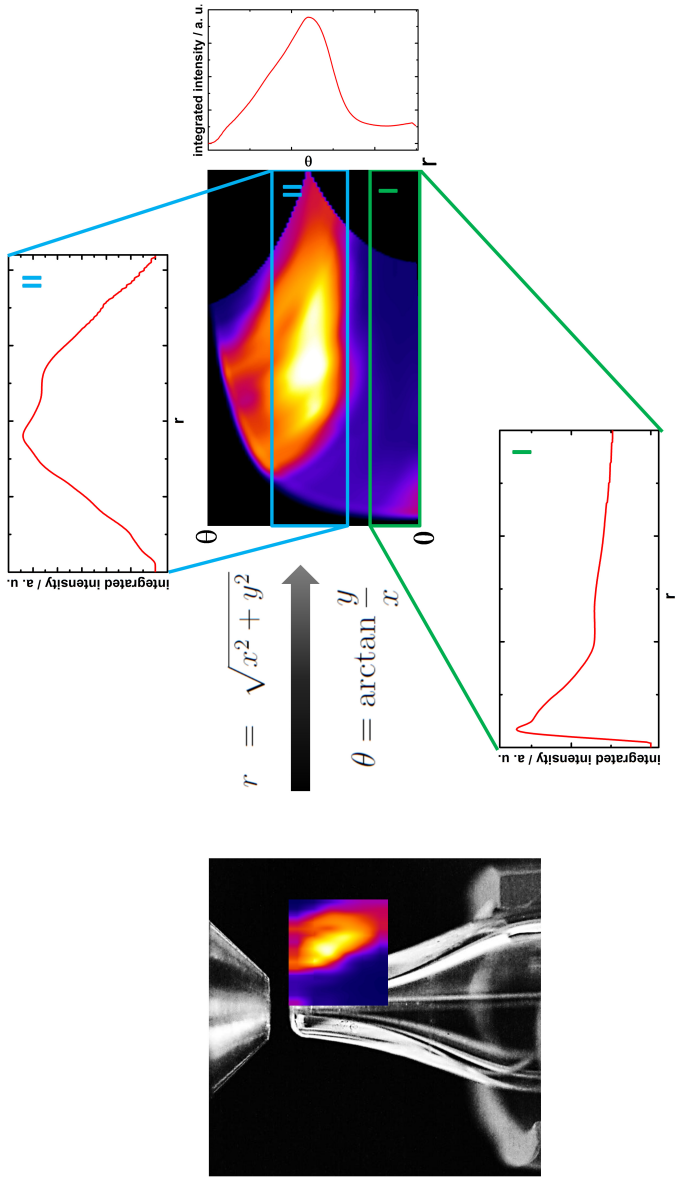

Fig. 4.14: Workflow of extraction of angular and radial distributions of the individual ion formation channels.

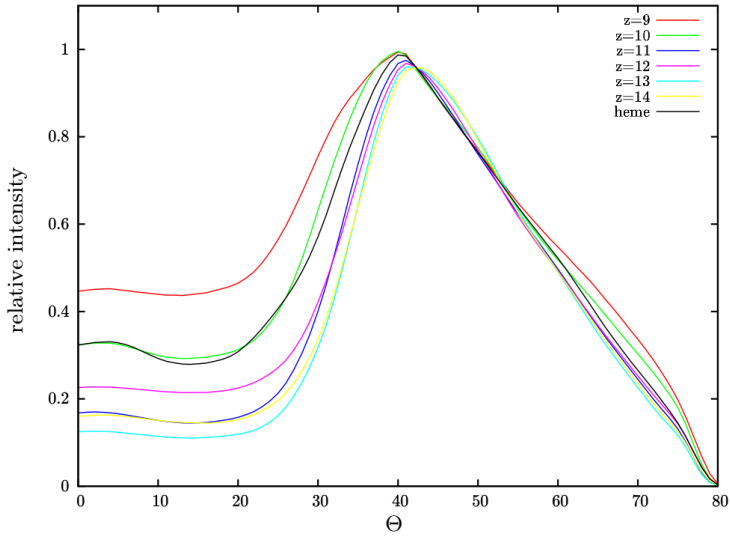

Fig. 4.15: Angular distribution of the positively charged ion formation channels.

Positive ion formation

After extracting all relevant distributions in a first step, the two ion formation channels yielding positively charged ions will be discussed. Therefore, first the angular distributions integrated over all radii will be analyzed. A direct comparison of the different charge states is shown in figure 4.15. For a better visualization, all curves have been normalized to unity at the maximum intensity within channel II. For a comparison of the absolute ionization probability, please refer to the spatially independent mass spectra shown in figure 4.11 or to tables 4.1 and 4.2. As can be seen, the relative ratio of channel I (ions at small angles) and channel II (ions at large angles) strongly correlates with the observed charge state. Even though there is not a monotone linear decrease, it is clearly visible that channel II is strongly favored towards higher charge states in the positive

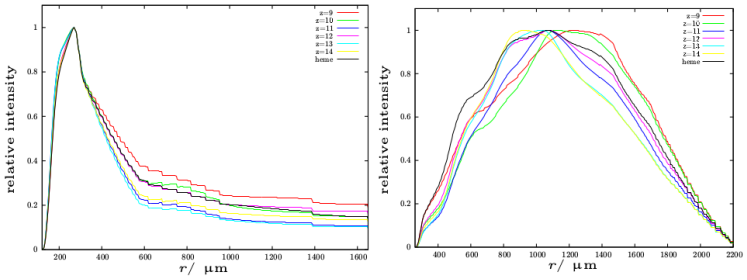

Fig. 4.16: Normalized radial distributions of the positively charged ions formed *via* channel I (left) and channel II (right).

myoglobin. A closer look at the absolute peak positions of channel II also shows a change in the preferred angle for the individual charge states. When looking more detailed into the radial distributions, the channels have to be discussed separately. Figure 4.16 shows the radial distributions of the positively charged ions formed via channel I and II, normalized to unity.

All radial ion distributions in channel I peak at the same distance in direct vicinity of the inlet tube. Again, it has to be mentioned that the radial positions located closer to the inlet could not be determined due to sterical hindrance in the experimental setup geometry. All charge states seem to roughly follow the same bimodal pattern. A pronounced peak and a tailing towards longer distances between the SSI nozzle and the MS orifice can be observed. The tailing is found to strongly depend on the observed charge state, it has a high overall contribution to the ion yield at low charge states and becomes less important towards higher charge states. However, this trend could be very well artificially introduced by the normalization since the global maximum of the ion formation appears to be in the cutout region below $r = 250$ µm in all cases.

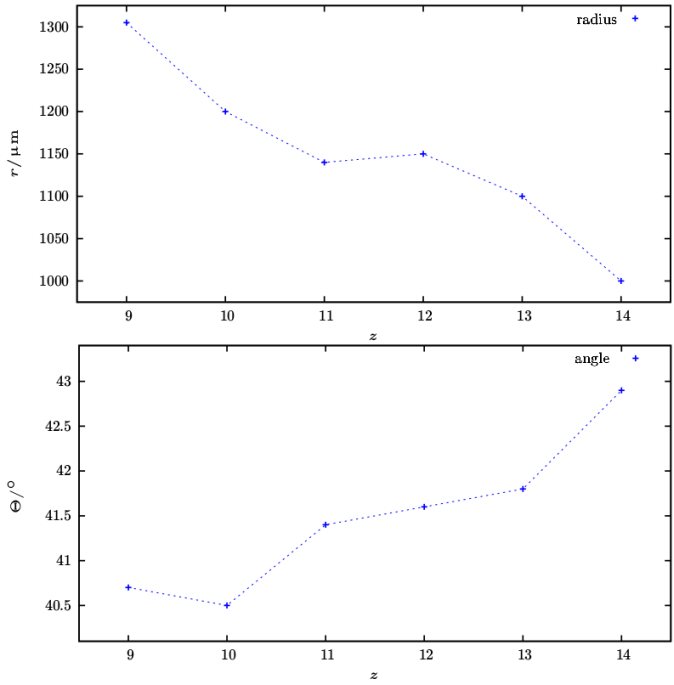

Fig. 4.17: Radial (top) and angular (bottom) trends in the maxima of ion occurrence of the positively charged myoglobin ions.

The radial distribution of the second ion channel is shown in figure 4.16. Again, a clear trend of the radial maximal position can be observed among the charge states. Higher charged molecules are preferentially formed closer to the inlet. It is worth noting that the absolute change in distance between the radial maximum of positively charged myoglobin $z = 9$ and $z = 14$ is 100 pixel, corresponding to 0.5 mm. This clearly shows that the ion formation probability is drastically affected by a change in the spray/inlet geometry. Figure 4.17 summarizes the distinct trends observed in both, the radial and the angular position of the global maximum of ion formation at different charge states.

Negative ion formation

As demonstrated before the absolute net charge of positive ions strongly influences their trajectories while drifting towards the inlet nozzle. The physical driving forces determining these trajectories are coulomb interactions between the charged droplets and the applied potential on the inlet skimmer and the fluid-dynamic transport properties within the expanding jet and the suction towards the vacuum behind the entrance orifice of the MS. Thus, the observed dependence on the charge can be rationalized by two effects. (i) The increase in coulomb interaction caused by the increase in charge causes the deviations. (ii) The different charge goes along with a different collisional cross section *i.e.* diameter of the charged droplets. For a further distinction between these two contributions, a detailed investigation of the ion formation probabilities of the negatively charged ions will be done.

A polar plot of the ion formation probability map for $[\text{myoglobin}]^{n-}$ with $n = 10 - 15$ is depicted in figure 4.18. Several distinct differences from the positive ion maps are revealed in this representation. The relative contribution of an ion formation via channel I (along $\Theta = 0$) has largely increased compared to the positive ions. The polar distribution of negative ions in the outer perimeter (towards higher Θ) shows two pronounced maxima separated by a local minimum in ion intensity. The shape of the outer channels is more bend towards smaller distances from the inlet. This "bending" corresponds to a nonlinearity along a single angle. This stands in stark contrast to the conical shape of the spray plumes found in the fluorescence experiments in the beginning of this chapter. Since all negative ion maps were recorded using the same MS voltages as for the positive ones (however, with opposite polarities), a mere electrostatic coulomb interaction (that would result in an identical spatial

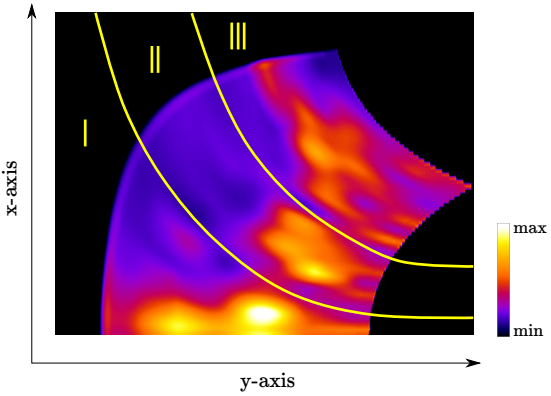

Fig. 4.18: Typical ion formation probability plot for negatively charged myoglobin ions. The yellow lines separate the individual regions of interest and are referred to as channel I, II, and III throughout the remainder of this text.

distribution of the ionization probabilities, accordingly) cannot account for these observed differences. As can be seen in figure 4.18, mere line integrals cannot deconvolute the individual channels since the contributions of ion intensity from the three individual channels overlap in radius and angle. Therefore, a 2D separation into ROIs was performed. The borders between the corresponding regions are depicted in figure 4.18 as yellow lines. After deconstructing the polar plots into these three regions, the resulting radial and angular distributions of the individual channels for the charge state series were extracted. Like in the case of positive ion formation, all ions formed by channel I peak in a narrow angular distribution, centered around the coaxial position $\Theta = 0$. The FWHM of the angular distribution of the heme anions is FWHM $\sim 35°$. All myoglobin anions have a narrower distribution with FWHM $\sim 25°$, independent of their charge state. Channel II also results in a monomodal distribution with a maximum for all formed ions at $\Theta = 26°$. The distributions exhibit a pronounced symmetry and towards larger an-

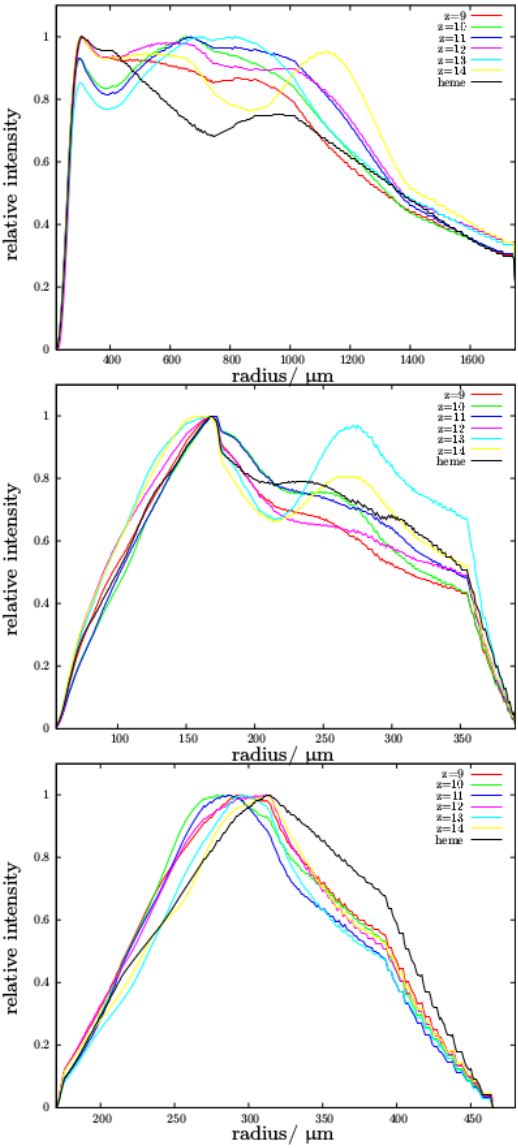

Fig. 4.19: Radial ion distribution of [myoglobin]$^{-n}$ and heme formed *via* channel I (top) channel II (middle) and channel III (bottom).

gles the distributions show a longer tailing. Channel III results in a broad featureless distribution ranging from $\Theta = 25°$to $\Theta = 80°$. The position of the maxima varies between 40° and 50°. Some distributions reveal bimodal character, however, no clear trend for the myoglobin anions can be found. The heme unit once again shows a somewhat different ionization behavior. The heme ions show a well-defined maximum at $\Theta = 40°$ and a much lower intensity towards higher angles compared to their myoglobin counterparts.

Similar to the angular distributions and unlike for the positive ions, no distinct differences in the radial plots of the anions formed out of myoglobin can be observed in figure 4.20. All three channels exhibit a broad featureless shape. Channel I has a less pronounced, albeit visible trend towards small distances to the inlet. Channel II results in a broad Gaussian shaped distribution peaking around 1.5 mm. The anions formed via channel III have a more complex behavior, in most cases a clear bimodal shape with a pronounced node between the individual maxima is found. However, no clear correlation between charge state and bimodality can be observed.

Discussion of the ion formation mechanisms

One distinction between the different mechanisms that underlay positive and negative ion formation is the fact that negative ions are primarily produced/transferred via channel I, whereas this channel only plays a minor role in the detection of positive ions. This can be visualized by superimposing the two polarities of a given charge number in false color representation into one ion yield map. This representation can be seen in figure 4.21. As mentioned above, the two physical driving forces that imprint the ion paths are electrostatic interactions and aerodynamic gas flow. The exact extent of the influence of both forces on the accelerated droplets strongly de-

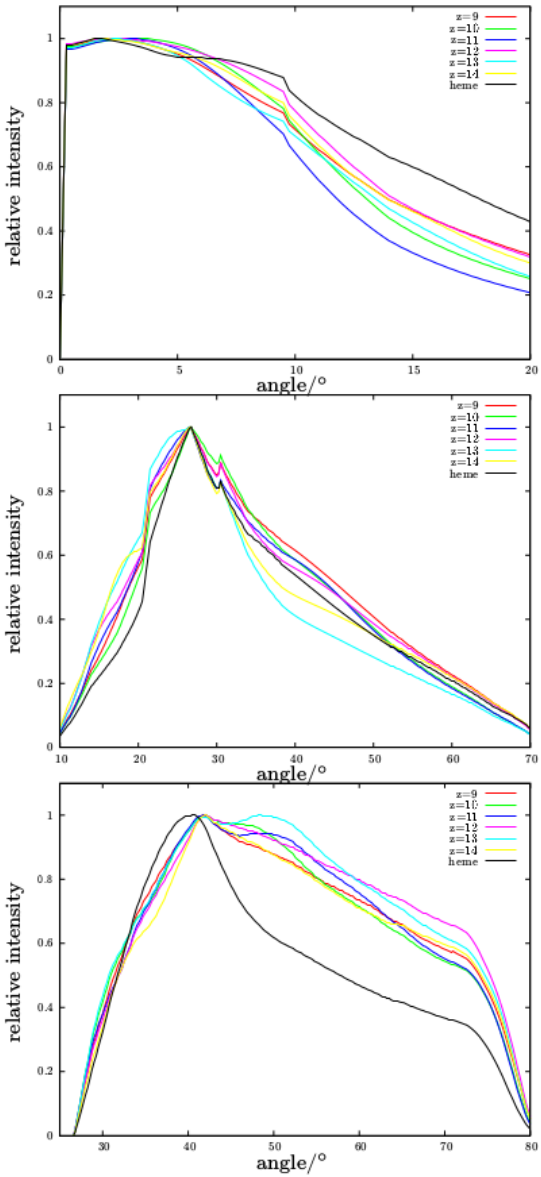

Fig. 4.20: Angular ion distribution of [myoglobin]$^{-n}$ and heme formed *via* channel I (top) channel II (middle) and channel III (bottom).

Table 4.1: Angular, radial and relative intensity values for the positive myoglobin ions.

Charge state	Channel	Radial max / µm	Angular max / degrees	Ratio channel:TIC
9	I	365	5	0.017
	II	1320	41	0.074
10	I	365	4	0.011
	II	1220	41	0.063
11	I	365	3	0.021
	II	1165	42	0.185
12	I	365	3	0.025
	II	1170	42	0.169
13	I	365	3	0.015
	II	1120	43	0.171
14	I	365	4	0.014
	II	1050	44	0.125
15	I	365	3	0.008
	II	1140	44	0.085
heme	I	365	5	0.003
	II	1165	42	0.014

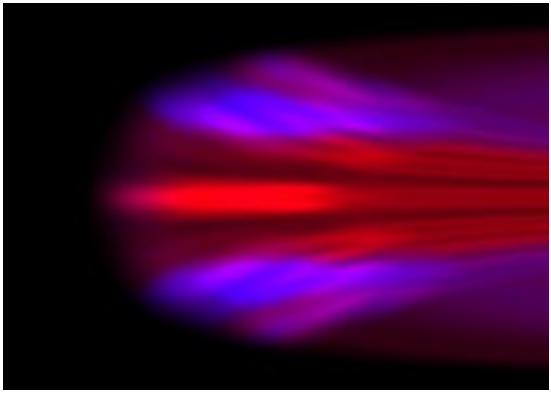

Fig. 4.21: False color representation of negative (red) and positive ions (blue) in the same polar plot.

Table 4.2: Angular, radial and relative intensity values for the negative myoglobin ions.

Charge state	Channel	Radial max / μm	Angular max / degrees	Ratio channel:TIC
9	I	490	89.4	0.060
	II	745	83.3	0.086
	III	1470	79.6	0.072
10	I	655	89.2	0.082
	II	760	83.3	0.110
	III	1415	79.5	0.085
11	I	670	89.3	0.069
	II	760	83.4	0.081
	III	1440	79.6	0.062
12	I	620	89.4	0.051
	II	760	83.4	0.061
	III	1710	79.5	0.052
13	I	815	89.4	0.023
	II	1190	83.4	0.023
	III	1480	79.5	0.022
14	I	1115	89.6	0.008
	II	1150	83.4	0.010
	III	1565	79.5	0.009
heme	I	945	89.6	0.006
	II	925	83.3	0.011
	III	1560	79.9	0.016

pends on their size. In both cases, the size (and its corresponding mass) determine the moment of inertia that makes heavier (larger in diameter) droplets less conceptive to external forces. In the case of any aerodynamic displacement caused by a) the suction into the inlet, b) the Venturi forces of the expanding gas or c) deceleration/deflection induced by surrounding ambient molecules (mostly N_2), the droplet size also determines the collisional cross section. The electrostatic interaction between charged droplets and an external electric field is given by the Coulomb potential. The resulting acceleration/deceleration is given by

$$m\ddot{x} = qE_x \tag{4.3}$$

with m being the mass of the particle, x the acceleration along x, q the charge and E the electric field strength. While m again works as the particles moment of inertia, the interaction is linearly scaled with the charge number q.

The radial and angular distributions of the positive ion formation can be readily explained by a coulomb interaction. To prevent neutralization of the formed ions during wall collisions, the inlet cone is set to a potential with the same polarity as the ions during all experiments. Consequently, the inlet cone is set to a positive voltage in positive ion mode. Particles of the same momentum (same m and same acceleration from the venture expansion in the spray nozzle) but with a growing net charge q experience an increased repulsion from the inlet. Thus, with increasing charge number the ions are preferentially formed closer to the nozzle. Ions formed at larger distances do not have the sufficient momentum to overcome the potential slope. Since the inlet has a conical shape, the ion cone of channel II is repelled towards larger angles with an increasing coulomb repulsion.

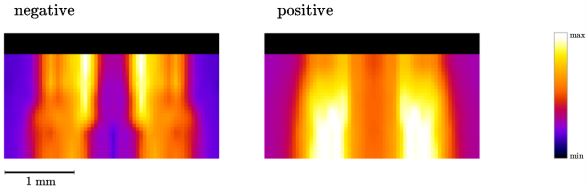

Fig. 4.22: Visualization of the spatial ion acceptance for glutathione in positive and negative mode.

The differences between positive and negative ion formation mechanisms become larger with an increase in net charge. For the singly charged heme unit, the ion formation probabilities are almost equally distributed. The dissimilarities between negatively and positively charged proteins increase with increasing q. Since the electrostatic potential interacting with the positive and negative ions is identical (the voltage applied to the inlet has the same value but opposite sign), this difference in electrostatic response of the particles distribution has to stem from different masses. For a better understanding the formation of the charged droplets has to be elucidated.

In order to clarify the correctness of the previously mentioned bag mechanism proclaimed by Zilch *et al.*, the spatial dependence of ion formation of the small peptide glutathione was also studied. Unlike the large myoglobin, this oligopeptide has a smaller mass and appears only singly charged. A comparison between the results and the anisotropy of the ion yield of the previously studied heme unit should therefore prove that the similarity in the case of heme was caused by its low charge density rather than because of its chemical difference.

The comparison of the ion yield maps obtained for glutathione shows some similarities but each also contains some distinct features of its own. Generally, the intensity distributions in the glutathione maps follow the same trends as those of the peptide ions. The

maxima for the positive ions appear farther away from the capillary tip while the negative ions occur much closer and with less offset.

The occurrence of spatially separated ionization channels might also be an indicator for the coexistence of CRM and IEM which originate from different droplet sizes. On the other hand glutathione lacks these distinct patterns which follows the commonly accepted explanation that small molecules mainly ionize *via* IEM or that the ionization process takes place when the droplet has already shrunk to sizes (usually the size of a few nanometers) where the distinction between CRM and IEM gets unspecific.[121;122] Nonetheless, there is only one consistent explanation for all the observed trends. This model is based on the bag mechanism and the two ion formation models described in the introduction of chapter 4. Based on the statements made there, IEM mainly yields in singly charged ions. The results allow an unprecedented insight into the complex reaction dynamics involved in ion formation that might help to shed some light onto the underlying transitions. In contrast to all previously published results, the results introduced here allow for a separation of ion channels that would usually be superimposed. Especially from the results observed for myoglobin it is apparent that the spatially resolved detection of ions allows a clear attribution of ions to different formation pathways. In combination with this spatial distinction of individual mechanisms according to this understanding, the results shown here strongly point towards a concluding model which will be briefly described in the next paragraph.

Central droplets are small and depleted of positive ions. These small droplets may never develop high enough charge density to release ions via ion evaporation, which is the main mechanism for small ion generation (singly charged). Thus, very little negatively charged heme ions are observed *via* the central channel. However, since central channel droplets do contain negative ions of the pro-

tein they are introduced into the gas phase via the charge residue mechanism. That is why only negative protein ions are visible along the central channel.

The larger droplets in the outer channel (which are enriched in positive ions, but also contain considerable amounts of negative ions) increase their charge density sufficiently as they shrink to release ions *via* the ion evaporation model. Thus, small singly charged ions can be observed here with both, positive and negative charge states. Finally, the remaining positive and negative protein ions will be observed *via* the charge residue model. To summarize, the central channel gives ions *via* the charge residue mechanism (negative protein ions). The outer channel releases ions *via* the ion evaporation mechanism (small ions) and the remaining large ions are formed according to the charge residue model.

Summary and conclusion

In this chapter two inexpensive randomly accessible SSI sources were presented. The sources are readily available and could thus be used in the future to compare instruments directly in different laboratories. Protic analytes ranging from a single amino acid to a small protein were successfully ionized. To elucidate the origin of charged molecules and to characterize the spray formation/ionization in the proposed setup, LIF experiments were conducted. As previously observed for other SSI sources the results reveal the used airbrush to lead to the formation of a fine aerosol.[93;102] For the first time the ion desolvation in an sonic spray induced aerosol cone was observed via solvatochromism LIF experiments. Desolvated ion formation could be shown to occur at an early stage in the expansion zone and preferentially in the outer perimeter of the spray cone. The majority of the ions in the spray cone, however, are still sol-

vated. This indicates that the desolvation mainly takes place in the intermediate pressure inside the AP-MS interface. Symmetry considerations allowed the reconstruction of the 3D spatial distribution of the ejected spray. Single-exposure LIF photography gave access to the droplet-size distribution and the velocity range of the spray.

A closer investigation confirmed the experimentally observed trends where positive ions are formed in the outer regions of the spray cone. However, those trends become more elusive at higher charge states and for negative ions. The negative ions are preferably formed in a reaction channel located in the inner spray cone. Nevertheless, further spatially less confined channels at bigger angles exist. These ionization regions do not coincide with the previously identified desolvation regions. This leads to the conclusion that the negative ion formation is governed by different kinds of droplets which evaporate later in the transfer region of the MS instrument. Unfortunately, the occurrence of those droplets is impossible to proof with imaging techniques since their size is below the optical diffraction limit. The overall mechanism of the spatial ion formation showed to be a complex interplay of coulomb repulsion and aerodynamic properties with an additional external influence of electrical fields and gas flows/suction. It can also be concluded that optimizing settings for a spray ionization process like ESI, SSI but also IR-laser desorption can be only performed for one single analyte, or even more accurate, for a single analyte in a specific charge state. This finding should be considered in all future experiments and is an entirely new concept because in contrast to laser based ionization techniques like MALDI in which a geometry dependence on the analyte of choice is well known [123;124], up to now spray based ion formation methods were always considered to result in isotropic, non-analyte depending ion formation. For a better understanding of this complex ion formation and a better distinction between the pro-

posed concepts of IEM and CRM, additional experiments including the systematic investigation of specific molecular/ion properties like total charge, mass-to-charge ratio, solubility, proton affinities and also instrumental parameters have to be performed. Also, recent developments in computational techniques for the modeling of AP ionization and transfer mechanisms like the combination of fluid dynamics with ion trajectories in electrical fields [125] could contribute towards a better understanding of spray ionization sources like SSI and ESI.

Based on the findings described in this chapter and a thorough consideration of the related literature, a new ion formation model could be introduced that shows a contribution of both, IEM and CRM at different times along droplet evaporation.

Chapter 5

Characterization and application of a low temperature plasma ambient ionization source for probing the droplet environment

In order to also be able to probe the surrounding of levitated droplets, a low temperature plasma source was built. A thorough characterization of this low temperature plasma source is given in this chapter. The source was subsequently used to probe the gaseous surrounding of a droplet. First preliminary results show promising results towards a closed bulk/headspace analytical approach.

Dielectric-barrier discharges

In the preceding chapters, it could be shown that a successful interrogation of the droplets content is possible. The mechanism of the laser-induced desorption/ionization process could mainly be caused by a spray formation. These processes could be satisfactory mimicked by a sonic spray device. Since a levitated droplet is an open system to its gaseous environment, it would be desirable to also be capable of probing its direct vicinity in the gas phase.

Lately, dielectric-barrier discharge (DBD) devices have attracted significant attention from many areas of science. They have been used for plasma cleaning,[126;127] for disinfecting water[128] and surfaces[129] through ozone generation, as light sources,[130;131] and as sources for atomic emission spectroscopy.[132;133] More recently, modified DBDs have been used as ionization sources for molecular mass spectrometry.[43;44] These discharges have also been shown to be capable of directly desorbing and ionizing molecules from surfaces[134] for mass spectrometric analysis without the need for sample preparation, which has become a field of study of its own called ambient desorption/ionization mass spectrometry (ADI-MS).[76] The most commonly used configuration of DBD for ADI-MS analyses, the low-temperature plasma (LTP) probe was, first described by Harper *et al.*.[135]

Much of the interest in these plasmas stems from their simplicity and flexibility. A variety of electrode geometries can be employed[136] and only very low power is required, often less than 1 W. Furthermore, the operation with a variety of gases, including air, at minimal flow rates (*i.e.* low consumption) is possible, thus meeting all requirements for a compact and portable plasma source.[137]

The utility of DBDs as excimer or ozone[138] sources has rapidly expanded, partly due to fundamental studies regarding the plasma

structure and processes, particularly the work by Eliasson *et al.*[139;140] Unfortunately, fundamental studies on these plasmas in the context of analytical applications have lagged behind. This gap in understanding is especially noticeable in the use of these discharges as ionization sources for molecular mass spectrometry. Most studies have focused on optical spectroscopic methods to understand the structure and behavior of DBD ionization sources. Steady-state measurements have revealed some of the excited species created in the discharge as well as the rotational temperature and electron number density, which are important parameters in desorption and ionization processes.[43;141]

Spatially resolved fluorescence[142] and emission[143] from a helium LTP revealed the important roles of metastable helium, He_m, and helium dimer ions, He_2^+ in the formation of N_2^+ and other reagent ions. These reagent ions are responsible for the ionization of gaseous or desorbed analyte species through atmospheric pressure chemical ionization (APCI) mechanisms. The ionization process is initiated by Penning ionization caused by metastable helium species.

$$He_m + M \longrightarrow He + M^{\cdot +} + e^-$$

Under ambient conditions, one can assume that $M = N_2$ which leads to formation of ${N_2}^+$ as a key intermediate which will then react with water to form protonated water clusters.

$$\begin{aligned}
{N_2}^+ + 2\,N_2 &\longrightarrow {N_4}^+ + N_2 \\
{N_4}^+ + H_2O &\longrightarrow H_2O^+ + 2\,N_2 \\
H_2O^+ + H_2O &\longrightarrow H_3O^+ + OH^- \\
H_3O^+ + (n\text{-}1)\,H_2O &\longrightarrow [(H_2O)_n + H]^+
\end{aligned}$$

Depending on the relative proton affinities, analytes can then be ionized via the proton transfer reaction:

$$[(H_2O)_n + H]^+ + A \longrightarrow nH_2O + AH^+$$

In addition to the steady-state measurements, time-resolved optical studies have revealed that these DBDs are not continuous plasmas, but are comprised of transient plasma bursts, called plasma bullets, which propagate through space at supersonic velocities. Thus, the duty cycle of the discharge and, by assumption the reagent ions, is very low, ca. 1 %.[144;145] Unfortunately, relatively high-speed mass spectral studies have yet to be performed on the LTP probe, which would provide the most direct information on the creation of reagent and analyte ions.

In the first part of this chapter, a time-of-flight mass spectrometer (TOF-MS) was used to record reagent and analyte ion signals from a relatively low-frequency LTP probe. The high acquisition rate of the instrument enabled multiple mass spectra to be acquired within the duration of one waveform cycle. Additionally, ion signals from an LTP powered with different voltage-waveform shapes were acquired and related to the discharge current traces to understand the role of the applied voltage in the resulting ion formation.

Experimental

The LTP probe used in these studies was similar in design to that described by Wiley *et al.*[137] A 2.4 mm wide copper ring electrode, to which a high voltage was applied, was placed on the outside of a quartz capillary (1.6 mm o.d., 0.6 mm i.d., Sutter Instruments, Novato, CA). A 0.38 mm diameter stainless steel wire, which served as the grounded counter electrode, was placed inside the quartz capillary. A 3.18 mm Swagelok tee and Teflon ferrules (Swagelok, USA) were used to fix the position of the quartz capillary and the grounded electrode as well as providing the gas inlet for the discharge. Helium gas flows between 300 and 700 mL min^{-1} were

monitored and adjusted using a mass flow meter (Voegtlin Model GCR A95A BA15, Aesch, Switzerland). However, the flow rate did not play any significant role in these studies, in consequence a standard flow rate of 550 mL min^{-1} was used throughout to ensure the stability of the vacuum system. High-voltage waveforms for the LTP were generated using a function generator (Model DS345, Stanford Research Systems, Sunnyvale, CA), which were fed into the input of a high voltage amplifier (Model AS-3B1, hivolt.de, Hamburg, Germany). The amplifier is capable of producing potentials from −3 to 3 kV with frequencies of up to 1.5 kHz. Voltage waveforms from the amplifier, without any load, were observed with a high voltage probe (TT-HV 150, TESTEC, Frankfurt, Germany) connected to a digital oscilloscope (TDS 2024B, Tektronix, Beaverton, OR, USA). Unfortunately, due to loading issues, the voltage could not be measured when the discharge was powered. Current waveforms were recorded by measuring the voltage drop across a 1 kΩ resistor connected between the pin electrode and ground. For the analyses of the droplet's environment, the used frequency and amplitude were adjusted to $f = 120$ kHz and $U = 7$ kV_{pp} using a modulated high voltage generator (PLASMSP_V2, Voltagezone Electronics, Graz, Austria). To avoid disturbances by acoustic streaming caused by the standing wave, the source was set up with an angle of 30° relative to the inlet. Also the droplets were positioned with an offset of 2 mm to ensure the plasma source didn't directly interfere with the liquid bulk phase.

The ions produced by the LTP probe were detected with the previous described TOF-MS. To ensure that the vacuum system could cope with the helium flux (99.999 %, Linde, Düsseldorf, Germany), an additional 500 µm orifice was placed ca. 34 mm in front of the normal 300 µm pinhole inlet. Independent voltages could be applied to both entrance orifices, however, it was observed that the

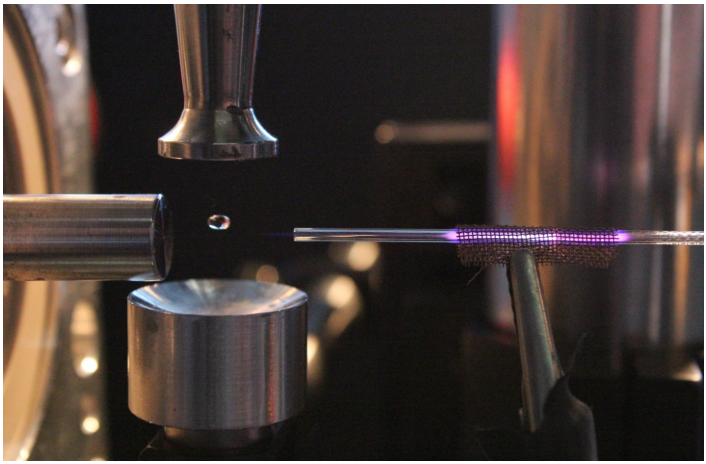

Fig. 5.1: The used LTP setup to probe the droplet's environment.

best signal stability was achieved when both electrodes were floating. It is important to note that there was no qualitative difference in the reagent ions detected or their distribution when the inlets were grounded or had a small potential on them (less than 20 V) as compared to floating the electrodes. The API-HTOF is capable of providing a high mass spectral acquisition rate of up to 40 kHz at the cost of mass range, physical memory, and run time. For a time-resolved interrogation of the fast transient signals generated by the LTP, the TOF-MS was operated with an extraction frequency of 20 kHz with 50 spectra averaged resulting in an acquisition rate of 400 spectra per s (2.5 ms per spectrum). Temporal synchronization between the repeller pulses of the TOF-MS and the function generator was achieved by using a delay generator (Model DG535, Stanford Research Systems, Sunnyvale, CA).

Time-resolved mass spectral characterization of ion formation

The LTP was powered with a high voltage amplifier, which enabled the performance of the source to be examined with different waveform shapes and frequencies. This specific amplifier was capable of producing a 6 kV_{pp} waveform with frequencies up to 500 Hz without degradation in the shape of the waveform. A visually stable DBD could be produced with frequencies between ca. 2 and 500 Hz with four different types of waveforms: sine, triangle, sawtooth, and square waves. An example of the steady-state background, or reagent ion, mass spectrum is shown in figure 5.2 for the LTP operated with a 10 Hz square wave. The ion pattern in this spectrum resembles those previously described for LTP [135] and the flowing atmospheric pressure afterglow (FAPA). [45] These ions include protonated water clusters, $(H_2O)_nH^+$, as well as NO^+, O_2^+, and O_3^+. Protonated water clusters are capable of proton transfer reactions with basic gas-phase analytes, which is the most common ionization pathway in plasma-based ADI-MS. The other reagent ions can undergo charge transfer interactions to form ions from non-polar molecules. [45;42] The reagent ions formed and their relative abundances were found to be independent of gas flow rate, waveform shape, and discharge frequency.

Time-dependent ion signals

DBDs are known to be transient sources consisting of short-lived corona discharges and plasma bullets. [136;145] Thus, to better understand the plasma and ion formation processes, it is crucial to monitor the time-dependent generation of reagent and analyte ions. Therefore, the high repetition rate of the time-of-flight mass spec-

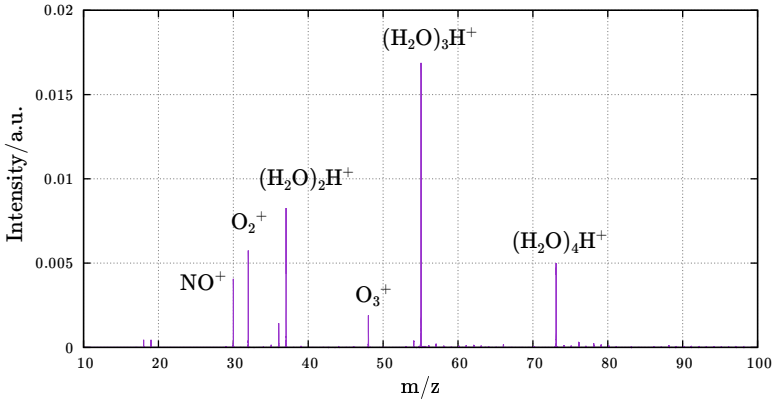

Fig. 5.2: Averaged background mass spectrum of the LTP probe operated with a 6 kV_{pp}, 10 Hz square wave. [146]

trometer was exploited to record real-time mass spectra at a full spectral readout of 400 Hz. Figure 5.3 shows the time-dependent signals for two reagent ions, $(H_2O)_4H^+$ and O_2^+, for the LTP operated with a 6 kV_{pp}, 10 Hz square wave. In this time trace, the pulsed nature of the discharge is apparent. The temporal profile and arrival time of the two reagent ions correlate well, which indicates that any differences that may exist in the relative time or duration of ion formation are lost in the transit time from the discharge to the inlet of the MS, likely from diffusion and collisional processes near or in the atmospheric pressure interface. It was also found that changing the gas flow rate and, as a result the transport velocity, did not significantly alter the broadening, which supports the previous claim. Because of this broadening, it was only possible to baseline-resolve the ion pulses with discharge frequencies less than ca. 50 Hz, depending on the waveform. While this degree of broadening spanning over several orders of magnitude might be surprising, it has been recently demonstrated that significant temporal ion-packet broadening occurs with capillary-based atmospheric pressure interfaces

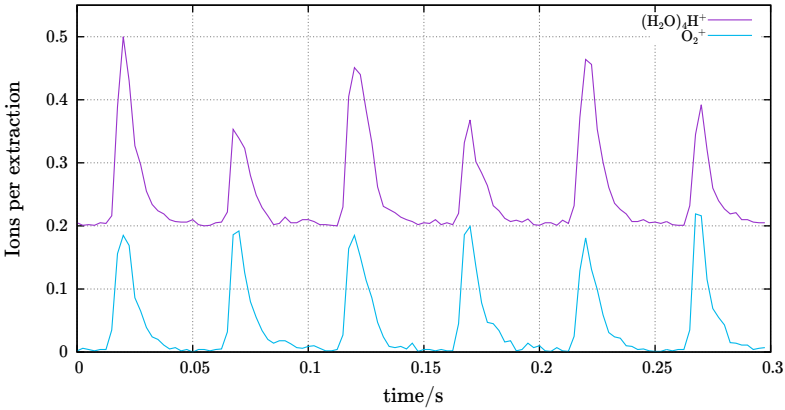

Fig. 5.3: Chronogram of the reagent ion signals, $(H_2O)_4H^+$ at m/z 73 (purple trace) and O_2^+ at m/z 32 (teal trace), for a square wave LTP probe operating at 10 Hz. Note that the purple trace is vertically offset for visualization purposes. [146]

(API).[147] In that study, pulsed laser ionization produced spatially and temporally narrow ion packets near the inlet, similar to those from the LTP source, which were broadened to widths of at least 100 ms. Ion trajectory and fluid dynamics modeling showed similar broadening caused by turbulent flow patterns near and within the transfer capillary.[147] In the present case, a capillary inlet was used for two reasons: to imitate the capillary API used in many LTP studies and to reduce the helium flux into the instrument. It has been demonstrated that single particle inductively coupled plasma MS (ICP-MS) can produce ion pulses of less than 200 µs due to the two cone (*i.e.* sampler-skimmer) inlet geometry, which mostly preserves the laminar flow pattern in the central channel of the ICP.[148;149] Future efforts will be focused on investigating the role of inlet geometry on ion packet broadening and diffusion. Similar transient ion signals were obtained for a variety of voltage waveforms, frequencies, and duty cycles. Figure 5.4 displays the chronogram of m/z 55, corresponding to $(H_2O)_3H^+$, for two cycles of different

voltage waveforms, as well as the measured discharge current. It was not possible to measure the discharge voltage waveform during analysis without loading the amplifier and altering the discharge, as such: The voltage traces shown in figure 5.4, the dashed teal lines, are presented for visualization purposes only. In addition, to maximize the temporal resolution of the current measurements, only one cycle was acquired at a time, so the current traces were duplicated for visualization purposes as shown in figure 5.4.

All four waveforms, sine, triangle, sawtooth, and square waves produced stable discharges with very reproducible pulses of ions. However, each type of waveform produced a distinctly different pattern of transient ion signals, which correlate with the measured current waveforms. A sine wave-powered LTP produced a temporally broad packet of ions (figure 5.4a). Examining the discharge current reveals that each half cycle produces multiple, short-lived (*e.g.* significantly less than 40 μs) discharges. These short pulses were also very erratic in time and current, which is an indicator of a filamentary mode of operation that arises from transient micro corona discharges.[150] While the excited species and ions created in these brief plasmas are assumed to be initially localized in time and space, they broaden through collisions in turbulent flow and mix with ion clouds from other micro discharges prior to extraction into the low pressure mass analyzer resulting in a broadened temporal distribution of ions as described in detail above. Similar to the sine wave, the triangle wave LTP consisted of many short, sporadic plasma pulses, as seen in the current time trace (figure 5.4b). However, the current spikes were less frequent and had a more pronounced separation between the pulses in the positive and negative half cycles of the waveform. The temporal spacing of the micro discharges was large enough that the ion clouds created in the two half cycles did not overlap appreciably and two distinct ion pulses were detected

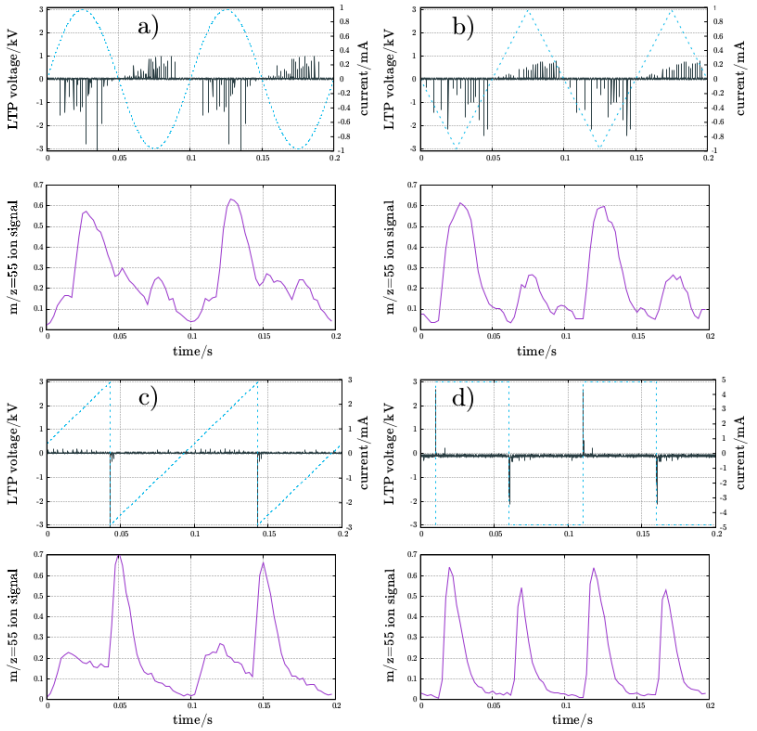

Fig. 5.4: Selected ion chronograms and current waveforms for an LTP powered with 10 Hz, 6 kV$_{pp}$ (a) sine, (b) triangle, (c) sawtooth and (d) square waves. The voltage waveform traces (dashed, teal lines) were not recorded with the discharge on and are for visualization purposes only. Note that the current trace for one cycle was recorded to maximize temporal resolution; as a result the displayed current traces have been duplicated for the second cycle for visualization purposes.[146]

per voltage cycle. Both the sine and triangle waves produced current pulses in the positive half cycle that were significantly smaller than those observed when a negative voltage was applied to the ring electrode. Consequently, less excited species and reagent ions were produced in the positive lobe of the voltage waveform, which can be observed in the time-resolved mass spectra (figure 5.4a and b). These transient current spikes observed with sine and triangle wave LTP were even found to occur when relatively little potential exists between the two electrodes (*i.e.* near the zero crossing). The dielectric-barrier discharge utilized by the LTP is a type of capacitively coupled plasma, which behaves similar to a capacitor in a way that the current through the system is governed by the derivative of the applied potential, in the form of electrical breakdown. The occurrence of current spikes while the applied voltage was near zero indicates that the time-dependent voltage change (*i.e.* $\mathrm{d}V/\mathrm{d}t$) is sufficient to induce a capacitively coupled plasma.

LTP powered with a sawtooth waveform (figure 5.4c) exhibited the irregular current pulses during the slow voltage ramp, similar to the sine and triangle waves. However, the rapid decrease in voltage at the end of the cycle, from +3 kV to −3 kV, resulted in a strong and reproducible negative current pulse of ca. −3 mA. Thus, the sawtooth LTP can be viewed as operating in a filamentary mode for most of the cycle. But, with the rapid change in voltage, a homogeneous discharge is formed.[150] This discharge behavior was reflected in the reagent ion profile. Early in the cycle, when the applied voltage was negative, few micro discharges occurred and thus little ion signal was observed. As the discharge voltage became increasingly positive, a greater number of erratic current pulses resulted in a temporally broad packet of ions. In contrast, the homogenous, yet short-lived, plasma formed from the sharp decrease in voltage translated to a relatively compact, dense cloud of reagent ions. Thus, the

sawtooth wave LTP appears to operate like a combination of the triangle wave and square wave LTP. A reproducible and controlled mixed-mode discharge, such as this one, could have significant analytical utility. As recently noted,[136] the homogenous mode of a DBD typically leads to a more soft ionization, where little or no fragmentation of the analyte takes place. However when the discharge is operated in a filamentary mode, more fragment ions are detected.

Finally, the square wave LTP produces two homogenous plasma pulses every cycle: one at each transition between positive and negative voltages. This observation is feasible because DBDs are inherently capacitively coupled plasmas. As such, the system behaves as a high-pass filter that will only allow current flow with a change in the input voltage with fast voltage changes (*i.e.* high frequencies) leading to larger discharge current/power. To check if a zero crossing is crucial for a discharge the voltage waveforms were adjusted to alternate between 0 and 3 kV (*i.e.* a pulsating DC mode). Only one ion peak per cycle was produced for the square and sawtooth wave LTP (figure 5.5); in both cases the signal occurred at the rising voltage slopes. Because the voltage of a square wave is constant, other than the transitions between voltage levels, no micro discharges or ions were produced during the constant voltage period. The plasma pulses were short and well defined, lasting approximately for 40 µs. These consistent current pulses are likely manifested as plasma bullets, which are high velocity ionization waves known to occur with DBDs. After collisional and diffusional effects, the ion cloud expanded significantly, as seen in the mass spectral signal (figure 5.4d) where the duration of ion pulses was 10.5 ms at FWHM. This temporal broadening of detected ions, caused by the spatial broadening of the ion packet as indicated earlier, agrees with simulations of ion

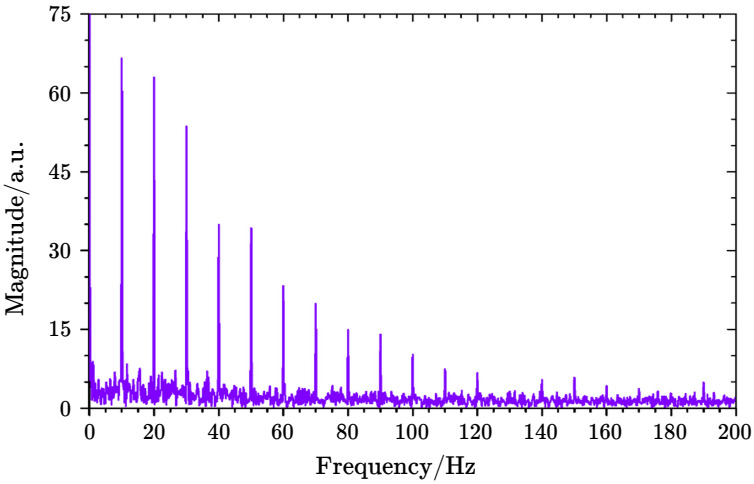

Fig. 5.5: Frequency spectrum of $(H_2O)_3H^+$ ion signal from a 10 Hz square wave from 0 kV to 3 kV. The base peak at 10 Hz indicates that only one plasma pulse occurs per cycle. In contrast, a square wave from −3 kV to +3 kV produced two pulses per cycle. [146]

transport from an atmospheric pressure ion source into a reduced pressure mass analyzer.[147;151;152]

Fourier analysis of ion signals

In addition to the temporal profile of the pulsed ion signals, Fourier analysis of the periodic signals also provides valuable insight into the structure of the discharge as well as ion formation processes. Fast Fourier transforms (FFTs) of the transient signals for m/z 55 state molecule for the four voltage waveforms at 10 Hz are shown in figure 5.6. For all tested frequencies, the sine wave LTP yielded the simplest reagent ion Fourier spectrum with the most abundant frequency component at the fundamental drive frequency of 10 Hz as shown in figure 5.6. The minor contributions at overtone frequencies are a result of the non-sinusoidal curvature of the ion-signal traces.

The Fourier spectra became more complex for the ion signals produced by the other waveforms, which is congruous to the frequency spectra of the voltage waveform itself. The FFT of the triangle wave LTP was most similar to the sine wave FFT, while the signals from the square wave contained significant contributions from higher order even harmonics. In addition, the second harmonic frequency of 20 Hz was the dominant contributor in the case of the triangle and square wave LTP signals, which is a result of plasma events occurring both in the positive and negative half cycle (figure 5.6). Thus, the Fourier spectra of these ion signals can provide information about the temporal and spatial structure of the ions produced, which was found to be directly related to the mode of the DBD: homogenous or filamentary. The Fourier analyses from these data were also found to be useful in identifying subtle differences in ion formation processes within one cycle. In most cases, the frequency spectra for different reagent ions for a given discharge voltage and frequency were nearly identical. However, a clear difference exists between the Fourier spectra of charge transfer ions (*e.g.* O_2^+ and NO^+) and proton transfer species (*e.g.*, $(H_2O)_nH^+$) generated by the square wave LTP (figure 5.7). Frequency spectra for the ion signal from each protonated water cluster contained odd harmonics, which were absent from those corresponding to O_2^+ and NO^+. The odd harmonics would only be absent if the ion time profiles from the two plasma events in one cycle were nearly identical. The chronogram for O_2^+ (blue trace) shown in figure 5.4 exhibits this behavior, which indicates that the relative amount of this charge transfer species was the same from the plasma bullet on the rising edge as that on the falling edge of the waveform. In contrast, the amount of $(H_2O)_4H^+$ (purple trace in figure 5.3) was significantly less from the plasma formed during the falling edge of the waveform. This finding signifies a difference in the ion formation processes of

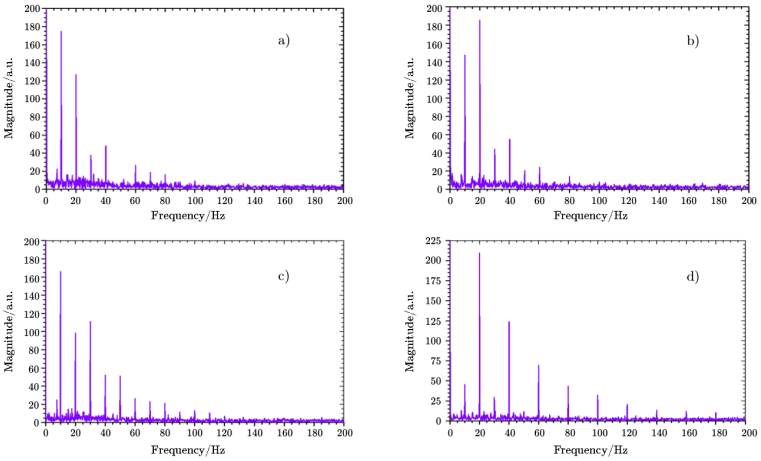

Fig. 5.6: Fourier spectra of $(H_2O)_3H^+$ ion signal for an LTP powered with a sine a), triangle b), sawtooth c) and square wave d). Note that other reagent ions produced similar frequency spectra for each waveform. [146]

the two species within one cycle. While the cause of these differences is not known at this time, the ability to produce different reagent ions at different times would result in temporally controlled, selective ionization *via* an APCI or a Penning ionization channel. Data obtained in ADI-MS analyses would gain much dimensionality due to this added complementary information, expanding the capabilities of the field as a whole.[153]

Steady-state reagent ion production

While the measurement of time-resolved ion signals provided insight into the underlying mechanisms of plasma formation, the steady-state signals yielded information on the analytical capabilities of the discharge. Figure 5.8 shows the signal for m/z 55, which corresponds to the $n = 3$ protonated water cluster, for the LTP powered

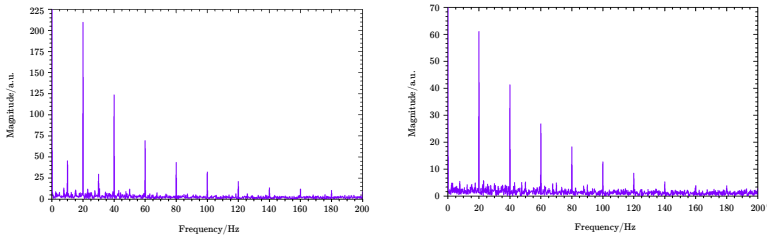

Fig. 5.7: Frequency spectra for (a) $(H_2O)_3H^+$ and (b) O_2^+ signals for a 10 Hz square wave LTP. Note the appearance of odd harmonic peaks (*e.g.* 10, 30. 50 Hz) in (a) that do not appear in (b).[146]

with varying waveforms and frequencies. It must be noted that all other reagent ions exhibited the same trends (not shown here). In general, a higher density of reagent ions results in a broader dynamic range of analysis as well as reduced matrix effects.[154] An increase in the discharge frequency, from 5 Hz to 20 Hz, resulted in a greater production of reagent ions caused by an increase of the number of plasma events per mass spectral integration window. It is expected that a linear increase in ion signal with increasing frequency should occur until there is temporal overlap between homogeneous plasma events or plasma bullets. In the case of triangle, sine, and sawtooth waves, the observed increase in signal with discharge frequency was larger than the linear extrapolation value. When the frequency of these waveforms was increased, the amount of current flow and plasma intensity, which is dictated by the derivative of the applied voltage, also increased. Thus, for these waveforms, more plasma events per unit time and higher power discharges occur at higher frequencies. The same is not true for a square wave DBD, in which the derivative of the voltage is fixed for all frequencies. In addition to frequency, the waveform shape was also found to have a significant impact on the number of reagent ions generated by the source. While the square and sawtooth powered LTP produced

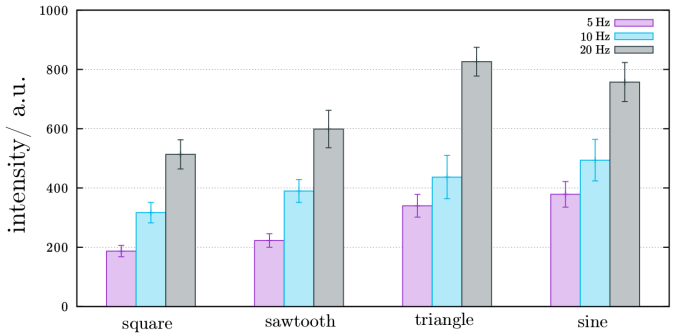

Fig. 5.8: Average ion signal for the $n = 3$ protonated water cluster at m/z 55, as a function of discharge frequency and waveform shape. Error bars represent one standard deviation ion signal. [146]

fixed, homogenous discharge events, fewer reagent ions were produced compared to a source powered by sine and triangle waves. Based on the observations described above, these additional ions can be rationalized to be produced by filamentary microdischarges. Although the microdischarges occurred sporadically and with a relatively low current compared to the homogeneous discharge, they appeared frequently and throughout most of the cycle; hence resulting in the production of more reagent ions and at a higher duty cycle. From the standpoint of ionization capabilities, these findings suggest that a sine or triangle wave LTP should offer more consistent ionization and suffer less from matrix effects. While the frequency range used for the LTP in these studies was significantly lower than that used in other LTP studies, [135;137] these findings can serve as precursory knowledge for predicting and studying the effect of frequency and waveform shape on analytical signal with more conventional LTPs, which has not yet been explored in great detail. At higher frequencies, a greater number of filamentary discharges and presumably reagent ions, would be expected for sine, triangle,

and sawtooth driven LTPs due to an increased voltage change.[155] Ion production should also be more stable as fluctuations of ions from the more frequent filamentary discharges will average out in time and space. In contrast, the sharp voltage transitions for the square wave are independent of frequency and, thus, the reagent ion production should increase almost linearly with frequency.[155] At sufficiently high frequencies (>10 kHz), electrons will not have sufficient time to escape the discharge gap prior to the next discharge event and will enable a more stable glow formation.[156]

Time-resolved analyte signal

In addition to monitoring time-resolved reagent ion signals, the temporal ionization of gas phase analytes was examined. Headspace vapor from liquid species was sampled by the square wave LTP by placing an open vial underneath the source. Full mass spectra were acquired every 2.5 ms and reagent ion signal traces were compared with analyte ion signal traces. Figure 5.9 shows selected ion chronograms for NO^+ (m/z 30), $(H_2O)_3H^+$ (m/z 55), and protonated acetone (MH^+, m/z 59). Interestingly, the time profile for protonated acetone closely matches that of the protonated water clusters with larger, relatively broad peaks followed by shorter narrower and less intense pulses. Meanwhile, the charge-transfer reagents NO^+ and O_2^+ had a notably different pulse structure, similar to that observed in figure 5.3. It is important to note that no analyte ions were detected in the absence of reagent ion signals. These findings clearly demonstrate that acetone was ionized by proton transfer from protonated water clusters and not via photoionization or charge transfer followed by hydrogen abstraction. For comparison, *o*-xylene was also analyzed because it is known to form an odd-electron molecular ion ($M^{\cdot+}$, m/z 106) with plasma-based ADI-MS sources instead

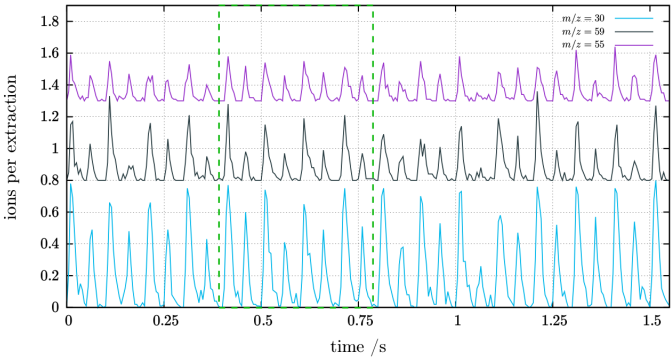

Fig. 5.9: Selected ion chronograms for NO^+ (purple), $(H_2O)_3H^+$ (teal), and the MH^+ for acetone (gray) in the presence of acetone vapor. The LTP was powered with a 10 Hz. 6 kV_{pp} square wave. Note that the trace for protonated acetone closely matches the profile for the protonated water cluster. [146]

of undergoing a proton transfer reaction (figure 5.10). In this case, the long-time stability of the ion signals was poor due to stray air currents varying the concentration of analyte near the source. Because of this effect, two unique scenarios exist. In one case where the concentration of analyte was relatively low (region I in figure 5.10) a pulse for the $M^{+\cdot}$ was detected with no adverse effects on the reagent ion signal. In region II, the local concentration of *o*-xylene was significantly higher, which caused a depletion of the charge-transfer reagent ions (*e.g.* m/z 30), confirming the assumption that *o*-xylene was ionized through charge transfer. The protonated water cluster signal was mostly unaffected in this region. Depletion of appropriate reagent ions is one of the main contributions of matrix effects in plasma-based molecular mass spectrometry and such temporally resolved measurements will be essential to characterize and distinguish between multiple types of matrix effects in plasma-based ADI-MS analyses. [153;154]

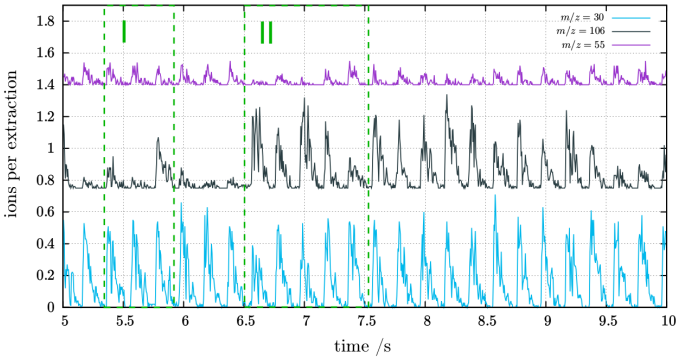

Fig. 5.10: Selected ion chronograms for NO^+ (teal), $(H_2O)_3H^+$ (purple), and the $M^{\cdot+}$ for *o*-xylene (gray) for the detection ox *o*-xylene with 25 % duty cycle 5 Hz, square wave LTP. Region I shows a case where little reagent ion depletion takes place, while region II shows depletion of reagent ions due to excess analyte often resulting in analyte ion suppression. [146]

The immediate vicinity of levitated droplets

A closer look on the microreactor droplet as a whole reveals different zones of analytical interest. The entire system can be classified into three main regions (figure 5.11). The droplet itself contains most of the solvent and species of analytical interest under bulk conditions.

This droplet is enclosed by the second region: the droplet surface. Depending on the definition, the surface has a thickness ranging from only a few molecules up to a few hundred nanometers and thus contains only a small fraction of the overall substance. Despite its relatively small contribution to the overall matter, it is the main interface between the bulk droplet and its surrounding atmosphere. In contrast to the bulk situation deeper within the droplet, this moiety is physicochemically governed by interfacial phenomena. External forces like electric dipole moments or van-der-Waals interactions in this region are strongly directional. Thus, surface

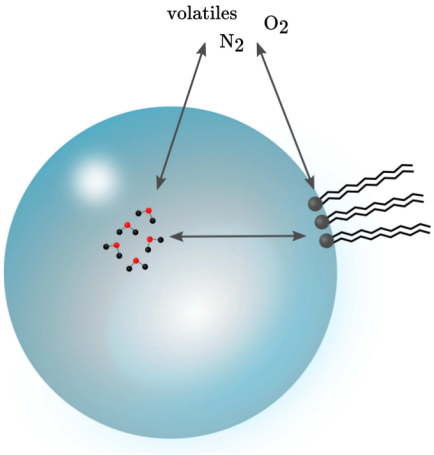

Fig. 5.11: Different regions of analytical interest in levitated droplets.

active compounds will accumulate in this region to monolayers or even more complex structures.

The last zone is the atmosphere surrounding the droplet. Even though this part does not contribute to analytical solutions at first glance, it reveals important information. The surrounding atmosphere can be considered as the close vicinity of the droplet which lies in a diffusive equilibrium with its adjacent space. This region contains gaseous substances interacting with the droplet surface that may even diffuse into the bulk phase, thus their identities and composition should be known. Also, volatile compounds evaporate from the droplet driven by the corresponding vapor pressure. This equilibrium between the bulk and its headspace plays an even more predominant role in µL droplets because of the large surface to volume ratio. Thus, every analytical approach using levitated droplets could greatly benefit from simultaneous interrogation of the surrounding gas phase. Probing this adjacent volume has certain advantages. It offers the possibility to analyze reactions with volatile products

without any interferences from bulk phase molecules and without disturbing the droplet neither with laser desorption nor by heating the droplet. Besides reaction monitoring, an analysis of the droplet environment reveals the evaporation kinetics of complex mixtures. This knowledge is essential to understand, *i.e.* the formation of particles in spray drying processes. But it also yields essential information about the conditions inside the droplet during chemical reactions.

Evaporation process

To study the evaporation process of levitated droplets, LTP ionization offers the best prerequisites. It offers a soft ionization of a small volume at low temperatures with an access to both, polar and nonpolar compounds. To explore the capabilities of LTP for the analysis of a droplet's environment, methanol was chosen as model substance. Its intermediate vapor pressure provides a favorable trade-off between handling and evaporation. Also, its low mass makes the identification of unknown signals much easier. Since there are two competitive ionization pathways, Penning ionization, as well as APCI, the occurrence of radical cations and protonated molecules should be considered when interpreting the spectrum which is shown in figure 5.12. The evaporation was acquired with one accumulated spectrum per second. As seen earlier in figure 5.2, characteristic background signals can be assigned to protonated water and water clusters ($m/z = 19, 37, 55$), $NO^{\cdot +}$ ($m/z = 30$), $O_2^{\cdot +}$ ($m/z = 32$) and O_3^+ ($m/z = 48$). The protonated methanol occurs in the mass spectrum at $m/z = 33$ but also its protonated dimer and trimer can be observed at $m/z = 65$ and $m/z = 97$, respectively. Additionally, the methanol water clusters $[MeOH{+}H_2O{+}H]^+$ at $m/z = 51$ and $[MeOH{+}2(H_2O){+}H]^+$ at $m/z = 83$ can be observed. The temporal

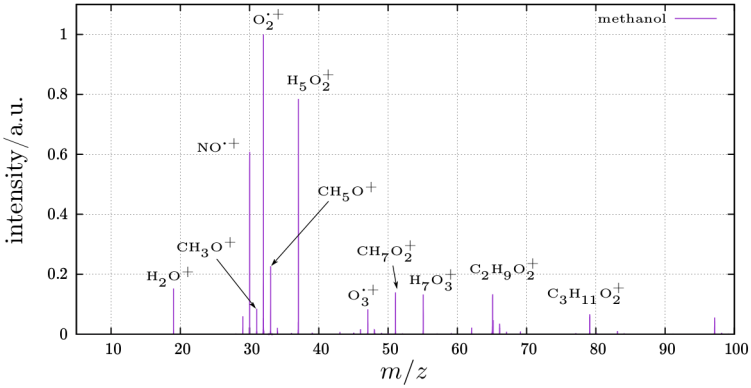

Fig. 5.12: LTP spectrum of a levitated methanol droplet.

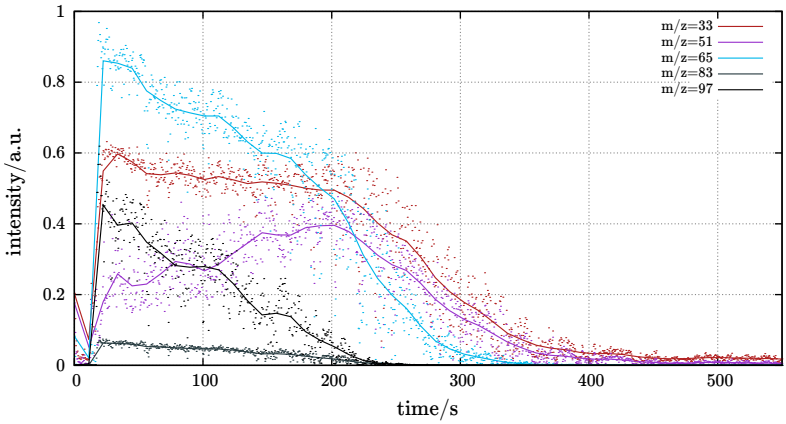

Fig. 5.13: Temporal signals of the formed methanol ions.

signals of those methanol species are shown in figure 5.13. After 12 seconds, a 5 µL methanol droplet was inserted into the levitator which becomes stable after an additional four seconds. All the assigned methanol signals rise simultaneously. While the signal of the protonated monomer remains constant over more than 200 seconds, the signals arising from the dimer and trimer decrease immediately whereby the trimer signal drops faster than the dimer signal. On the other hand, the $[MeOH+H_2O+H]^+$ intensity rises with a maximum around 200 seconds. This behavior is caused by the LTP ionization. Since the used ion source is highly selective for gas phase molecules, the observed clusters are also formed due to collisions at atmospheric pressure in the gas phase. At the beginning, the methanol concentration around the droplet is at its maximum leading to the highest probability for a methanol-methanol collision. With a decreasing methanol concentration beginning from this point gas phase water molecules become more and more competitive collision partners. However, the exact mechanism by which methanol gets depleted remains unclear.

Besides the known background signals and those caused by protonated methanol and methanol clusters, additional unknown peaks are visible in the mass spectrum at the masses $m/z = 31$, $m/z = 47$, $m/z = 65$ and $m/z = 79$. For a further analysis, the TOF resolution in the regarding mass range of approximate $m/\Delta m = 5000$ allows the determination of the atomic composition of those signals. The exact masses and the deriving sum formulas are shown in table 5.1. Under consideration of the time traces of those signals, they can be divided into two groups, one with signal intensities highest directly after inserting the droplet followed by a continually decrease and one where the signal intensities increase until a maximum around 200 s. The first group includes all signals with high intensities immediately after inserting the methanol droplet. These are $m/z = 47.05$

Table 5.1: Exact masses and sum formulas of occurring unknown signals in the LTP mass spectrum of MeOH.

Nominal mass	Exact mass	Calculated mass	Sum formula
31	31.02	31.02	CH_3O
47	47.05	47.05	C_2H_7O
65	65.13	65.06	$C_2H_9O_2$
79	79.07	79.08	$C_3H_{11}O_2$

(C_2H_7O), $m/z = 65.13$ ($C_2H_9O_2$) and $m/z = 79.07$ ($C_3H_{11}O_2$) which can be identified as the protonated dimethyl ether formed by bimolecular methanol combination, the dimethyl ether water cluster and the dimethyl ether methanol cluster. The reaction between a protonated and a neutral methanol molecule highly depends on methanol concentration.

$$2\,CH_3OH \xrightarrow{H^+} (CH_3)_2O + H_2O$$

Since this concentration is the highest directly after inserting the droplet (figure 5.13), the signal of the formed ether immediately starts to decrease. The signal of the formed dimethyl ether methanol cluster follows the same trend. Contrary to the described trend of the $m/z = 51$ methanol water cluster, the methyl ether water cluster follows the same progression as the molecular ether. This can be easily explained by the different formation processes of these water adducts. The water methanol cluster formation depends on the collision probability of those two species while in case of the water ether cluster, water is merely the second reaction product which tends to remain in vicinity to the ether.

The second class of signal progression contains one species at $m/z = 31.02$ (CH_3O). This can be assigned to formaldehyde which

is the oxidation product of the reaction between methanol and the molecular oxygen cation.

$$CH_3OH \xrightarrow{O_2^{\cdot+}} H_2CO + H_2O$$

This reaction is competing to the ether formation while the preference for one of those reaction channels is determined by the methanol concentration. With a high methanol concentration the collision between two methanol molecules is more likely but while the methanol depletes, the reaction between methanol and an oxygen radical cation becomes more likely. Surprisingly, the reaction stops at the step of the formaldehyde formation and no further oxidation products like formic acid, or formyl radicals can be observed. The oxidation of methanol to formaldehyde is a well studied reaction, driven in large scale reactors. However, this high selectivity usually can only be observed in heterogeneously catalyzed reactions[157] whereas oxidation in the gas phase usually does not stop at the formyl radical but continues to the fully oxidized carbon dioxide.

Conclusion

Fast temporally resolved mass spectrometry in combination with a low frequency DBD source allows a direct correlation of transient ion detection with the high voltage waveform. Depending on the shape of the applied voltage, two distinct charge moieties exist. Steep voltage gradients as in square waves lead to a reproducible Townsend discharge through the dielectric barrier occurring at the moment the polarity changes. With slower voltage changes as in sine and triangle waves short (< 40 µs) spontaneous microfilament discharges occur. As the sawtooth wave shows, steep voltage gradients as well as slow ones, both discharge forms occur throughout this waveform. Even though these discharges occur on a short timescale, the formed ion

packages undergo pressure broadening which makes it substantially impossible to distinguish between single events at higher frequencies.

The two described individual discharge regimes could be shown to result in different ionization pathways. Under positive voltage transitions the proton transfer reagents were favored; the corona resulting from the falling edge of a waveform preferentially produces radical cations. Thus, apart from being a powerful tool for plasma diagnostics, low frequency DBD sources could eventually be used for pulsed and selective ion formation.

The LTP source has been proven as a versatile ionization source which offers complementary insights into the droplet system. It enables a contactless and separate investigation of the droplet's environment and therefore facilitates the access to volatile compounds diffusing out of the droplet itself. An investigation of such compounds enables both, a better understanding of evaporation processes of complex mixtures, as well as kinetics of chemical reactions in which volatile products are formed. Those molecules can be detected without any interferences of compounds from the droplets bulk phase.

The formation of reactive species will be exploited in future experiments, for example the ozone generated by the LTP can be used to induce reactions[158] at the surface of a droplet with a monolayer. The possibility to perform reactions like the ozonolysis of oleic acid[159] on the surface of levitated droplets could offer an additional approach to understand the chemistry happening at the surface of atmospheric aerosols.

Chapter 6

Conclusion and Outlook

Within this work, a novel ultrasonic sample holder for mass spectrometric experiments was designed, built, and subsequently optimized. Using this device, a method to probe the bulk phase of levitated droplets as well as the first procedure for the analysis of the droplet's gaseous environment without interferences from the liquid phase were developed.

Ultrasonic levitation

The herein gained knowledge on how different resonator geometries influence the sound pressure intensities and spatial characteristics leads to a better understanding of ultrasonic levitators and therefore yields an important contribution to their design. The ability of curved reflector and sonotrode surfaces to amplify the sound pressure intensity and to increase the pressure node steepness will be further exploited in future setups. Computational modeling for the optimization of different geometries replaces the time consuming process of prototype design and manufacturing, which was partially based on experimental observations rather than comparable numbers. Another factor to be considered in future designs is the radius of the parts. A bigger radius will lead an increase in reflection and a decrease in loss, but will also lead to restrictions regarding the accessibility.

Future ultrasonic sample holders with such optimized geometries can therefore provide even better levitation capabilities which allows to increase the repetition rate in laser desorption experiments or the helium flow used in low temperature plasma sources.

Laser desorption ionization

During this work, laser desorption was proven to be useful for the desorption of small amounts of sample from levitated droplets without any fragmentation caused by *e.g* thermal processes or electronical excitation. The desorbed sample can subsequently be transferred to and analyzed by the mass spectrometer. Furthermore, the used laser pulses cause a soft ionization of analytes from the droplet which enables its optional use as an ionization source.

The ionization process taking place in the spray plume investigated by high speed shadowgraphy is inconsistent with the traditional models explaining the ion formation in MALDI and ESI and therefore raises additional questions. Future experiments will need to further investigate the influence of the laser parameters like wavelength, pulse duration and energy.

Sonic spray ionization

In the performed experiments, sonic spray ionization mimics the aerosol spray induced by the laser desorption pulse with additional benefits caused by its fixed position and the continuity of the spray. The ability of SSI to ionize substances from small molecules up to proteins resulting in ESI-like spectra can be explained by the much higher droplet speeds compared to the LDI process, resulting in a faster and more efficient breakup and ionization. The LIF imaging of the spray plume revealed a spatial preference of the desolvation mechanism and therefore also of the zones where ionization takes places. A closer look into those ionization zones for specific charge states of myoglobin and its heme unit discloses a strong dependency on the angular and radial distribution of the ion formation on their corresponding charge density.

These findings not only help to understand the LDI mechanism better, which will result in an optimized performance in future experiments, but they also indicate that optimizations performed on commercially available ESI instruments are only valid for a specific analyte and, strictly speaking, only for one specific charge state.

Dielectric barrier discharge ionization

Similar to LDI, low temperature plasma sources are capable of desorbing solid analytes and with a limited effectiveness even liquid ones. The most effective analysis, however, can be achieved for gas phase molecules. The two competing ionization mechanisms result in a broad range of accessible analytes. The ionization channels can be controlled by choosing a specific wave form. Optimizing this tunability will result in the option to choose the selectivity of the source. Combined with a periodic change of the ionization method one could also decrease interferences and increase the significance of single peaks.

The described LTP source is also capable of probing the droplet's environment without any perturbing signals from the bulk phase. Due to the continuous character of the source, the progress of reactions inside the droplet can be analyzed by measuring volatile reaction products. The occurrence of reactive species will be exploited in the future to increase the gained chemical information and to utilize the droplet as a model system for atmospheric aerosols.

Chapter 7

Bibliography

[1] K.T. Whitby. Physical Characteristics of Sulfur Aerosols. *Atmospheric Environment*, 12(1-3):135–159, 1978.

[2] E. Vignati, M. C. Facchini, M. Rinaldi, C. Scannell, D. Ceburnis, J. Sciare, M. Kanakidou, S. Myriokefalitakis, F. Dentener, and C. D. O'Dowd. Global scale emission and distribution of sea-spray aerosol: Sea-salt and organic enrichment. *Atmospheric Environment*, 44(5):670–677, 2010.

[3] E. Vignati, M.C. Facchini, M. Rinaldi, C. Scannell, D. Ceburnis, J. Sciare, M. Kanakidou, S. Myriokefalitakis, F. Dentener, and C.D. O'Dowd. Global scale emission and distribution of sea-spray aerosol: Sea-salt and organic enrichment. *Atmospheric Environment*, 44(5):670–677, 2010.

[4] G. M. Whitesides. The origins and the future of microfluidics. *Nature*, 442(7101):368–373, 2006.

[5] MJ Felton. Microfluidics takes a page from the trees. *Analytical Chemistry*, 75(1):14A, JAN 1 2003.

[6] Z. T. Cygan, J. T. Cabral, Kathryn L. Beers, and Eric J. Amis. Microfluidic platform for the generation of organic-phase microreactors. *Langmuir*, 21(8):3629–3634, 2005.

[7] M. Srisa-Art, A. J. deMello, and J. B. Edel. High-throughput DNA droplet assays using picoliter reactor volumes. *Analytical Chemistry*, 79(17):6682–6689, 2007.

[8] Y. Schaerli, R. C. Wootton, T. Robinson, V. Stein, C. Dunsby, M. A. A. Neil, P. M. W. French, A. J. deMello, C. Abell, and F. Hollfelder. Continuous-flow polymerase chain reaction of single-copy DNA in microfluidic microdroplets. *Analytical Chemistry*, 81(1):302–306, 2009.

[9] M. Grumann, J. Steigert, L. Riegger, I. Moser, B. Enderle, K. Riebeseel, G. Urban, R. Zengerle, and J. Ducrée. Sensitivity enhancement for colorimetric glucose assays on whole blood by on-chip beam-guidance. *Biomedical Microdevices*, 8(3):209–214, 2006.

[10] C. P. Price. Point of care testing. *British Medical Journal*, 322(7297):1285–1288, 2001.

[11] M. Toner and D. Irimia. Blood-on-a-chip. *Annual Review of Biomedical Engineering*, 7(1):77–103, 2005.

[12] A. Marie Dupuy, S.n Lehmann, and J. Paul Cristol. Protein biochip systems for the clinical laboratory. *Clinical Chemical Laboratory Medicine*, 43(12):1291–1302, 2005.

[13] L. J. Kricka. Miniaturization of analytical systems. *Clinical Chemistry*, 44(9):2008–2014, 1998.

[14] G. Vecchio, M. Fenech, P. P. Pompa, and N. H. Voelcker. Lab-on-a-chip-based high-throughput screening of the genotoxicity of engineered nanomaterials. *Small*, 10(13):2721–2734, 2014.

[15] J. Shi, D. Ahmed, X. Mao, S.-C. S. Lin, A. Lawit, and T. J. Huang. Acoustic tweezers: patterning cells and microparticles using standing surface acoustic waves (ssaw). *Lab on a Chip*, 9:2890–2895, 2009.

[16] J. El-Ali, P. K. Sorger, and K. F. Jensen. Cells on chips. *Nature*, 442(7101):403–411, 2006.

[17] V. Vandaele, P. Lambert, and A. Delchambre. Non-contact handling in microassembly: Acoustical levitation. *Precision Engineering*, 29(4):491–505, 2005.

[18] S. Santesson and S. Nilsson. Airborne chemistry: acoustic levitation in chemical analysis. *Analytical and Bioanalytical Chemistry*, 378(7):1704–1709, 2004.

[19] M. Klimakow, J. Leiterer, J. Kneipp, E. Roessler, U. Panne, K. Rademann, and F. Emmerling. Combined synchrotron xrd/raman measurements: In situ identification of polymorphic transitions during crystallization processes. *Langmuir*, 26(13):11233–11237, 2010.

[20] S. E. Wolf, J. Leiterer, M. Kappl, F. Emmerling, and W. Tremel. Early homogenous amorphous precursor stages of calcium carbonate and subsequent crystal growth in levitated droplets. *Journal of the American Chemical Society*, 130(37):12342–12347, 2008.

[21] F. Delissen, J. Leiterer, R. Bienert, F. Emmerling, and A. F. Thünemann. Agglomeration of proteins in acoustically levitated droplets. *Analytical and Bioanalytical Chemistry*, 392(1-2):161–165, 2008.

[22] J. Schenk, L. Tröbs, F. Emmerling, J. Kneipp, U. Panne, and M. Albrecht. Simultaneous uv/vis spectroscopy and surface enhanced raman scattering of nanoparticle formation and aggregation in levitated droplets. *Analytical Methods*, 4(5):1252–1258, 2012.

[23] J. Schenk, U. Panne, and M. Albrecht. Interaction of levitated ionic liquid droplets with water. *Journal of Physical Chemistry B*, 116(48):14171–14177, 2012.

[24] D. D. Weis and J. D. Nardozzi. Enzyme kinetics in acoustically levitated droplets of supercooled water: a novel approach to cryoenzymology. *Analytical Chemistry*, 77(8):2558–2563, 2005.

[25] M. S. Westphall, K. Jorabchi, and L. M. Smith. Mass spectrometry of acoustically levitated droplets. *Analytical Chemistry*, 80(15):5847–5853, 2008.

[26] Y. Wada, D. Koyama, and K. Nakamura. Finite-element analysis of acoustic streaming generated between a bending transducer and a reflector through second-order approximated forces. *Acoustical Science and Technology*, 34(5):322–331, 2013.

[27] S. Baer, M.A.B. Andrade, J.C. Adamowski C. Esen, G. Schweiger, and A. Ostendorf. Analysis of the particle stability in a new designed ultrasoniclevitation device. *Review of Scientific Instruments*, 82(5):105111, 2011.

[28] J.J. Thomson. Xix. further experiments on positive rays. *Philosophical Magazine Series 6*, 24(140):209–253, 1912.

[29] T. Satoh, T. Sato, and J. Tamura. Development of a high-performance MALDI-TOF mass spectrometer utilizing a spiral ion trajectory. *Journal of the American Society for Mass Spectrometry*, 18(7):1318–1323, 2007.

[30] M. M. Shahin. Mass-spectrometric studies of corona discharges in air at atmospheric pressures. *The Journal of Chemical Physics*, 45(7):2600–2605, 1966.

[31] J. B. Fenn, M. Mann, C. K. Meng, S. F. Wong, and C. M. Whitehouse. Electrospray ionization for mass-spectrometry of large biomolecules. *Science*, 246(4926):64–71, 1989.

[32] R. Aebersold and M. Mann. Mass spectrometry-based proteomics. *Nature*, 422(6928):198–207, 2003.

[33] Andries P Bruins. Mechanistic aspects of electrospray ionization. *Journal of Chromatography A*, 794(1-2):345–357, 1998.

[34] R. D. Smith, J. A. Loo, R. R. O. Loo, M. Busman, and H. R. Udseth. Principles and practice of electrospray ionization - mass-spectrometry for large polypeptides and proteins. *Mass Spectrometry Reviews*, 10(5):359–451, 1991.

[35] M. Dole. Molecular beams of macroions. *The Journal of Chemical Physics*, 49(5):2240–2249, 1968.

[36] J. V. Iribarne and B. A. Thomson. On the evaporation of small ions from charged droplets. *The Journal of Chemical Physics*, 64(6):2287–2294, 1976.

[37] M. A. Mendes, B. M. Souza, M. R. Marques, and M. S. Palma. The effect of glycerol on signal supression during electrospray ionization analysis of proteins. *Spectroscopy*, 18(2):339–345, 2004.

[38] P. Kebarle and L. Tang. From ions in solution to ions in the gas phase - the mechanism of electrospray mass spectrometry. *Analytical Chemistry*, 65(22):972A–986A, 1993.

[39] E. C. Horning, D. I. Carroll, I. Dzidic, K. D. Haegele, M. G. Horning, and R. N. Stillwell. Atmospheric pressure ionization (API) mass spectrometry. solvent-mediated ionization of samples introduced in solution and in a liquid chromatograph effluent stream. *Journal of Chromatographic Science*, 12(11):725–729, 1974.

[40] D. B. Robb, T. R. Covey, and A. P. Bruins. Atmospheric pressure photoionization: An ionization method for liquid chromatography-mass spectrometry. *Analytical Chemistry*, 72(15):3653–3659, 2000.

[41] A. Raffaelli and A. Saba. Atmospheric pressure photoionization mass spectrometry. *Mass Spectrometry Reviews*, 22(5):318–331, 2003.

[42] R. B. Cody, J. A. Laramée, and H. D. Durst. Versatile new ion source for the analysis of materials in open air under ambient conditions. *Analytical Chemistry*, 77(8):2297–2302, 2005.

[43] S.B. Olenici-Craciunescu, A. Michels, C. Meyer, R. Heming, S. Tombrink, W. Vautz, and J. Franzke. Characterization of a capillary dielectric barrier plasma jet for use as a soft ionization source by optical emission and ion mobility spectrometry. *Spectrochimica Acta Part B: Atomic Spectroscopy*, 64(11-12):1253–1258, 2009.

[44] H. Hayen, A. Michels, and J. Franzke. Dielectric barrier discharge ionization for liquid chromatography/mass spectrometry. *Analytical Chemistry*, 81(24):10239–10245, 2009.

[45] F. J. Andrade, J. T. Shelley, W. C. Wetzel, M. R. Webb, G. Gamez, S. J. Ray, and G. M. Hieftje. Atmospheric pressure chemical ionization source. 1. ionization of compounds in the gas phase. *Analytical Chemistry*, 80(8):2646–2653, 2008.

[46] F. Hillenkamp, M. Karas, R. C. Beavis, and B. T. Chait. Matrix-assisted laser desorption ionization mass-spectrometry of biopolymers. *Analytical Chemistry*, 63(24):1193A–1203A, 1991.

[47] V. V. Laiko, M. A. Baldwin, and A. L. Burlingame. Atmospheric pressure matrix-assisted laser desorption/ionization mass spectrometry. *Analytical Chemistry*, 72(4):652–657, 2000.

[48] J.-L. Wolfender, F. Chu, H. Ball, F. Wolfender, M. Fainzilber, M. A. Baldwin, and A. L. Burlingame. Identification of tyrosine sulfation in conuspennaceus conotoxins α-PnIA and α-PnIB: further investigation of labile sulfo- and phosphopeptides by electrospray, matrix-assisted laser desorption/ionization (MALDI) and atmospheric pressure MALDI mass spectrometry. *Journal of Mass Spectrometry*, 34(4):447–454, 1999.

[49] S. C. Moyer and R. J. Cotter. Peer reviewed: Atmospheric pressure MALDI. *Analytical Chemistry*, 74(17):468A–476A, 2002.

[50] M. Barmatz and P. Collas. Acoustic radiation potential on a sphere in plane, cylindrical, and spherical standing wave fields. *Journal of the Acoustical Society of America*, 77(3):928–945, 1985.

[51] E. G. Lierke and L. Holitzner. Positioning of drops, particles and bubbles in ultrasonic standing-waves levitators. a final round up. *Acta Acustica United with Acustica*, 99(2):302–316, 2013.

[52] W. J. Xie, C. D. Cao, and B. B. Wei. Experimental investigation and numerical analysis on acoustic levitation. *Acta Physica Sinica*, 48(2):250–256, 1999.

[53] M. A. B. Andrade, F. Buiochi, and J. C. Adamowski. Finite element analysis and optimization of a single-axis acoustic levitator. *IEEE Transactions on Ultrasonics Ferroelectrics and Frequency Control*, 57(2):469–479, 2010.

[54] T. Kozuka, K. Yasui, T. Tuziuti, A. Towata, and Y. Ilda. Acoustic standing-wave field for manipulation in air. *Japanese Journal of Applied Physics*, 47(5):4336–4338, 2008.

[55] T. Kozuka, K. Yasui, T. Tuziuti, A. Towata, J. Lee, and Y. Iida. Measurement and numerical calculation of force on a particle in a strong acoustic field required for levitation. *Japanese Journal of Applied Physics*, 48(7):07GM09–07GM09, 2009.

[56] T. Kozuka, K. Yasui, T. Tuziuti, A. Towata, and Y. Iida. Noncontact acoustic manipulation in air. *Japanese Journal of Applied Physics Part 1-Regular Papers Brief Communications and Review Papers*, 46(7B):4948–4950, 2007.

[57] D. Koyama and K. Nakamura. Noncontact ultrasonic transportation of small objects over long distances in air using a bending vibrator and a reflector. *IEEE Transactions on Ultrasonics Ferroelectrics and Frequency Control*, 57(5):1152–1159, 2010.

[58] D. Koyama and K. Nakamura. Noncontact ultrasonic transportation of small objects in a circular trajectory in air by flexural vibrations of a circular disc. *IEEE Transactions on Ultrasonics Ferroelectrics and Frequency Control*, 57(6):1434–1442, 2010.

[59] D. Foresti, M. Nabavi, M. Klingauf, A. Ferrari, and D. Poulikakos. Acoustophoretic contactless transport and handling of matter in air. *Proceedings of the National Academy of Sciences of the United States of America*, 110(31):12549–12554, 2013.

[60] M. A. B. Andrade, N. Perez, F. Buiochi, and J. C. Adamowski. Matrix method for acoustic levitation simulation. *IEEE Transactions on Ultrasonics Ferroelectrics and Frequency Control*, 58(8):1674–1683, 2011.

[61] A. Ibánez, C. Fritsch, M. Parrilla, and J. Villazón. Monochromatic transfer matrix method for acoustic field simulation thorough media boundaries. *Physics Procedia*, 3(1):883 – 890, 2010.

[62] R. Tuckermann, B. Neidhart, E. G. Lierke, and S. Bauerecker. Trapping of heavy gases in stationary ultrasonic fields. *Chemical Physics Letters*, 363(3-4):349–354, 2002.

[63] W. A. Oran, L. H. Berge, and H. W. Parker. Parametric study of an acoustic levitation-system. *Review of Scientific Instruments*, 51(5):626–631, 1980.

[64] D. Möller, N. Degen, and J. Dual. Schlieren visualization of ultrasonic standing waves in mm-sized chambers for ultrasonic particle manipulation. *Journal of Nanobiotechnology*, 11(21):1–5, 2013.

[65] P. Zheng, E. Li, J. Zhao, J. Di, W. Zhou, H. Wang, and R. Zhang. Visualized measurement of the acoustic levitation field based on digital holography with phase multiplication. *Optics Communications*, 282(22):4339–4344, 2009.

[66] Y. Abe, D. Hyuga, S. Yamada, and K. Aoki. Study on internal flow and surface deformation of large droplet levitated by ultrasonic wave. *Annals of the New York Academy of Sciences*, 1077(1):49–62, 2006.

[67] G. Zhou and M. Li. A study on ultrasonic solid horns for flexural mode. *The Journal of the Acoustical Society of America*, 107(3):1358–1362, 2000.

[68] Michael Hercher. The spherical mirror fabry-perot interferometer. *Applied Optics*, 7(5):951–966, 1968.

[69] W. Xie and B. Wei. Dependence of acoustic levitation capabilities on geometric parameters. *Phys. Rev. E*, 66(2):026605, 2002.

[70] S. Amini, H. Soleimanimehr, M.J. Nategh, A. Abudollah, and M.H. Sadeghi. FEM analysis of ultrasonic-vibration-assisted turning and the vibratory tool. *Journal of Materials Processing Technology*, 201(1-3):43–47, 2008.

[71] M. A. B. Andrade, T. S. Ramos, T. A. O. Fabio, and J. C. Adamowski. Nonlinear characterization of a single-axis accoustic levitator. *Review of scientific instruments*, 85(4):045125, 2014.

[72] A. Stindt, M. A. B. Andrade, M. Albrecht, J. C. Adamowski, U. Panne, and J. Riedel. Experimental and numerical characterization of the sound pressure in standing wave acoustic levitators. *Review of Scientific Instruments*, 85(1):015110, 2014.

[73] L. Li, A. P. L. Wang, and L. D. Coulson. Continuous-flow matrix-assisted laser desorption ionization mass-spectrometry. *Analytical Chemistry*, 65(4):493–495, 1993.

[74] M. Faubel, S. Schlemmer, and J. P. Toennies. A molecular-beam study of the evaporation of water from a liquid jet. *Zeitschrift Für Physik D-Atoms Molecules and Clusters*, 10(2-3):269–277, 1988.

[75] W. Kleinekofort, J. Avdiev, and B. Brutschy. A new method of laser desorption mass spectrometry for the study of biological macromolecules. *International Journal of Mass Spectrometry and Ion Processes*, 152(2-3):135–142, 1996.

[76] R. G. Cooks, Z. Ouyang, Z. Takats, and J. M. Wiseman. Ambient mass spectrometry. *Science*, 311(5767):1566–1570, 2006.

[77] J. M. Daniel, V. V. Laiko, V. M. Doroshenko, and R. Zenobi. Interfacing liquid chromatography with atmospheric pressure MALDI-MS. *Analytical and Bioanalytical Chemistry*, 383(6):895–902, 2005.

[78] E. Rapp, A. Charvat, A. Beinsen, U. Plessmann, U. Reichl, A. Seidel-Morgenstern, H. Urlaub, and B. Abel. Atmospheric pressure free liquid infrared MALDI mass spectrometry: Toward a combined ESI/MALDI-liquid chromatography interface. *Analytical Chemistry*, 81(1):443–452, 2009.

[79] A. Stindt, M. Albrecht, U. Panne, and J. Riedel. Co2 laser ionization of acoustically levitated droplets. *Analytical and Bioanalytical Chemistry*, 405(DOI: 10.1007/s00216-012-6500-y):7005–7010, 2012.

[80] E. Nordhoff, A. Ingendoh, R. Cramer, A. Overberg, B. Stahl, M. Karas, F. Hillenkamp, and P. F. Crain. Matrix-assisted laser desorption ionization mass-spectrometry of nucleic-acids with wavelengths in the ultraviolet and infrared. *Rapid Communications in Mass Spectrometry*, 6(12):771–776, 1992.

[81] A. Apffel, S. Fischer, G. Goldberg, P. C. Goodley, and F. E. Kuhlmann. Enhanced sensitivity for peptide-mapping with electrospray liquid-chromatography mass-spectrometry in the presence of signal suppression due to trifluoroacetic acid-containing mobile phases. *Journal of Chromatography A*, 712(1):177–190, 1995.

[82] C. Dass. Gas-phase fragmentation reactions of protonated glycerol and its oligomers - metastable and collision-induced dissociation reactions, associated deuterium-isotope effects and the structure of $C_3H_5O^+$, $C_2H_5O^+$, $C_2H_4O^+$. and $C_2H_3O^+$ ions. *Organic Mass Spectrometry*, 29(9):475–482, 1994.

[83] M. Karas and R. Kruger. Ion formation in MALDI: The cluster ionization mechanism. *Chemical Reviews*, 103(2):427–440, 2003.

[84] T. W. Jaskolla, M. Karas, U. Roth, K. Steinert, C. Menzel, and K. Reihs. Comparison between vacuum sublimed matrices and conventional dried droplet preparation in MALDI-tof mass spectrometry. *Journal of the American Society for Mass Spectrometry*, 20(6):1104–1114, 2009.

[85] R. Zenobi and R. Knochenmuss. Ion formation in MALDI mass spectrometry. *Mass Spectrometry Reviews*, 17(5):337–366, 1998.

[86] T. W. Jaskolla and M. Karas. Compelling evidence for lucky survivor and gas phase protonation: The unified MALDI analyte protonation mechanism. *Journal of the American Society for Mass Spectrometry*, 22(6):976–988, 2011.

[87] E. P. L. Hunter and S. G. Lias. Evaluated gas phase basicities and proton affinities of molecules: An update. *Journal of Physical and Chemical Reference Data*, 27(3):413–656, 1998.

[88] A. Hirabayashi, M. Sakairi, and H. Koizumi. Sonic spray ionization method for atmospheric-pressure ionization mass-spectrometry. *Analytical Chemistry*, 66(24):4557–4559, 1994.

[89] M. Yamashita and J. B. Fenn. Electrospray ion-source - another variation on the free-jet theme. *Journal of Physical Chemistry*, 88(20):4451–4459, 1984.

[90] M. M. Antonakis, A. Tsirigotaki, K. Kanaki, C. J. Milios, and S. A. Pergantis. Bipolar mass spectrometry of labile coordination complexes, redox active inorganic compounds, and proteins using a glass nebulizer for sonic-spray ionization. *Journal of the American Society for Mass Spectrometry*, 24(8):1250–1259, 2013.

[91] N. D. Chubatyi, T. W. Wang, and C. N. McEwen. More inclusive or selective ionization for mass spectrometry using obstructive sonic spray ionization and voltage polarity switching. *Rapid Communications in Mass Spectrometry*, 26(23):2763–2769, 2012.

[92] Z. Takats, S. C. Nanita, and R. G. Cooks. Serine octamer reactions: Indicators of prebiotic relevance. *Angewandte Chemie-International Edition*, 42(30):3521–3523, 2003.

[93] Z. Takats, S. C. Nanita, R. G. Cooks, G. Schlosser, and K. Vekey. Amino acid clusters formed by sonic spray ionization. *Analytical Chemistry*, 75(6):1514–1523, 2003.

[94] R. Haddad, R. Sparrapan, and M. N. Eberlin. Desorption sonic spray ionization for (high) voltage-free ambient mass spectrometry. *Rapid Communications in Mass Spectrometry*, 20(19):2901–2905, 2006.

[95] V. G. Santos, T. Regiani, F. F. G. Dias, W. Romao, J. L. P. Jara, C. F. Klitzke, F. Coelho, and M. N. Eberlins. Venturi easy ambient sonic-spray ionization. *Analytical Chemistry*, 83(4):1375–1380, 2011.

[96] D. Touboul, M. C. Jecklin, and R. Zenobi. Ion internal energy distributions validate the charge residue model for small molecule ion formation by spray methods. *Rapid Communications in Mass Spectrometry*, 22(7):1062–1068, 2008.

[97] A. Wortmann, A. Kistler-Momotova, R. Zenobi, M. C. Heine, O. Wilhelm, and S. E. Pratsinis. Shrinking droplets in electrospray ionization and their influence on chemical equilibria. *Journal of the American Society for Mass Spectrometry*, 18(3):385–393, 2007.

[98] J. N. Smith, R. C. Flagan, and J. L. Beauchamp. Droplet evaporation and discharge dynamics in electrospray ionization. *Journal of Physical Chemistry A*, 106(42):9957–9967, 2002.

[99] K. Chingin, V. Frankevich, R. M. Balabin, K. Barylyuk, H. W. Chen, R. Wang, and R. Zenobi. Direct access to isolated biomolecules under ambient conditions. *Angewandte Chemie-International Edition*, 49(13):2358–2361, 2010.

[100] B. A. Thomson and J. V. Iribarne. Field-Induced Ion Evaporation from Liquid Surfaces at Atmospheric-Pressure. *Journal of Chemical Physics*, 71(11):4451–4463, 1979.

[101] P. Kebarle and U. H. Verkerk. Electrospray: from ions in solution to ions in the gas phase, what we know now. *Mass Spectrometry Reviews*, 28(6):898–917, 2009.

[102] L. W. Zilch, J. T. Maze, J. W. Smith, G. E. Ewing, and M. F. Jarrold. Charge separation in the aerodynamic breakup of micrometer-sized water droplets. *Journal of Physical Chemistry A*, 112(51):13352–13363, 2008.

[103] A. Hirabayashi and J. F. de la Mora. Charged droplet formation in sonic spray. *International Journal of Mass Spectrometry*, 175(3):277–282, 1998.

[104] Y. Yair. Charge generation and separation processes. *Space Science Reviews*, 137(1-4):119–131, 2008.

[105] I. Bhattacharyya, J. T. Maze, G. E. Ewing, and M. F. Jarrold. Charge separation from the bursting of bubbles on water. *The Journal of Physical Chemistry A*, 115(23):5723–5728, 2010.

[106] C. Saunders. Charge separation mechanisms in clouds. In *Planetary Atmospheric Electricity*, pages 335–353. Springer, 2008.

[107] A. Stindt, C. Warschat, A. Bierstedt, U. Panne, and J. Riedel. Characterization of an inexpensive sonic spray ionization source using laser induced fluorescence imaging and mass spectrometry. *European Journal of Mass Spectrometry*, 20(1):21–29, 2013.

[108] P. James. Protein identification in the post-genome era: the rapid rise of proteomics. *Quarterly Reviews of Biophysics*, 30(4):279–331, 1997.

[109] A. Hirabayashi, M. Sakairi, and H. Koizumi. Sonic spray mass-spectrometry. *Analytical Chemistry*, 67(17):2878–2882, 1995.

[110] C. G. Enke. A predictive model for matrix and analyte effects in electrospray ionization of singly-charged ionic analytes. *Analytical Chemistry*, 69(23):4885–4893, 1997.

[111] F. Renth, J. Riedel, and F. Temps. Inversion of velocity map ion images using iterative regularization and cross validation. *Review of Scientific Instruments*, 77(3):033103, 2006.

[112] E. W. Hansen and P. L. Law. Recursive methods for computing the abel transform and its inverse. *Journal of the Optical Society of America a-Optics Image Science and Vision*, 2(4):510–520, 1985.

[113] R. N. Bracewell. *The Fourier transform and its applications*. McGraw-Hill, New York, 1986.

[114] I. L. Arbeloa and K. K. Rohatgimukherjee. Solvent effect on photophysics of the molecular-forms of rhodamine-b - solvation models and spectroscopic parameters. *Chemical Physics Letters*, 128(5-6):474–479, 1986.

[115] T. L. Chang and H. C. Cheung. Solvent effects on the photoisomerization rates of the zwitterionic and the cationic forms of rhodamine-b in protic solvents. *Journal of Physical Chemistry*, 96(12):4874–4878, 1992.

[116] S. K. Sagoo and R. A. Jockusch. The fluorescence properties of cationic rhodamine b in the gas phase. *Journal of Photochemistry and Photobiology a-Chemistry*, 220(2-3):173–178, 2011.

[117] J. V. Iribarne and B. A. Thomson. Evaporation of small ions from charged droplets. *Journal of Chemical Physics*, 64(6):2287–2294, 1976.

[118] H. W. Liepmann Roshko and A. *Elements of Gasdynamics*. Wiley and Sons, New York, 1957.

[119] A. T. Iavarone, J. C. Jurchen, and E. R. Williams. Effects of solvent on the maximum charge state and charge state distribution of protein ions produced by electrospray ionization. *Journal of the American Society for Mass Spectrometry*, 11(11):976–985, 2000.

[120] C. A. Schneider, W. S. Rasband, and K. W. Eliceiri. Image to ImageJ: 25 Years of image analysis. *Nature Methods*, 9(7):671–675, 2012.

[121] S. Nguyen and J. B. Fenn. Gas-phase ions of solute species from charged droplets of solutions. *Proceedings of the National Academy of Sciences*, 104(4):1111–1117, 2007.

[122] P Kebarle and M Peschke. On the mechanisms by which the charged droplets produced by electrospray lead to gas phase ions. *Analytica Chimica Acta*, 406(1):11–35, 2000.

[123] AA Puretzky, DB Geohegan, GB Hurst, MV Buchanan, and BS Luk'yanchuk. Imaging of vapor plumes produced by matrix assisted laser desorption: a plume sharpening effect. *Physical review letters*, 83(2):444–446, 1999.

[124] Chi Wei Liang, Chih Hao Lee, Yu-Jiun Lin, Yuan Tseh Lee, and Chi Kung Ni. Maldi mechanism of dihydroxybenzoic acid isomers: desorption of neutral matrix and analyte. *The Journal of Physical Chemistry B*, 117(17):5058–5064, 2013.

[125] W. Wissdorf, M. Lorenz, T. Poehler, H. Hoenen, and T. Benter. Atmospheric Pressure Ion Source Development: Experimental Validation of Simulated Ion Trajectories within Complex Flow and Electrical Fields. *Journal of the American Society for Mass Spectrometry*, 24(10):1456–1466, 2013.

[126] K. Pochner, W. Neff, and R. Lebert. Atmospheric pressure gas discharges for surface treatment. *Surface and Coatings Technology*, 74-75, Part 1(1):394 – 398, 1995. Fourth International Conference on Plasma Surface Engineering.

[127] G. Baravian, D. Chaleix, P. Choquet, P.L. Nauche, V. Puech, and M. Rozoy. Oil removal from iron surfaces by atmospheric-pressure barrier discharges. *Surface and Coatings Technology*, 115(1):66–69, 1999.

[128] M. A. Malik, A. Ghaffar, and S. A. Malik. Water purification by electrical discharges. *Plasma Sources Science and Technology*, 10(1):82–91, 2001.

[129] O. Goossens, E. Dekempeneer, D. Vangeneugden, R. Van de Leest, and C. Leys. Application of atmospheric pressure dielectric barrier discharges in deposition, cleaning and activation. *Surface and Coatings Technology*, 142-144(0):474–481, 2001.

[130] I. P. Vinogradov and K. Wiesemann. Classical absorption and emission spectroscopy of barrier discharges in mixtures. *Plasma Sources Science and Technology*, 6(3):307–316, 1997.

[131] T. I. Lee, K. W. Park, H. K. Baik, and S.-M. Lee. Dielectric barrier hollow cathode discharge and its enhanced performance for light source. *Applied Physics Letters*, 87(26):261502, 2005.

[132] Z. Zhu, G. C.-Y. Chan, S. J. Ray, X. Zhang, and G. M. Hieftje. Microplasma source based on a dielectric barrier discharge for the determination of mercury by atomic emission spectrometry. *Analytical Chemistry*, 80(22):8622–8627, 2008.

[133] Y. Yu, Z. Du, M. Chen, and J. Wang. Atmospheric-pressure dielectric-barrier discharge as a radiation source for optical emission spectrometry. *Angewandte Chemie International Edition*, 47(41):7909–7912, 2008.

[134] Y. Zhang, X. Ma, S. Zhang, C. Yang, Z. Ouyang, and X. Zhang. Direct detection of explosives on solid surfaces by low temperature plasma desorption mass spectrometry. *Analyst*, 134:176–181, 2009.

[135] J. D. Harper, N. A. Charipar, C. C. Mulligan, X. Zhang, R. G. Cooks, and Z. Ouyang. Low-temperature plasma probe for ambient desorption ionization. *Analytical Chemistry*, 80(23):9097–9104, 2008.

[136] C. Meyer, S. Muller, E. L. Gurevich, and J. Franzke. Dielectric barrier discharges in analytical chemistry. *Analyst*, 136:2427–2440, 2011.

[137] J. S. Wiley, J. T. Shelley, and R. G. Cooks. Handheld low-temperature plasma probe for portable "point-and-shoot" ambient ionization mass spectrometry. *Analytical Chemistry*, 85(14):6545–6552, 2013.

[138] B Eliasson, M Hirth, and U Kogelschatz. Ozone synthesis from oxygen in dielectric barrier discharges. *Journal of Physics D: Applied Physics*, 20(11):1421–1437, 1987.

[139] B. Eliasson and U. Kogelschatz. Modeling and applications of silent discharge plasmas. *Plasma Science, IEEE Transactions on*, 19(2):309–323, 1991.

[140] Eliasson B., W. Egli, and Kogelschatz U. Modelling of dielectric barrier discharge chemistry. *Pure and Applied Chemistry*, 66(6):1275–1286, 2009.

[141] G. C.-Y. Chan, J. T. Shelley, A. U. Jackson, J. S. Wiley, C. Engelhard, R. G. Cooks, and G. M. Hieftje. Spectroscopic plasma diagnostics on a low-temperature plasma probe for ambient mass spectrometry. *Journal of Analytical Atomic Spectrometry*, 26:1434–1444, 2011.

[142] M. S. Heywood, N. Taylor, and P. B. Farnsworth. Measurement of helium metastable atom densities in a plasma-based ambient ionization source. *Analytical Chemistry*, 83(17):6493–6499, 2011.

[143] G. C.-Y. Chan, Jacob T. S., J. S. Wiley, C. Engelhard, A. U. Jackson, R. G. Cooks, and G. M. Hieftje. Elucidation of reaction mechanisms responsible for afterglow and reagent-ion formation in the low-temperature plasma probe ambient ionization source. *Analytical Chemistry*, 83(10):3675–3686, 2011.

[144] X. Lu and M. Laroussi. Dynamics of an atmospheric pressure plasma plume generated by submicrosecond voltage pulses. *Journal of Applied Physics*, 100(6):063302, 2006.

[145] J. Shi, F. Zhong, J. Zhang, D. W. Liu, and M. G. Kong. A hypersonic plasma bullet train traveling in an atmospheric dielectric-barrier discharge jet. *Physics of Plasmas*, 15(1):013504, 2008.

[146] J. T. Shelley, A. Stindt, J. Riedel, and C. Engelhard. Time-resolved mass-spectral characterization of ion formation from a low-frequency, low-temperature plasma probe ambient ionization source. *Journal of Analytical Atomic Spectrometry*, 29(2):359–366, 2014.

[147] K. J. Brockmann, W. Walter, M. Lorenz, D. Müller, T. Poehler, R. Kunte, and T. Benter, editors. *Proceedings of the 60th Annual American Society for Mass Spectrometry Conference*, volume 4 of *5*, Canada, Vancouver, BC, 2012. JASMS.

[148] S. E. Hobbs and J. W. Olesik. Inductively coupled plasma mass spectrometry signal fluctuations due to individual aerosol droplets and vaporizing particles. *Analytical Chemistry*, 64(3):274–283, 1992.

[149] M. P. Dziewatkoski, L. B. Daniels, and J. W. Olesik. Time-resolved inductively coupled plasma mass spectrometry measurements with individual, monodisperse drop sample introduction. *Analytical Chemistry*, 68(7):1101–1109, 1996.

[150] H.-E. Wagner, R. Brandenburg, K.V. Kozlov, A. Sonnenfeld, P. Michel, and J.F. Behnke. The barrier discharge: basic properties and applications to surface treatment. *Vacuum*, 71(3):417–436, 2003. Symposium on Plasma Surface Engineering at the Spring Meeting of the German Physical Society, Regensburg, Germany, March 11-15 2002.

[151] Anthony D. A. and David A. D. Simion ion optics simulations at atmospheric pressure. *International Journal of Mass Spectrometry*, 244(1):1–14, 2005.

[152] T. Poehler, R. Kunte, H. Hoenen, P. Jeschke, W. Wissdorf, K. J. Brockmann, and T. Benter. Numerical simulation and experimental validation of the three-dimensional flow field and relative analyte concentration distribution in an atmospheric pressure ion source. *Journal of The American Society for Mass Spectrometry*, 22(11):2061–2069, 2011.

[153] J. T. Shelley and G. M. Hieftje. Ambient mass spectrometry: Approaching the chemical analysis of things as they are. *Journal of Analytical Atomic Spectrometry*, 26:2153–2159, 2011.

[154] J. T. Shelley and G. M. Hieftje. Ionization matrix effects in plasma-based ambient mass spectrometry sources. *Journal of Analytical Atomic Spectrometry*, 25:345–350, 2010.

[155] N. Benard and E. Moreau. Role of the electric waveform supplying a dielectric barrier discharge plasma actuator. *Applied Physics Letters*, 100(19):193503, 2012.

[156] W. Jiang, J. Tang, Y. Wang, W. Zhao, and Y. Duan. Influence of driving frequency on discharge modes in a dielectric-barrier discharge with multiple current pulses. *Physics of Plasmas*, 20(7):073509, 2013.

[157] T. H. Kim, B. Ramachandra, J. S. Choi, M. B. Saidutta, K. Y. Choo, S. D. Song, and Y. W. Rhee. Selective oxidation of methanol to formaldehyde using modified iron-molybdate catalysts. *Catalysis Letters*, 98(2-3):161–165, 2004.

[158] A. W. Norgaard, A. Vibenholt, M. Benassi, P. A. Clausen, and P. Wolkoff. Study of Ozone-Initiated Limonene Reaction Products by Low Temperature Plasma Ionization Mass Spectrometry. *Journal of the American Society for Mass Spectrometry*, 24(7):1090–1096, 2013.

[159] J. Kleber, K. Lass, and G. Friedrichs. Quantitative Time-Resolved Vibrational Sum Frequency Generation Spectroscopy as a Tool for Thin Film Kinetic Studies: New Insights into Oleic Acid Monolayer Oxidation. *Journal of Physical Chemistry A*, 117(33):7863–7875, 2013.